第 5 回 豊田ビームライン研究発表会

（第 11 回 SPring-8 産業利用報告会）

期間： 2014 年 9 月 4 日（木）～ 5 日（金）

会場： 姫路商工会議所

主催： (株)豊田中央研究所、
(公財)高輝度光科学研究センター（JASRI）、兵庫県、
サンビーム（産業用専用ビームライン建設利用共同体）

共催： SPring-8 利用推進協議会、姫路市、姫路商工会議所

協賛： フロンティアソフトマター開発専用ビームライン産学連合体、
SPRUC 企業利用研究会、（一財）高度情報科学技術研究機構、
（一財）総合科学研究機構東海事業センター、
光ビームプラットホーム

目 次

ご挨拶

2015 年 1 月
株式会社豊田中央研究所
分析・計測部　妹尾与志木

第 5 回目となります豊田ビームライン研究発表会のプロシーディングスを発刊いたします。この発表会は 2014 年 9 月 4 日、5 日に姫路商工会議所にて開催されました第 11 回 SPring-8 産業利用報告会の中の一部として行われたもので、本冊子はその発表の記録に相当いたします。

豊田ビームライン（SPring-8 BL33XU）は 2013 年に中間評価を受ける段階まで来ており、測定手法面の整備は一応の終息点に来たと考えております。その中には、産業利用の視点からではありますがオリジナリティーの高い独自の手法を開発できたと、自負しているものもあります。早い現象を観測する Superquick XAFS 法はすでに多くの場でご紹介しておりますが、本プロシーディングスにあります、結晶材料内部を観察する 3 次元 X 線回折顕微鏡法や、高い空間分解能を保ったまま 2 次元検出器を用いて回折実験が可能になるスリットなども誇れるものと考えております。また自動車業界らしい研究である焼き付き現象のその場観察は、上記産業利用報告会にてご参加の方々より高い評価をいただきました。これらの成果は理研、JASRI の研究者の方々を始めとする多くの皆様のご支援の賜物です。心より御礼申し上げます。

しかしながら、私たち産業界の人間にとりましては、放射光利用の手法整備はあくまでも手段であり、それを用いて生産活動に貢献できる結果を得ることが目的のはずです。手法の開発にあまりに労力がかかると、ついついそれを忘れがちになりますが、そこを履き違えてはいけないと自戒しております。豊田ビームラインでの実施テーマも、その意味ではこれからが正念場、と考えられるものが多くあると感じております。

さらに2013年度にいただきました中間評価の中に、「利用の成果を専門家でない方々にもアピールするように」とのコメントがありました。実を申しますと、この部分は自身の社やグループ内の活動においても非常に頭を悩ませている点です。本プロシーディングスは、当然その理解活動の一助のつもりではありますが、ほかにも工夫をこらして活動を継続していかなくてはならないであろうと思っております。

今後とも、豊田ビームラインの活動にご理解、ご協力をよろしくお願い申し上げます。

以上

2013A7012、2013B7012 BL33XU

放射光回折応力測定のための２次元検出器用スリットの開発
Developed Slit System for Synchrotron X-ray Stress Measurement with Area Detector

瀬戸山 大吾[a]，木村 英彦[a]，広瀬 美治[a]，山口 聡[a]
Daigo Setoyama[a], Hidehiko Kimura[a], Yoshiharu Hirose[a], and Satoshi Yamaguchi[a]

[a](株)豊田中央研究所
[a]Toyota Central R&D Labs. Inc

自動車等の材料･部品内部の応力･ひずみ分布、組織状態の経時変化の計測手法の一つとして、2 次元検出器を用いた放射光 X 線回折測定は有望である。このとき、材料内部で必要十分な空間分解能、回折角分解能を確保するためには、受光側に何らかのスリット系が必要であり、これまでに複数の提案が報告されている。本発表では、既往の研究例を踏まえ新たに 2 次元検出器用のスリットを開発し、その性能を検証した。

キーワード: 放射光 X 線回折、応力･ひずみ測定、2 次元検出器、スリット、内部応力･ひずみ

背景と研究目的

2 次元検出器を用いた X 線応力・ひずみ評価法は、結晶配向の強い材料、粗大粒材を効率よく評価できる手法の一つであり、ここに高輝度放射光 X 線を用いることで、材料内部・微小部の応力・ひずみ分布を評価できうる。ただし、材料中の位置を特定するためには、(特に試料-検出器間に)何らかのスリット系を設ける必要がある。これまでに、様々なスリットが提案されてきたが、それぞれに長所と短所がある事が分かっている。そこで本研究では、既往のスリットの特徴を踏まえ、新たに 2 次元検出器用のスリットを開発した。さらに、この開発スリットを用いて、材料内部のひずみ分布の計測を試み、対応する数値解析と比較することで性能検証を行った。

既往の 2 次元検出器用スリット

放射光 X 線回折測定を前提とした 2 次元検出器用スリットの代表的な 3 例に、コニカルスリット[1、2]、静置型スパイラルスリット[3–5]、および回転型スパイラルスリット[6]が挙げられる。

コニカルスリットは、2000 年頃デンマーク Risø National Lab.で提案され、平板に同心円状に空隙の空いたスリット板である。スリットは試料位置を頂点とする円錐面を成しており、回折角に応じて傾斜したスリット形状となっている。回折角はスリット作製時点で固定されているため、白色 XRD で結晶系が既知の材料の計測に有効である。一方で、試料の任意性や複合材料、相変態の計測に困難を伴うと考えられる。

2003 年頃に発表された静置型スパイラルスリットは、スリット形状が渦状になっているため任意の回折角を放つ試料への適用が可能である。また、ほぼ同一寸法のスリット板 2 枚の方位各方向の位相を変化させることで、スリット幅を任意の幅に設定できる。一方、このス

リット構造ではスリット自身により遮蔽される方位角範囲が存在する。従って、粗大粒材や微小領域の計測の場合のように回折光が斑点状に得られる場合や、異方性のきわめて強い材料に対しては、応力・ひずみ等を評価するために十分な回折像が 2 次元検出器で得られない可能性がある。

この点を解決したのが 2010 年頃鈴木、菖蒲等により考案された回転型スパイラルスリットで、スリット構造全体を入射光軸を中心に回転させることで、静置型スパイラルスリットの問題を解決している。加えて相似な大小 2 枚のスリット円盤により回折光の発散角を低減させ、測定位置と回折角の精度を高めている。らせん状のスリット形状は、アルキメデスの渦巻き曲線型やインヴォリュート曲線型が採用されている。

ところでこれらのスリットは、基本的にその中心が光軸と一致するように配置される。従って、利用できる回折角の上限がスリット円板の半径と試料-スリット間の距離に制約されてしまう。従って試料や検出器の特性から比較的低エネルギーの放射光で大きい回折角の測定を行う必要のある場合、計測が難しい問題が残されている。

開発スリットの概要

本研究では、これら既往のスリットの課題に対処した新規スリットを開発した。本スリットを用いた測定の概要を Fig. 1 に示す。本スリットは前述の各種スリットと同様に、試料と 2 次元検出器の間に配置され、いわゆる 0 次元検出器を用いた従来の X 線回折測定における散乱スリット、受講スリットの役割を担う。2 枚のスリット円板間の距離を、搭載する回折計の許容する範囲で可能な限り遠ざけることで、回折光の発散角を可能な限り抑制している。

本スリットは回転型スパイラルスリットと同様、大小の相似形状のスリット円板で構成され、円板中心軸の延長線上でかつ大小のスリットの相似中心位置に試料が位置するように配置される。この配置によって、相似中心位置からの回折光のみを後方の 2 次元検出器でとらえ、他の位置からの回折光を除去することができるので、材料内部の局所応力・ひずみ計測が可能となる。

本研究のスリット構造は、既往の回転型スパイラルスリットと同様の回転機構を備えており、回折光の方位角方向の死角を可能な限り低減している。合わせてスリットの配置や数、スリット構造全体の剛性を十分に確保する事で高速回転を実現し、最短 5msec での計測も可能となっている。

各スリット円板の素材はタングステン合金であり、ワイヤ放電加工により幅 500 μm のらせん状スリットが形成されている。大小の円板はそれぞれほぼ同一形状の 2 枚で構成され、スリット円板は合計 4 枚である。大小の円板それぞれにおいて、円板間の方位角方向に位相差を与えることで 500 μm 以下の微小な任意のスリット幅に調整できる。スリット形状関数は双曲線関数(sinh)型を採用し、スリット幅をどのような値に設定しても、スリット開口幅が回折角に依存しないように設計されている。

本研究のスリット構造は、上述のスリット構造中心軸をした回転機構の他に、Fig. 2 に示すようなスリット構造の焦点を中心とした旋回移動機構も備えている。この機構を用いることで、スリット円板直径以上の高角の回折 X 線に対しても対応可能であり、従来高エネルギー(短波長)放射光 X 線のみに採用されていた 2 次元検出器用スリットの適用範囲を低エネルギー(長波長)でも使用可能となった。

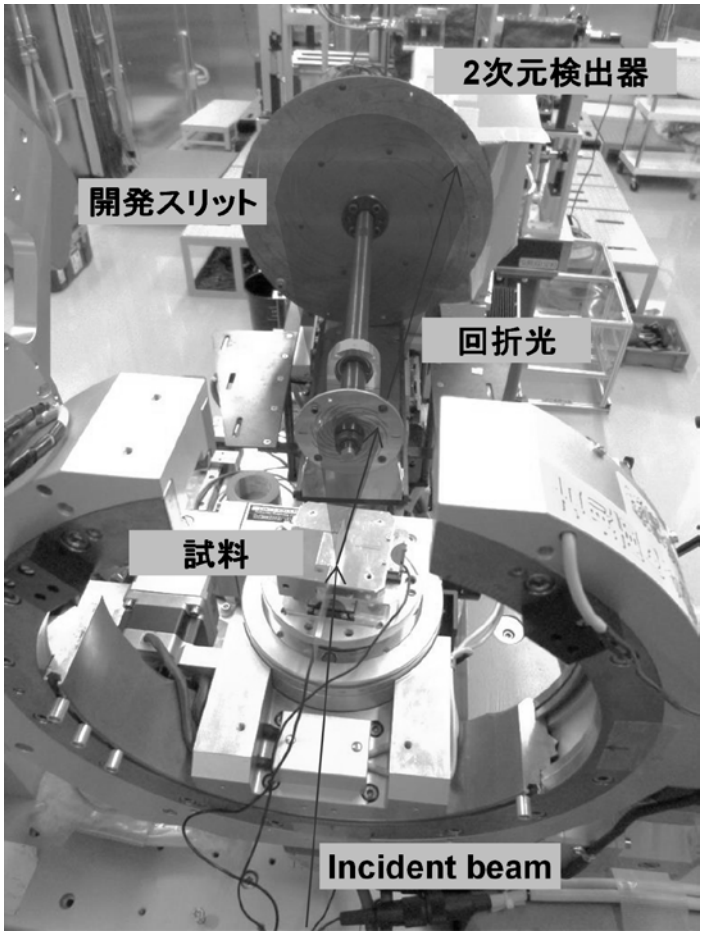

Fig. 1 Overview of XRD measurement setup with developed slit

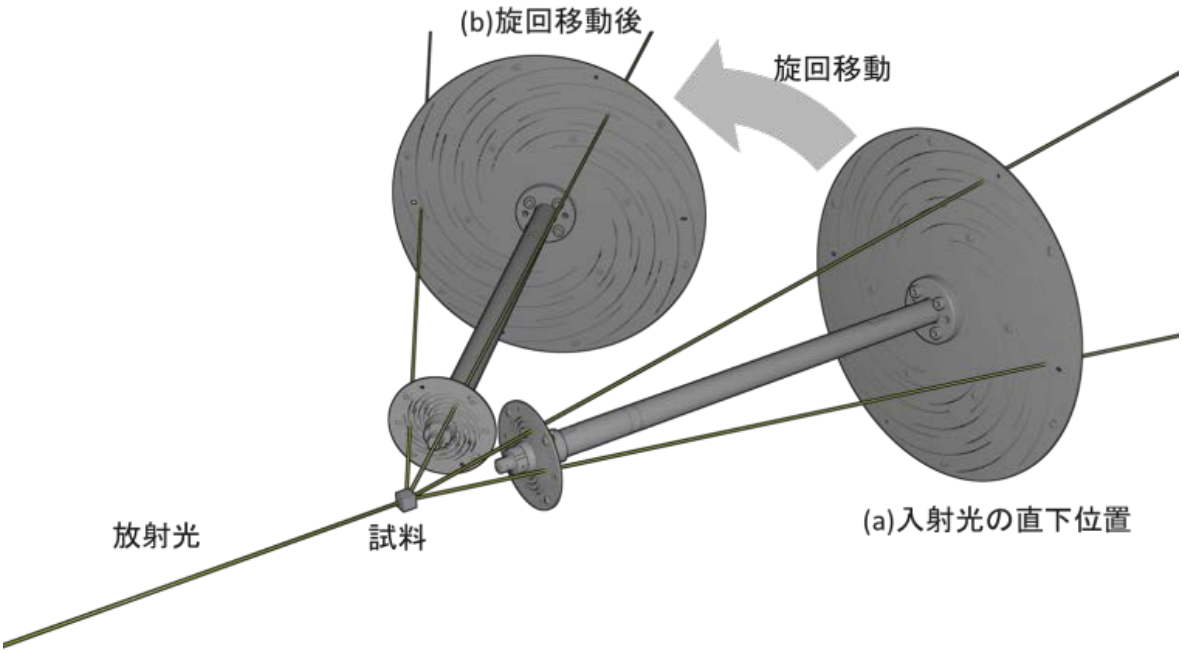

Fig. 2 Schematic drawing of movement of developed slit.
(a) Original location, (b) moved location

実験

開発スリットシステムの空間分解能を利用した計測例として、高回折角測定の例を示す。試料は断面積 0.5mm×0.5mm のアルミニウム超微細粒材からなるワイヤ状試料を用いた。本試料には著しい集合組織はなく、また結晶粒径が非常に微細である事から、スリット幅を数μm 程度としても確実に回折環が得られる事が分かっている。本実験では、この試料を回折計の中心位置に直立させて配置し、開発スリットとその後方の 2 次元検出器を同期させながら適宜旋回移動させることにより、高回折角の計測を試みた。入射光側スリット(発散スリット)は、幅は試料径と等しい 0.5mm とし、高さも 50μm とした。開発スリットのスリット幅は 300μm とした。なお本計測実験に先駆けて、開発スリットの配置を以下の手順で配置した：1．試料を配置していない状態で、入射光が開発スリットの中心軸に設けられたコリメータを通過できるように配置。2．スリットの焦点位置が回折計中心と一致するように設定。

放射光 X 線のエネルギーは 20keV とし、放射光 X 線は試料を貫くように照射して、試験片中で回折・透過した回折光を計測した(いわゆる透過法)。検出器は DECTRIS 社製の PILATUS300K を用い、測定 1 ヶ所あたり 5.0sec の露光時間で回折角を計測した。

結果および考察

Fig. 3 に、開発スリットの旋回移動による Al 超微細粒材の 2 次元回折像を示す。図中の黒色部は 2 次元検出器の不感領域である。本計測における最低角位置(a)では Al の(111)、(200)回折線を捉えることができ、最高角位置(d)の(400)回折線まで、計 6 本の回折環を計測できた。Fig.3 (a)の位置が開発スリットを旋回しない場合の計測結果であり、この場合回折角 15.07deg の(111)面と 17.42deg の(200)面のみの計測となる。これ以上の高指数回折面の計測のためには、放射光 X 線のエネルギーを変更するか、より大寸法のスリットを作製する必要がある。一方、本研究の開発スリットを用いれば、エネルギーを変更することなく Al(400)面の回折角 35.25deg までを捕捉でき、より自由度の高い計測が可能となった。なお、Fig. 3 では回折環の方位角方向の一部のみの計測であるが、試料を入射光回りに回転移動させることで、完全な回折環を得る事も可能である。

今後の課題

本研究では、放射光 X 線と 2 次元検出器を用いて材料内部の応力・ひずみを計測するためのスリットを開発した。開発スリットを用いて、偏心引張試験片内部のひずみ分布を正確に計測できることを確認した。上述の計測例ではスリット幅を 50μm としたが、さらにスリット幅を縮小して高い空間分解能を実現できる能力を有している。また、開発スリットは短時間計測にも対応しており、相変態などの時間分解能を求められる計測も行うことができる。今後、本研究の開発スリットの適用可能性をさらに評価し、新規材料・プロセスの開発・評価に活用していきたい。

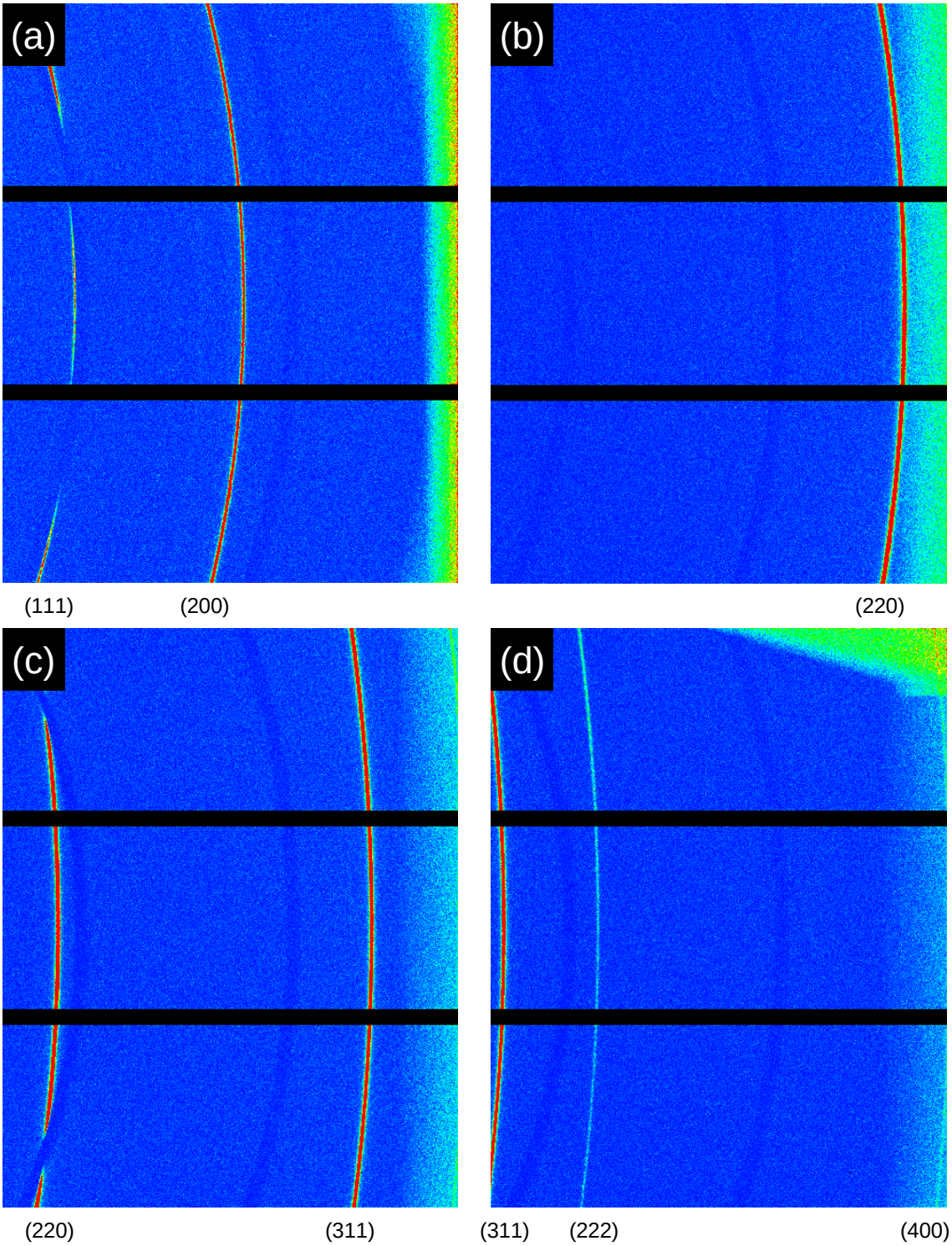

Fig. 3 Diffraction images of Aluminum specimen with developed slit and area detector.
((a) in the lowest angle, and following are in higher angle in alphabetical order)

参考文献

[1] S. F. Nielsen, A. Wolf, H. F. Poulsen, M. Ohler, U. Lienert and R. A. Owen, *J. Sync. Rad.,* **7(2)**, 103–109, (2000).
[2] S. F. Nielsen,“Synchrotron radiation and deformation studies,” Doctoral Dissertation, Risø National Laboratory, (2000).
[3] R. V. Martins and V. Honkimäki, *Text. Microstrct.*, **35(3/4)**, 145–152, (2003).
[4] R. V. Martins and V. Honkimäki, *Mater. Sci. Forum*, **490–491**, 424–429, (2005).
[5] R. V. Martins, C. Ohms and K. Decroos, *Mater. Sci. Eng.*, **527A**, 4779–4787, (2010).
[6] 鈴木賢治、菖蒲敬久、城鮎美、豊川秀訓、保全学、 **11(2)**、99–106, (2012).

謝辞

本スリットの開発では、(独)日本原子力研究開発機構の菖蒲敬久氏および新潟大学の鈴木賢治氏に多大なご助言とご協力を頂きました。ここに感謝を申し上げます。

2013B7021 BL33XU

摩擦面その場 X 線回折による鋼材の焼付き現象解析
In-situ X-ray Diffraction for Frictional Surface during Scuffing of Steel

泉 貴士, 梶田 晴司, 八木 和行, 小屋町 潤, 斉藤 浩二, 遠山 護, 杉村 丈一
Takashi Izumi[a], Seiji Kajita[a], Kazuyuki Yagi[b, c], Jun Koyamachi[b], Koji Saitou[d], Mamoru Tohyama[a], Joichi Sugimura[b, c]

[a](株)豊田中央研究所, [b] 九州大学, [c] カーボンニュートラル・エネルギー国際研究所, [d] トヨタ自動車(株)
[a]Toyota Central R&D Labs., Inc., [b]Kyusyu University, [c] International Institute for Carbon-Neutral Energy Research (I^2CNER), [d] Toyota Motor Corporation.

焼付き過程における鋼材の結晶構造変化をその場(in-situ)で捉えるべく、焼付き過程の鋼材の摩擦面に対して 30Hz の時分割 X 線回折(XRD)を実施した。また、XRD 測定と同時に摩擦面の可視像と温度測定用の近赤外像も取得した。その結果、焼付き時の塑性流動発生と対応して、摩擦面ではマルテンサイトからオーステナイトへの相変態が観察された。このオーステナイトは試験停止(摩擦停止)に伴い元の相であるマルテンサイト/フェライトに戻るため、このような結果はその場分析でのみ得られた結果と考えている。また、近赤外像をからは塑性流動部と対応して強度の高い近赤外光が観察された。これは塑性流動部における局所的な温度上昇を示唆している。

キーワード: 焼付き、鋼、塑性流動、相変態、マルテンサイト、オーステナイト

背景と研究目的

機械要素の摺動部において、焼付きは重大な問題である。摺動部において焼付きが生じると摩擦や摩耗が大幅に増加し、機械として機能しなくなることもあるからである。しかしながら、その機構は十分に解明されておらず、対策も試行錯誤的になっている。そのため焼付き機構の解明とそれに基づいた対策が求められている。

焼付きは摺動材の大きな損傷を引き起こす現象のため、機構解明には焼付き後の摺動材の分析・観察が有効である。一般的に、分析・観察は焼付いた試験片・部品などを使用環境から取り出し、環境外(ex-situ)で行われる。例えば、XRD による焼付き後の鋼材の ex-situ 分析が実施されている[1]。しかしながら、このような ex-situ 分析では以下の問題点があり、それらが機構解明を妨げる一因となっていた。

- 摺動材にはせん断や温度が加わっておらず、摩擦下でのそれとは異なる状況である
- 得られた情報は時間軸上の 1 点での情報であり、その前後の情報が得られない

これらの問題を解決すべく、著者らは焼付き過程の摩擦面をその場(in-situ)で 30Hz の時分割 XRD を用いて分析する手法を開発した。また, この手法では摩擦面の可視像と温度測定用の近赤外像も XRD と同時に取得している。この手法を用い、焼付き過程における鋼材摩擦面の結晶構造や面状態, 温度分布の変化を高い時間分解能で連続的に捉えることで、焼付き現象の機構解明を実施している[2, 3]。

実験

Fig. 1 に、本研究で用いた摩擦面その場分析・観察システムを示す。焼付きは、固定した鋼材試験片に対して回転するサファイアリングを押し付けることで発生させた。摩擦面その場 XRD は、X 線をサファイアリング側面から摩擦面に入射し、摩擦面からの回折 X 線を検出器で検出することで実施した。また、摩擦面の可視像と近赤外像(温度分布測定用)の取得は、透明なサファイア越しに摩擦

面をビデオカメラで観察することで実施した。

摩擦面その場 XRD では、その構成上、入射・回折 X 線が相手材(単結晶サファイア)中を通過する必要がある。そのため、大幅な強度減衰と単結晶サファイアによる回折が生じる. S/N 比を保ちながら時間分解能を高めるため、回折 X 線を十分な強度で得るべく以下を実施した。

①サファイアリングは「X 線光路長の短縮」と「機械的強度」を両立させる独自形状を採用

②X 線のエネルギーはサファイアによる減衰抑制と検出器の検出効率を考慮して 30keV を選択

③単結晶サファイアによる回折スポットが検出器に入らぬよう，入射角度およびサファイアリング試験面の面方位を(0001)面に設定

④検出器は 2 次元検出器(Dectris 社製 PILATUS 300K)を用い，得られた回折リングを円周積分によって積算

これらの工夫により、十分な S/N 比を確保しながら 30Hz で XRD を実施することができた。

Fig. 2 に X 線のサイズと分析範囲を示す。入射 X 線の幅は 1mm であり，高さは全反射ミラーによる集光とスリットを用いて 60μm (FWHM) とした。入射角は，鋼の最強ピーク [bcc (110), fcc(111)] の回折角が 30keV では 11° -12° にあることから、9° とした。この場合の X 線照射範囲は 0.4mm×1mm である。分析深さについては、表面から 7μm の情報が回折強度の 70%を占める。可視光と近赤外光は、それらを同時に撮影可能な 1 台の CCD カメラ(JAI 社製 AD-80CL)を用いて、XRD と同じく 30Hz で取得した。

試験片材質としては、焼き入れ・焼き戻しした SUJ2(軸受鋼)を用いた。試験片形状は直径 4mm、長さ 20mm のピン形状である。片当たりを防止するため，試験供試面は SR12.7mm の曲率を持つ。摩擦試験は、すべり速度 2.38m/s、荷重 280N、大気中無潤滑にて実施した。

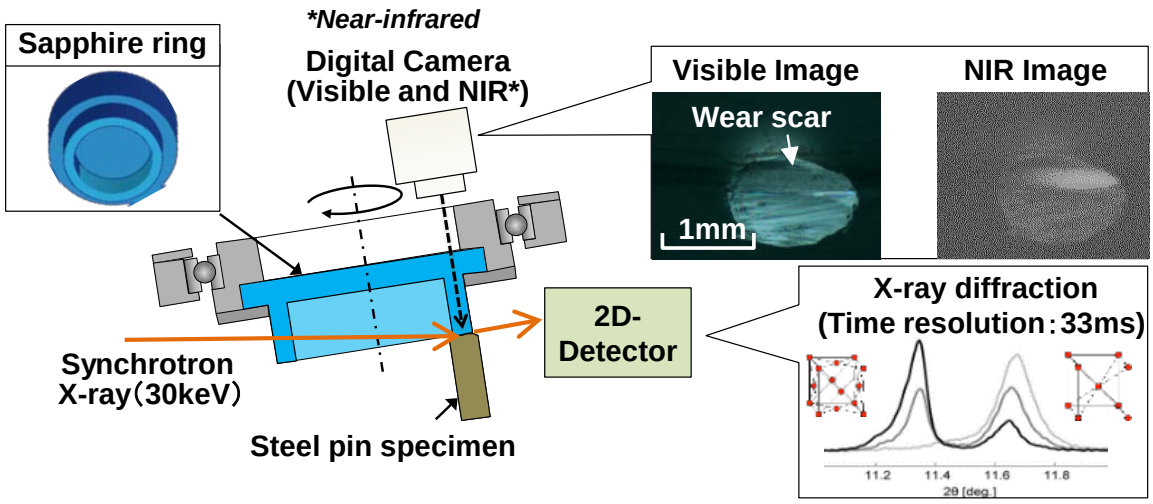

Fig. 1 Schematic of in-situ simultaneous analysis and observation system.

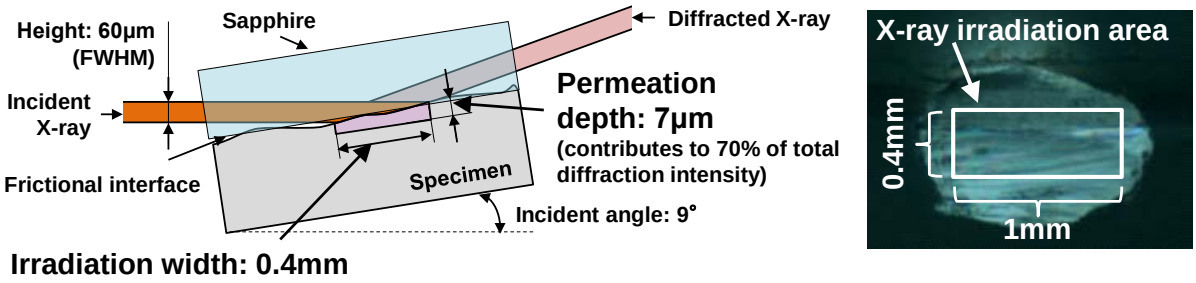

Fig. 2 X-ray irradiation volume on frictional interface.

結果

Fig. 3 に摩擦係数の結果を、Fig. 4 に XRD スペクトルとその時の摩擦面の可視像および近赤外像を示す。摩擦係数が急上昇する直前の 27.30s（図中（a））では、XRD スペクトルからはマルテンサイト［bcc（110）］のみが観察され、可視像では塑性流動は観察されなかった。その 0.03s 後（図中（b））では、XRD スペクトルからはオーステナイト［fcc（111）］のピークがわずかに出現し、可視像では塑性流動が観察された。また近赤外光像では塑性流動部位と対応して強度の高い近赤外光が観察された。その後 27.93s（図中（c））に至るまでの 0.60s 間では、摩擦係数の増大とオーステナイトピーク増加、塑性流動の進展，塑性流動に対応した強度の高い近赤外光が観察された。

これらの結果より、鋼材焼付き時の塑性流動発生と対応して、摩擦面ではマルテンサイトからオーステナイトへの相変態が生じていることが明らかになった。また、流動部位では周囲と比較して高い強度の近赤外光が観察されたため、塑性流動部は周囲と比較して高温であると考えられる。Fig. 4（c）のショルダーはこの局所的な温度上昇を現していると示唆される。

次に、摩擦面その場分析の有効性を評価すべく、試験中(摩擦あり)と試験終了後(摩擦なし)のスペクトルを比較する。Fig. 5 に、試験終了の直前から約 120s 間の XRD スペクトルの推移を示す。166s の試験終了直前では、試験片温度は 800℃以上でありオーステナイトへの変態温度を超えているため、オーステナイトのピークのみが観察される。そこから摩擦を停止すると、5s 後の 171s ではオーステナイトピークは大幅減少し、マルテンサイト/フェライトのピークへと回復していることがわかる。117s 後の 283s のスペクトルでは、ほぼ全てがマルテンサイト/フェライトのピークとなっており、オーステナイトのピークはごくわずかにしか観察されない。

ex-situ 分析で得られるスペクトルは Fig. 5 の 286s のようなスペクトルとなるため、Fig. 5 の 166s や Fig. 4（c）のようなオーステナイトが摩擦面に多量に存在する現象は、摩擦面その場分析だからこそ捉えることができた現象である。

考察

本結果より、塑性流動と対応して、「オーステナイト化」と「局所的な温度上昇」が生じていることが明らかになった。過去の報告より焼付き後の鋼材では残留オーステナイトが観察されることは知られていたが[(1)]、塑性流動との対応は本結果により明らかとなった。

次に、焼付きに対してオーステナイト化と局所的な温度上昇が果たす役割について考察する。オーステナイト化については、オーステナイトはマルテンサイトと比較して「硬さが低く」、また「熱伝導率が低い」ため、これらの 2 点が焼付きに対して悪影響を及ぼしたと考えられる。硬さの低下は一般的に耐摩耗性の低下に繋がるため、摩擦面のオーステナイト化は摩擦面の耐摩耗性の低下に繋がり、焼付き時の高摩擦による摩耗を助長すると考えられる。また，熱伝導率の低下は摩擦面の温度上昇に繋がり、さらなる硬さの低下を引き起こす。局所的な温度上昇についても、硬さの低下を引き起こすことで摩耗を進展させることが考えられる。

今後の課題

焼付き機構の解明には、「塑性流動」と「オーステナイト化」および「局所的な温度上昇」の因果関係を明らかにすることが重要である。しかしながら、本研究では測定系の時間分解能が十分でなくそれらの因果関係はわかっていない。今後は時間分解能を向上させて摩擦面その場 XRD を行い、それらの因果関係の解明を試みる。また今回用いた鋼材は SUJ2 のみであったため、今後は異なる鋼材を用い、塑性流動やオーステナイト化に及ぼす鋼材組成の影響を評価する。

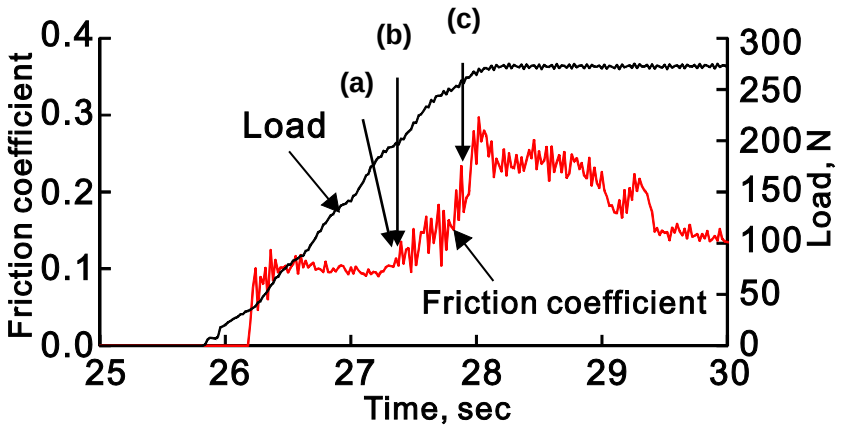

Fig. 3 Transition of friction coefficient and load during the initial period of the test. [(a), (b), (c) in the figure are corresponded to these in Fig. 4]

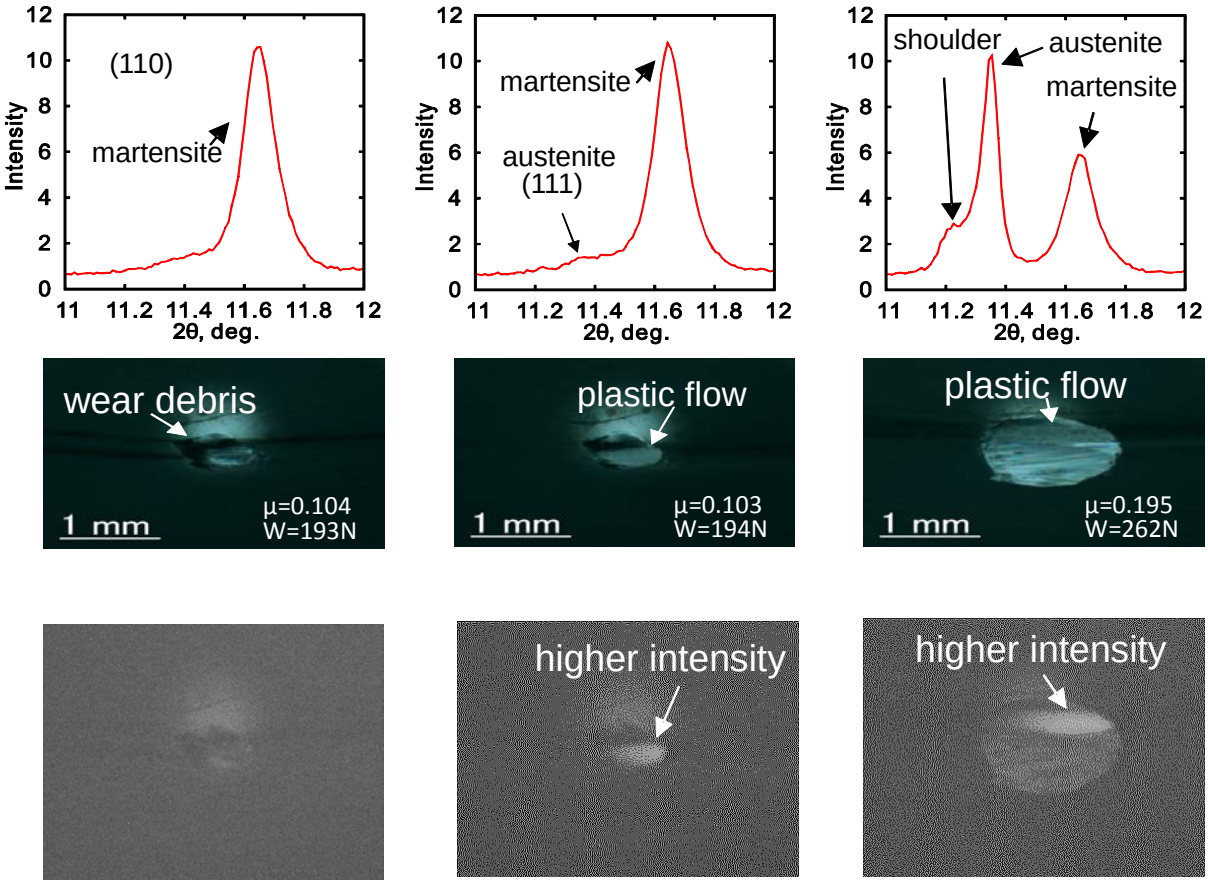

(a) 27.30s (b) 27.33s (c) 29.93s

Fig. 4 XRD spectra, visible images of friction surface and NIR images of friction surface at Fig. 3 (a), (b), (c).

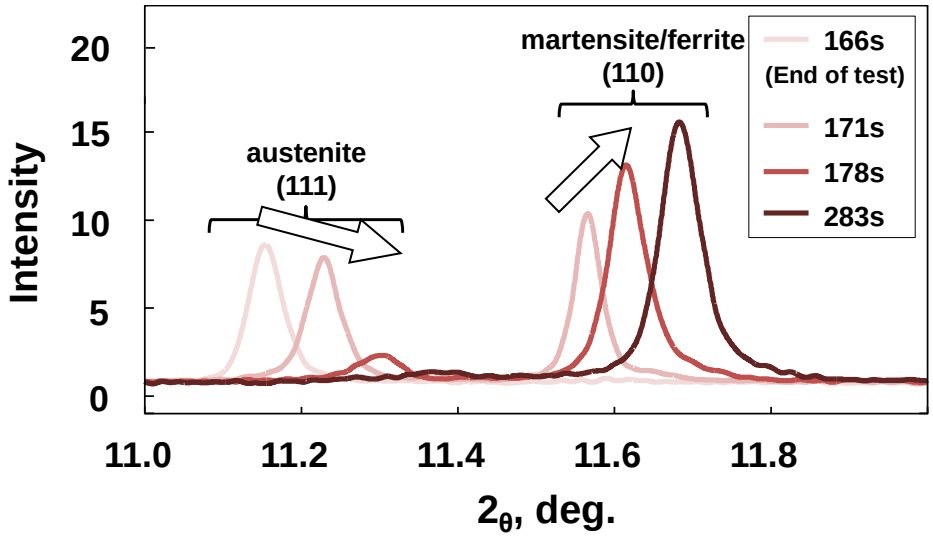

Fig. 5 Transition of XRD spectra at the end of the test.

参考文献

[1] J. Hershberger, O.O. Ajayi, J. Zhang, H. Yoon, G.R. Fenske, ” Formation of austenite during scuffing failure of SAE 4340 steel”, *Wear*, Vol. 256 (2004), pp. 159-167.
[2] 小屋町、八木、梶田、泉、遠山、斉藤、杉村、“トライボロジー会議予稿集 東京”、 2014-5.
[3] 梶田、泉、八木、小屋町、遠山、斉藤、杉村、 ”トライボロジー会議予稿集 東京、 2014-5.

0137013A, 20137013B BL33XU

ゴムの架橋反応解析
Investigation of Crosslinking Reaction on EPDM Rubber

青木 良文, 堂前 和彦, 福森 健三
Yoshifumi Aoki, Kazuhiko Dohmae, and Kenzou Fukumori

(株)豊田中央研究所
Toyota Central R&D Labs., Inc.

エチレン-プロピレン-ジエンゴム(EPDM)の架橋反応について、オイル及びカーボンブラック(HAF)を配合した系にて時分割 XAFS(X 線微細構造解析)法を用いて解析した。架橋反応は XAFS スペクトルの波形分離により酸化亜鉛(ZnO)の各時間における存在量からその減少速度 k(×10-6sec-1)を求め評価した。その結果 HAF を配合した系は架橋速度が上昇すること、及びオイルの増量は架橋速度を低下させることが判明した。さらにこれらを同時に配合した系についても検討したが、変化が複雑になる状況が明らかになった。

キーワード: エチレン-プロピレン-ジエンゴム(EPDM)、酸化亜鉛、架橋反応、減少速度

背景と研究目的

自動車部品の長期の性能確保へのニーズの高まりの中で、ゴムをはじめとする高分子材料の長期耐久寿命や使用中の残存寿命の予測には、熱、酸素などの環境履歴と物性との関係を把握することが重要である。今回、汎用合成ゴムのひとつであるエチレン-プロピレン-ジエンゴム(EPDM)について、実用的な配合を想定し、オイルおよびカーボンブラック(HAF)量を変量した試料を作製し、時分割 XAFS(X 線微細構造解析)測定により、各種条件での酸化亜鉛(ZnO)の変化挙動を追跡した。

実験

ゴム試料は EPDM を主成分としたもので、EPDM100 重量部に対し、酸化亜鉛(ZnO)5重量部、ステアリン酸1重量部および架橋剤(イオウ 1.5 重量部、テトラメチルチウラムジスルフィド(TMTD)1 重量部、2-メルカプトベンゾチアゾール(MBT)0.5 重量部)からなるものを基準配合とし、表 1 に示すように HAF およびオイルを変量したものを試料とした。

調製した試料は厚さ20μmのアルミ箔ではさみ120℃で100μmにシート状に成形された。これらを、アルミ箔をつけたまま直径 30mm の円状に切り出しリングヒータを用いて 160℃で加熱、架橋反応を進行させながら亜鉛化合物について4秒毎の時分割 XAFS 測定を行った。なお当測定は SPring-8 の BL33XU にて実施した。

試料の評価について、Ln(ZnO 残存率:[ZnO]/[Zn])vs.時間(time)プロットの負の傾きより、ZnO の減少速度 k(×10-6sec-1)を求め、その値を比較検討した。

結果

図 1-3 に架橋時の ZnO 減少挙動を示す。

(1)オイル添加の無い系における HAF の配合・増量(PS0→HAF40→HAF80)はkを増大させた、すなわち架橋反応を促進した(図 1)。

(2)HAF を配合しない系におけるオイルの増量(PS0→PSP20→PSP40)は、著しくkを低下させた(図2)。

(3)HAF を 40 重量部添加した系のオイルの増量(HAF40→HAF40P20→HAF40P40)では、(2)に

示したようなオイルの添加によりｋが著しく低下する傾向は見られなかった（図3）。

考察

今回の試料は実用的な配合を仮定して調製されたものである。したがって、架橋反応はより複雑なものになると予想されたが、図 1-3 が示すように、Ln（[ZnO]/[Zn]）と時間との関係は直線関係を示し、この系において、ZnO の減少は以前の報告[1]と同様の一次の反応であると推察された。

図1は基準配合に対し HAF を増量し、その影響を調べた結果である。HAF の増量に伴いkが増加することが確認された。この理由として、硫黄原子がカーボン材料の周りに局在化する傾向が確認されており[2]、おそらく HAF を配合することで高濃度な状態の硫黄及び架橋助剤が実現し、それがZnO の減少反応を促進していると考えられた。

次に、基準配合に対してオイルのみを増量配合した系を調べた。その結果が図2である。この系ではオイルの増量に伴うkの減少が確認された。このことにより、オイルは架橋反応に化学的な寄与は無く、ZnO や硫黄、架橋助剤に対してはそれらの濃度を希釈する働きしか無いからであろうと予想した。

最後に HAF を配合した系に対してオイルを増量する試験を行った。その結果が図3である。HAF のみを配合した試料（HAF40）に対してオイルを 20 重量部配合した試料（HAF40P20）では、前述の予想通り k は減少した。しかしながら、さらに 20 重量部のオイルを増量配合すると（HAF40P40）その k は増加に転じた。これは架橋時における ZnO と硫黄との反応において、HAF とオイルとが与える影響は独立ではないことを示している。例えば、硫黄に対するカーボン表面とオイルとの親和性（活量）の違いや、カーボンを配合することでの ZnO あるいは硫黄の移動を阻害する EPDM の劇的な硬化と、阻害を緩和するオイルの存在とのトレードオフなどが考えられる。今回、このような物質の移動にかかわる部分は考慮に入れられていない。しかしながら、以上の考察についてはより実用的な配合に対しては以上に述べた輸送現象やゴム材料そのもののレオロジーを考慮に入れた検討が必要である。

参考文献

[1] 青木良文、光岡拓也、福森健三、堂前和彦、 第4回豊田ビームライン研究発表会プロシーディング、2013、p16.

[2] 光岡拓也、野中敬正、青木良文、荒木暢、福森健三、第 16 回高分子分析討論会講演要旨集、II-16（2011）.

Table.1 Rubber compositions

Composition	PS0	HAF40	HAF80	PSP20	PSP40	HAF40P20	HAF40P40
EPDM **	100*	100	100	100	100	100	100
HAFcarbon***	0	40	80	0	0	40	40
Paraffin Oil	0	0	0	20	40	20	40
Zinc oxide	5	5	5	5	5	5	5
Stearic acid	1	1	1	1	1	1	1
Sulfur	1.5	1.5	1.5	1.5	1.5	1.5	1.5
TMTD	1	1	1	1	1	1	1
MBT	0.5	0.5	0.5	0.5	0.5	0.5	0.5

*Numerous figures are corresponding to parts per hundred rubber.

**EPDM was EP2(JSR) whose 5-ethylydene-2-norbornene unit is 36.2% on the weight ratio.

*** A kind of hard carbon, High Abrasion Furnace.

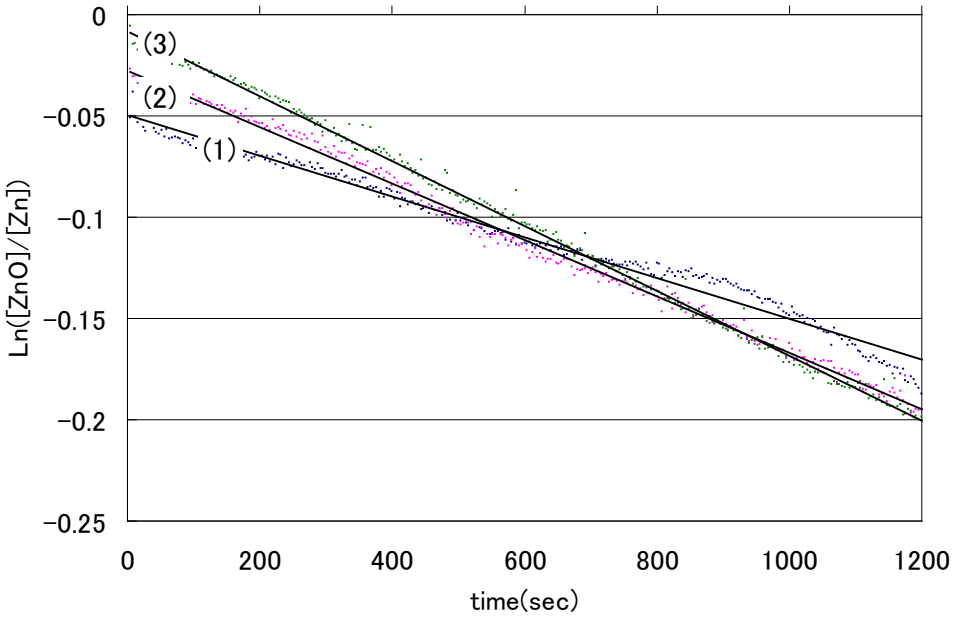

Fig. 1 Decreasing behaviors of ZnO in rubber compounds during crosslinking reaction process at 160C: (1) PS0 (k=100.4), (2) HAF40 (k=139.2) and (3) HAF80 (k=160.2).

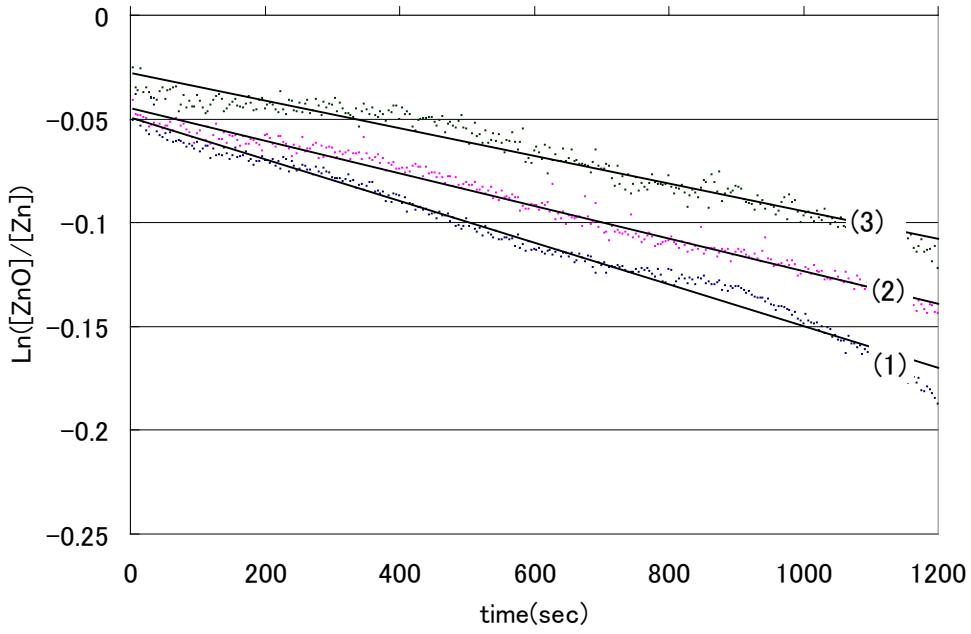

Fig. 2 Decreasing behaviors of ZnO in rubber compounds during crosslinking reaction process at 160C: (1) PS0 (k=100.4), (2) PSP20 (k=78.4) and (3) PSP40 (k=66.5).

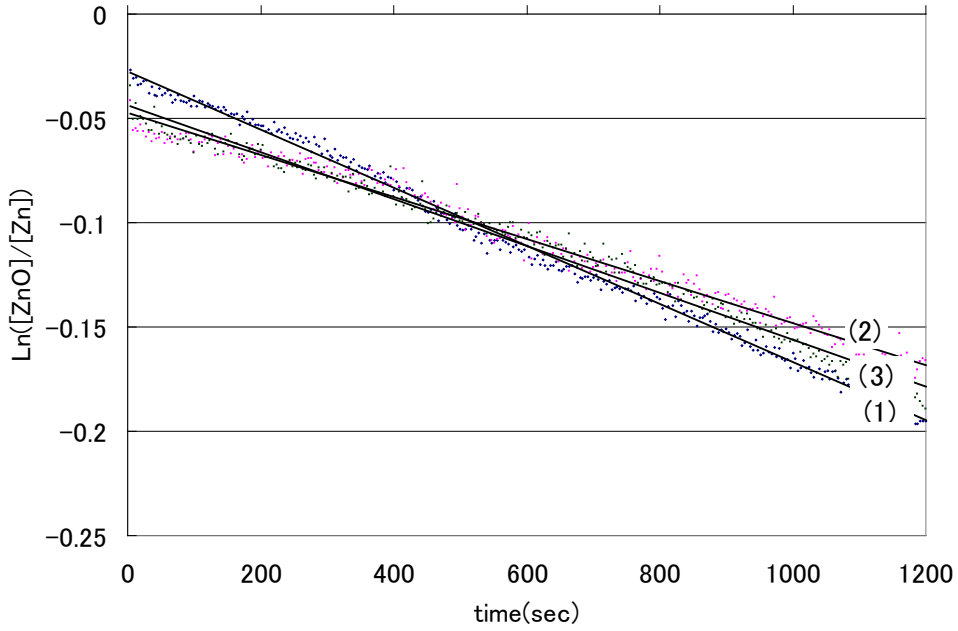

Fig. 3 Decreasing behaviors of ZnO in rubber compounds during crosslinking reaction process at 160C: (1) HAF40 (k=139.2), (2) HAF40P20 (k=100.5) and (3) HAF40P40 (k=112.3).

J Polym Res (2014) 21:488
DOI 10.1007/s10965-014-0488-2

ORIGINAL PAPER

Effects of metal loading and magnetic field strength on alignment of noncrystalline block copolymers doped with metal complexes

Hiroaki Wakayama · Hirotaka Yonekura · Masashi Harada

Received: 11 March 2014 / Accepted: 19 May 2014

Abstract Control of the orientation of block copolymers in self-assembled nanostructures is important for their applications in organic semiconductors, lithographic nanopatterning, separation membranes, and nanofabrication templates. We recently reported that addition of magnetically sensitive metal complexes to block copolymers can be used to align the block copolymers under the influence of a magnetic field. In the present study, we investigated the mechanism of magnetic alignment of block copolymers doped with metal complexes. Specifically, we used small-angle X-ray scattering analysis to evaluate the effects the metal complex molar ratio and the strength of the applied magnetic field have on magnetic alignment in block copolymer–metal composites. Two Fe precursors, tricarbonyl(cyclooctatetraene) iron and acetylacetonate iron(III), and one Pt precursor, platinum dimethylcyclooctadiene, were selectively introduced into separate polymer blocks of a block copolymer, polystyrene-*block*-poly(2-vinylpyridine) (PS-P2VP, 102 k/97 k) or polystyrene-*block*-poly(4-vinylpyridine) (PS-P4VP, 40 k/5.6 k), and the resulting films were annealed in a magnetic field. We found that magnetic alignment of the block copolymers was enhanced by high metal complex molar ratios and high magnetic field strength. The lamellar structures of the self-assembled PS-P2VP(102 k/97 k) composites were disturbed when the amounts of the metal complexes were increased, and magnetic alignment of the lamellar structures was enhanced when the strength of the applied magnetic field was increased. Magnetic alignment induced shrinkage of the cylindrical structures of the self-assembled PS-P4VP(40 k/5.6 k) composites with high metal complex ratios.

H. Wakayama (✉) · H. Yonekura · M. Harada
Toyota Central R&D Laboratories, Inc., Nagakute,
Aichi 480-1192, Japan
e-mail: wakayama@mosk.tytlabs.co.jp

Published online: 10 June 2014

Reprinted from Journal of Polymer Research, Vol. 21, pp. 488-494
(http://dx.doi.org/10.1007/s10965-014-0488-2), © 2014

Keywords Self-assembly · Block copolymers · Magnetic alignment · Nanomaterials

Introduction

Block copolymers are attracting much attention because of their ability to self-assemble into periodically ordered nanostructures. Control of the orientation of the block copolymers in such nanostructures is important for their applications in organic semiconductors [1–3], lithographic nanopatterning [4–6], separation membranes [7–9], and nanofabrication templates [10–12]. Many studies have focused on orienting block copolymers by applying stress [13–16], electric fields [17–19], and magnetic fields [20–24]. In the latter case, self-assembly of block copolymers that exhibit anisotropic magnetic susceptibility, such as liquid-crystalline block copolymers, is directed by application of a magnetic field; alignment of the block copolymers is achieved by means of orientation of the liquid-crystal mesogens. However, this approach is limited to crystalline block copolymers with anisotropy.

To expand this methodology to other types of block copolymers, including noncrystalline block copolymers, investigators have introduced magnetically sensitive additives into a specific polymer block of block copolymers. For example, introduction of a ligand containing a biphenyl moiety that interacts with the poly(acrylic acid) block of a poly(styrene-*block*-acrylic acid) block copolymer by hydrogen bonding has been shown to impart magnetic susceptibility, which in turn facilitates magnetic alignment of the block copolymer–ligand composite [25]. However, this method is limited by the need for a specific interaction (i.e., hydrogen bonding) between the block copolymer and the ligand.

Recently we reported a synthetic route to inorganic nanoheterostructures by templating block copolymer

self-assembly [26]. Metal complexes are introduced into a specific copolymer block, and subsequent removal of the block copolymers by pyrolysis produces self-assembled inorganic spheres, cylinders, or layers in a matrix. In addition, the morphology of the block copolymer–metal complex composite can be transformed (from spheres to cylinders) by application of a magnetic field. By means of this method, many kinds of ligands can be introduced into noncrystalline polymer blocks, and in particular magnetic susceptibility can be imparted to many kinds of block copolymers, which can then be magnetically aligned. The elucidation of the orientation mechanism in block copolymer-metal complex composites leads to the improvement in the material properties of the block copolymer composites as well as the inorganic nanohetero materials produced after the pyrolytic removal of the block copolymer.

Here, we describe in detail the mechanism of magnetic alignment of block copolymers doped with metal complexes; specifically, we describe the effects of the metal complex molar ratio and the strength of the applied magnetic field on magnetic alignment.

Experimental section

Preparation of block copolymer composites

Tricarbonyl(cyclooctatetraene) iron ($CtFe(CO)_3$, >96 %, Tokyo Chemical Industry), dimethyl(1,5-cyclooctadiene) platinum(II) ($PtMe_2COD$, 99 %, Wako Pure Chemical Industries), and acetylacetonate iron(III) ($Fe(acac)_3$, 99 %, Wako) were dissolved in a 0.5 wt.% solution of polystyrene-*block*-poly(2-vinylpyridine) (PS-P2VP, M_n^{PS}=102 kg mol^{-1}, M_n^{P2VP}=97 kg mol^{-1}, polydispersity index = 1.12, Polymer Source) in toluene (>99.5 %, Wako). Several solutions were prepared, and in each solution the $CtFe(CO)_3$/styrene, $PtMe_2COD$/vinylpyridine, and $Fe(acac)_3$/vinylpyridine molar ratios were the same, ranging from 0 to 1.0. After stirring for 3 h, each solution was sprayed onto a Kapton film, and the samples were annealed at 453 K for 6 h in a magnetic field (0–10 T) applied parallel to the film. In some of the experiments, polystyrene-*block*-poly-(4-vinylpyridine) (PS-P4VP, M_n^{PS}= 40 kg mol^{-1}, M_n^{P4VP}=5.6 kg mol^{-1}, polydispersity index = 1.10, Polymer Source) was used in place of the PS-P4VP(102 k/97 k).

Characterization of block copolymer composites

Scanning transmission electron microscopy of the resulting composites was conducted with a high-resolution transmission electron microscope (JEM-2010FEF, JEOL) operating at 200 keV. In addition, small-angle X-ray scattering (SAXS) measurements were performed on the BL33XU beamline at SPring-8 (Hyogo, Japan). The incident X-rays were applied normal to the samples for through-view images and parallel to the samples (and in the direction of the applied magnetic field) for cross-view images.

Results and discussion

Scanning transmission electron microscopy

Scanning transmission electron microscopy images of samples that were prepared with PS-P2VP(102 k/97 k) and PS-P4VP(40 k/5.6 k) and metal complexes at molar ratios of 1.0 and that were annealed in a 10 T magnetic field showed lamellar and cylindrical structures, respectively, that were almost exactly parallel to the direction of the applied magnetic field (Fig. 1).

Effects of metal complex molar ratio and magnetic field strength on block copolymer composite structure

Through-view images obtained by applying X-rays normal to the samples prepared with PS-P2VP(102 k/97 k) and PS-P4VP(40 k/5.6 k) (metal complex molar ratio, 1.0; magnetic field, 10 T) showed isotropic two-dimensional patterns (Fig. 2). Figure 3 shows the one-dimensional SAXS profiles obtained from the circular integral of the scattering intensity at the distance from the scattering center. In the SAXS pattern of a sample prepared with PS-P4VP(102 k/97 k) without metal complexes and at magnetic field strength of 10 T, the relative positions of the 1:2:3 peaks confirmed that the sample had a lamellar structure (Fig. 3a metal complex molar ratio, 0.0; blue line). As the amounts of the metal complexes were increased, the first peaks broadened (Fig. 3a), which suggests that the lamellar structures were disturbed by introduction of the metal complexes. The first peaks become sharp as the strength of the applied magnetic field was increased

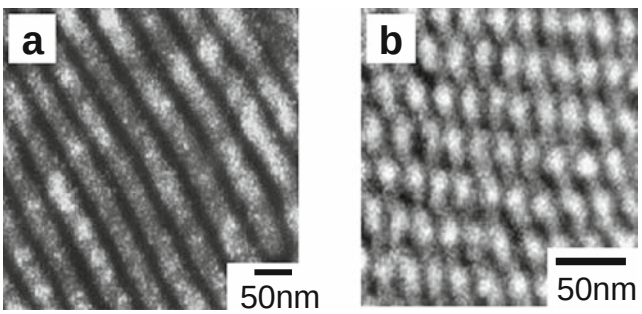

Fig. 1 Scanning transmission electron microscopy images of samples prepared from (**a**) PS-P2VP(102 k/97 k) and (**b**) PS-P4VP(40 k/5.6 k) and metal complexes (1.0 molar ratio) and annealed in a 10 T magnetic field

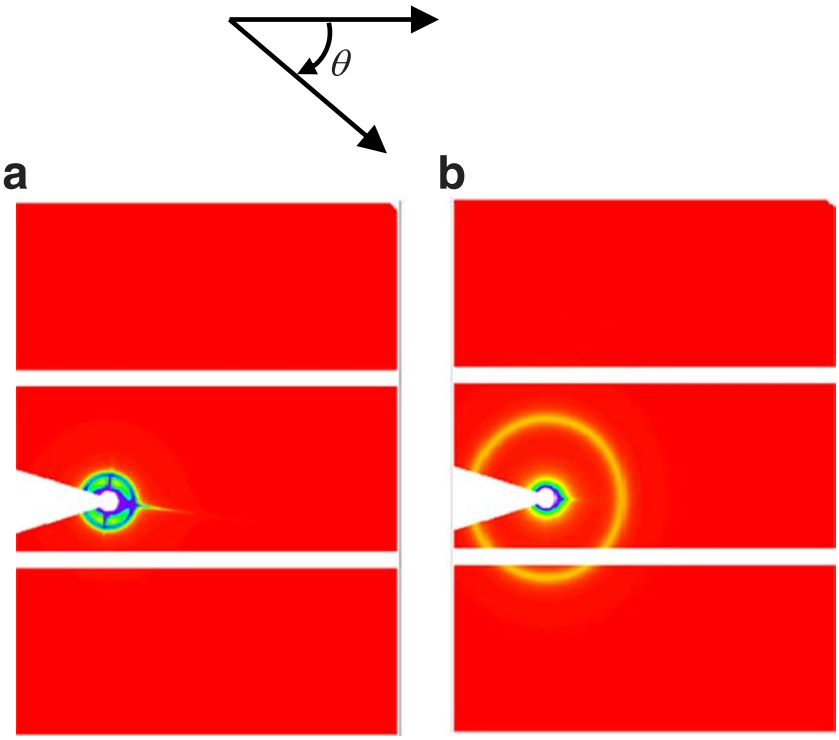

Fig. 2 Two-dimensional scattering patterns in through-view images obtained by applying X-rays normal to samples prepared with (**a**) PS-P2VP(102 k/97 k) and (**b**) PS-P4VP(40 k/5.6 k) and metal complexes (1.0 molar ratio) and annealed in a 10 T magnetic field

(Fig. 3b). This result is attributable to magnetic alignment of the self-assembled lamellar structures.

As was the case for the SAXS pattern of the sample prepared with PS-P2VP(102 k/97 k), in the SAXS pattern of the sample prepared with PS-P4VP(40 k/5.6 k), the first peaks broadened as the amounts of metal complexes were increased (Fig. 3c), and the first peaks become sharp as the strength of the applied magnetic field was increased (Fig. 3d), suggesting magnetic alignment of the self-assembled cylindrical structures. As shown in Fig. 3d, the peaks at relative positions of 1:

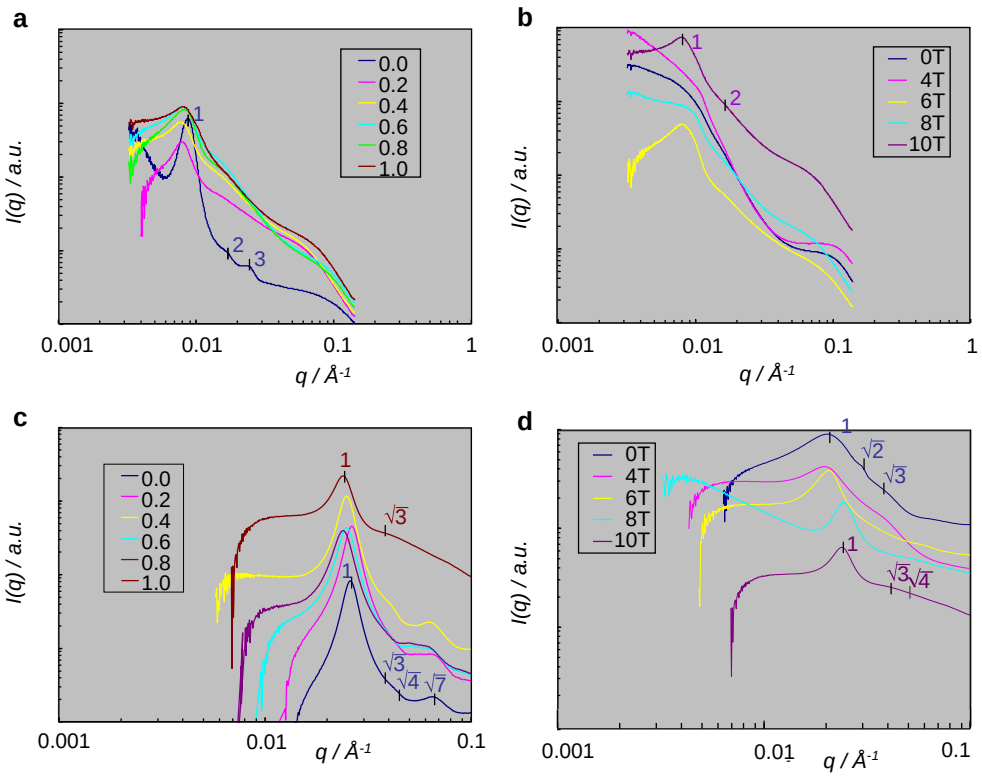

Fig. 3 Effects of metal complex molar ratio (magnetic field, 10 T; *left panels*) and magnetic field strength (metal complex molar ratio, 1.0; *right panels*) on one-dimensional small-angle X-ray scattering profiles obtained from the circular integral of the scattering intensity at the distance from the scattering center: **a**, **b** PS-P2VP(102 k/97 k) and **c**, **d** PS-P4VP(40 k/5.6 k)

√2:√3 for the samples prepared with PS-P4VP(40 k/5.6 k) in the absence of a magnetic field (Fig. 3d magnetic field, 0 T; blue line) and the peaks at relative positions of 1: √3:√4 for the samples prepared with PS-P4VP(40 k/5.6 k) and annealed in a high magnetic field (Fig. 3d magnetic field, 10 T; purple line) confirmed the spherical and hexagonal cylinder structures, respectively, of these samples. That is, application of a magnetic field to the PS-P4VP(40 k/5.6 k)–metal complex composite resulted in a phase transition from spheres to hexagonal cylinders.

Effects of metal complex molar ratio and magnetic field strength on the repeat size of the block copolymer composites

In the through-view images of the block copolymer composites(Fig. 4), the repeat size of samples prepared with PS-P2VP(102 k/97 k) and PS-P4VP(40 k/5.6 k) and annealed in a 10 T magnetic field increased with increasing metal complex molar ratio up to a ratio of 0.6, whereas at ratios higher than 0.6, the repeat size decreased. This result suggests that the polymer blocks of the microphase-separated structures were swollen by the introduction of metal complexes at molar ratios of <0.6 and that shrinkage was induced by magnetic alignment of the samples containing magnetically sensitive metal complexes at molar ratios of >0.6. As shown in Fig. 5, the repeat sizes of samples prepared with PS-P2VP(102 k/97 k) and PS-P4VP(40 k/5.6 k) decreased with increasing magnetic field strength at values of >6 T, suggesting magnetic alignment of the block copolymer composite structures.

Azimuthal angle dependence of peak intensity

The azimuthal angle dependence of the intensity of the first peak in the through-view images of samples prepared with PS-P2VP(102 k/97 k) and PS-P4VP(40 k/5.6 k)

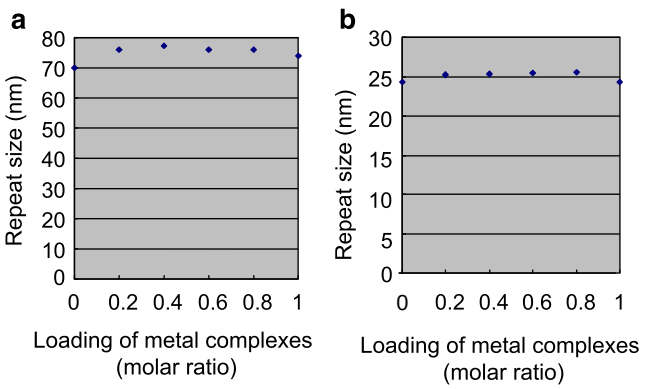

Fig. 4 Effects of metal complex molar ratio on the repeat size of block copolymer composites prepared with (**a**) PS-P2VP(102 k/97 k) and (**b**) PS-P4VP(40 k/5.6 k) annealed in a 10 T magnetic field

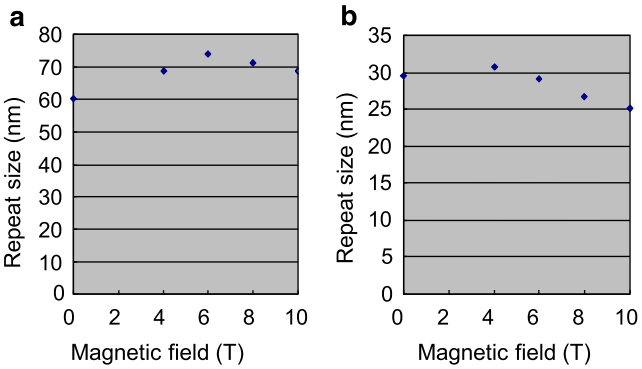

Fig. 5 Effect of magnetic field strength on the repeat size of block copolymer composites prepared from (**a**) PS-P2VP(102 k/97 k) and (**b**) PS-P4VP(40 k/5.6 k) and metal complexes (1.0 molar ratio)

(metal complex molar ratio, 1.0; magnetic field strength, 10 T) is shown in Fig. 6; the intensity of the first peak was almost independent of the azimuthal angle; no clear orientation induced by the magnetic field was observed. The results for the cross-view images are shown in Fig. 7 at the various metal complex molar ratios and magnetic field strengths. The intensities of the first peaks were maximal in the normal direction (0° and 180°) for the samples prepared with PS-P2VP(102 k/97 k) and PS-P4VP(40 k/5.6 k). This suggests that the self-assembled structures were oriented parallel to the film samples. For both PS-P2VP(102 k/97 k) and PS-P4VP(40 k/5.6 k), the peak intensity increased as the strength of the applied magnetic field was increased (Fig. 7a, c) and as the amounts of metal complexes were increased (Fig. 7b, d). Samples prepared with PS-P2VP(102 k/97 k) (metal complex molar ratio, 0.0; magnetic field strength, 10 T) exhibited small peaks at around 90° and 270° (Fig. 7b blue line), which were attributed to disturbance of the orientation of the lamellar structures. In contrast, broad peaks at 50–150° and 230–330° were observed for the samples that were prepared with PS-P4VP(40 k/5.6 k) annealed at high magnetic field strength (Fig. 7c magnetic field strength, 10 T: purple line) or the samples that were

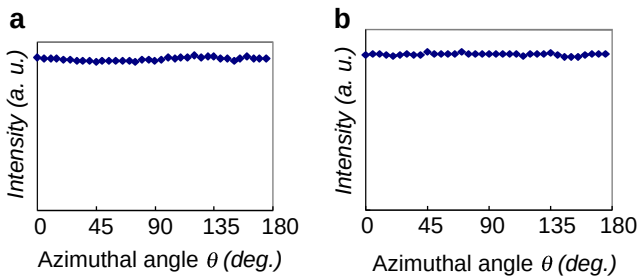

Fig. 6 Azimuthal angle dependence of the intensity of the first peak in the through-view images of composites prepared with (**a**) PS-P2VP(102 k/97 k) and (**b**) PS-P4VP(40 k/5.6 k) and metal complexes (1.0 molar ratio) and annealed in a 10 T magnetic field

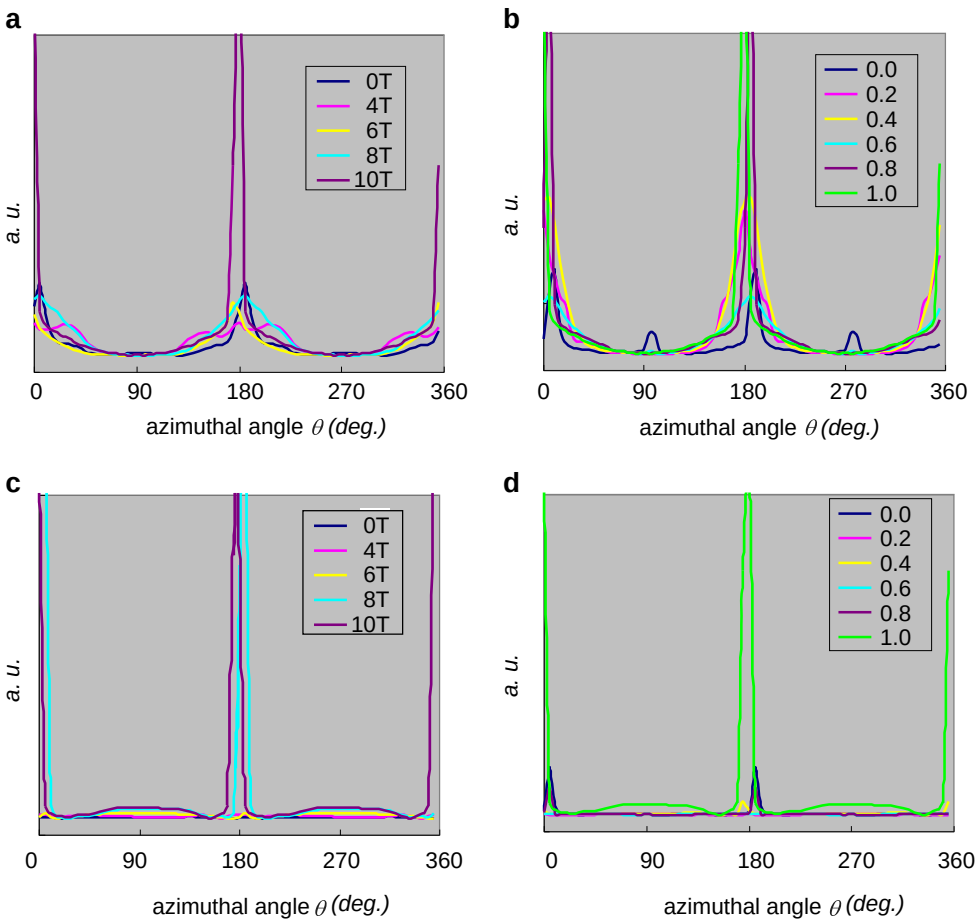

Fig. 7 Effects of magnetic field strength (metal complex molar ratio, 1.0; *left panels*) and metal complex molar ratio (magnetic field, 10 T; *right panels*) on the azimuthal angle dependence of the intensity of the first peak in the cross-view images of composites prepared with (**a**, **b**) PS-P2VP(102 k/97 k) and (**c**, **d**) PS-P4VP(40 k/5.6 k)

prepared with PS-P4VP(40 k/5.6 k) and a large amount of metal complexes (Fig. 7d metal complex molar ratio, 1.0: light green line). These broad peaks were due to the high orientation of the hexagonally packed cylindrical structures [27]. The highly oriented cylindrical structures were induced by a high loading of metal complexes and by annealing in a high-strength magnetic field.

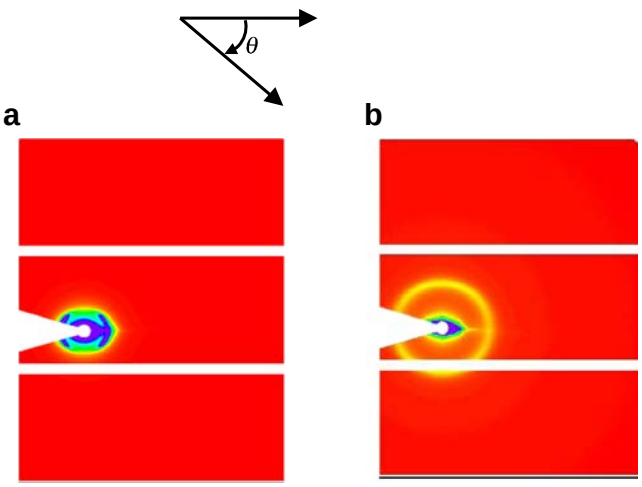

Fig. 8 Two-dimensional scattering patterns in cross-view images obtained by applying X-rays parallel to composites prepared with (**a**) PS-P2VP(102 k/97 k) and (**b**) PS-P4VP(40 k/5.6 k) and metal complexes (1.0 molar ratio) and annealed in a 4 T magnetic field

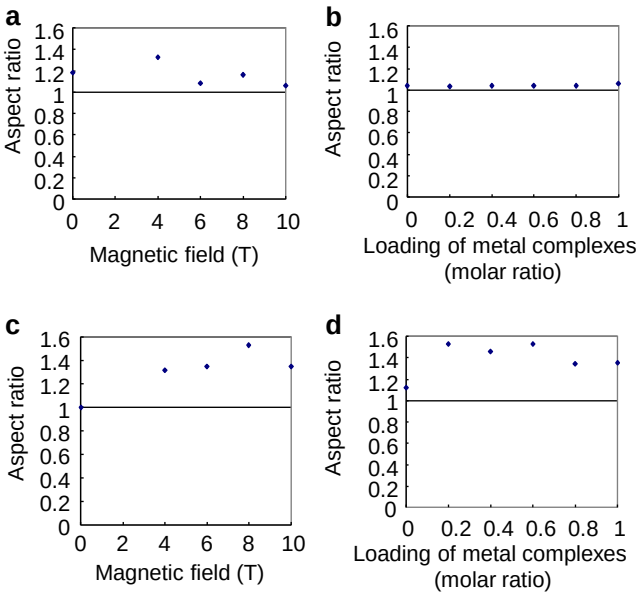

Fig. 9 Effects of magnetic field strength (metal complex molar ratio, 1.0; *left panels*) and metal complex molar ratio (magnetic field, 10 T; *right panels*) on the aspect ratio of the scattering ring: **a**, **b** PS-P4VP(40 k/5.6 k) and **c**, **d** PS-P2VP(102 k/97 k)

Ellipse aspect ratio of two-dimensional SAXS pattern

For the PS-P2VP(102 k/97 k) and PS-P4VP(40 k/5.6 k) samples prepared at a metal complex molar ratio of 1.0 and a magnetic field strength of 10 T, the intensity of the first peak in the through-view images were almost independent of the azimuthal angle (Fig. 6), and the aspect ratio of the scattering ring in the two-dimensional SAXS pattern was almost 1 (Fig. 2), suggesting isotopic scattering. Figure 8 shows the two-dimensional cross-view SAXS patterns for the PS-P2VP(102 k/97 k) and PS-P4VP(40 k/5.6 k) samples prepared at a metal complex molar ratio of 1.0 and a magnetic field strength of 4 T. The fact that the scattering ring for the sample prepared with PS-P4VP(40 k/5.6 k) had an oval shape extending in the equatorial direction (Fig. 8b) indicates that the repeat size of the cylindrical structure was smaller in the normal direction of the film samples than in the parallel direction. As the magnetic field strength was increased, the aspect ratio of the scattering ring approached 1 (Fig. 9a), which suggests that the cylindrical structures of PS-P4VP(40 k/5.6 k) were aligned by the application of the magnetic field and that the alignment reduced distortion of the hexagonally packed structures [28]. For the lamellar structures from PS-P2VP(102 k/97 k), it is considerable that anisotropy of the vertical and horizontal direction occurred in the polymer block, such as polymer density, induced by the application of magnetic field.

Conclusions

To investigate the mechanism of magnetic alignment of block copolymers, we examined the effects of metal complex molar ratio and magnetic field strength on magnetic alignment in self-assembled block copolymer composites. We found that alignment was enhanced by high metal complex molar ratio and high magnetic field strength. As the amounts of metal complexes in the composites were increased, the lamellar structures were disturbed. The magnetic alignment of the lamellar structures was enhanced by increasing the strength of the applied magnetic field. For cylindrical structures, shrinkage was induced by magnetic alignment of samples prepared at high metal complex molar ratios. Our results can be expected to contribute to the extension of magnetic alignment methods to various kinds of block copolymers including noncrystalline block copolymers. The control of the orientation in block copolymer-metal complex composites leads to the improvement in the material properties of the block copolymer composites as well as the inorganic nanohetero materials produced after the pyrolytic removal of the block copolymer. Our approach is simple and widely applicable for the synthesis of heterogeneous nanostructured materials with controlled oriented structures.

Acknowledgments The SAXS experiments were performed on the BL33XU beamline at SPring-8 with the approval of the Japan Synchrotron Radiation Research Institute (JASRI; proposal no. 2013B7003). We acknowledge T. Matsunaga for analysis of SAXS data.

References

1. Zorn M, Zentel R (2008) Liquid crystalline orientation of semiconducting nanorods in a semiconducting matrix. Macromol Rapid Commun 29:922–927
2. Tao Y, Ma B, Segalman RA (2008) Self-assembly of rod-coil block copolymers and their application in electroluminescent devices. Macromolecules 41:7152–7159
3. Lee YJ, Kim SH, Yang H, Jang M, Hwang SS, Lee HS, Baek KY (2011) Vertical conducting nanodomains self-assembled from poly(3-hexyl thiophene)-based diblock copolymer thin films. J Phys Chem C 115:4228–4234
4. Jung YS, Ross CA (2007) Orientation-controlled self-assembled nanolithography using a polystyrene-polydimethylsiloxane block copolymer. Nano Lett 7:2046–2050
5. Ramanathan M, Nettleton E, Darling SB (2009) Simple orientational control over cylindrical organic–inorganic block copolymer domains for etch mask applications. Thin Solid Films 517:4474–4478
6. Xie N, Li WH, Qiu F, Shi AC (2013) New strategy of nanolithography via controlled block copolymer self-assembly. Soft Matter 9:536–542
7. Rzayev J, Hillmyer MA (2005) Nanochannel array plastics with tailored surface chemistry. J Am Chem Soc 127:13373–13379
8. Barbi V, Funari SS, Gehrke R, Scharnagl N, Stribeck N (2003) SAXS and the gas transport in polyether-block-polyamide copolymer membranes. Macromolecules 36:749–758
9. Armstrong S, Freeman B, Hiltner A, Baer E (2012) Gas permeability of melt-processed poly(ether block amide) copolymers and the effects of orientation. Polymer 53:1383–1392
10. Li M, Ober CK (2006) Block copolymer patterns and templates. Mater Today 9:30–39
11. Lee JI, Cho SH, Park SM, Kim JK, Kim JK, Yu JW, Kim YC, Russell TP (2008) Highly aligned ultrahigh density arrays of conducting polymer nanorods using block copolymer templates. Nano Lett 8:2315–2320
12. Chai J, Buriak JM (2008) Using cylindrical domains of block copolymers to self-assemble and align metallic nanowires. ACS Nano 2:489–501
13. Laiho A, Hiekkataipale P, Ruokolainen J, Ikkala O (2009) Directing the smectic layer orientation by shear flow in hierarchical lamellar-within-lamellar liquid crystalline diblock copolymers. Macromol Chem Phys 210:1218–1223
14. Koppi KA, Tirrell M, Bates FS, Almdal K, Colby RH (1992) Lamellae orientation in dynamically sheared diblock copolymer melts. J Phys II 2:1941–1959
15. Honeker CC, Thomas EL (1996) Impact of morphological orientation in determining mechanical properties in triblock copolymer systems. Chem Mater 8:1702–1714

16. Mai B, Li Z, Liu R, Feng S, Wu Q, Liang G, Gao H, Zhu F (2013) Confined crystallization of core-forming blocks in nanoscale self-assembled micelles of poly(ε-caprolactone)-b-poly(ethylene oxide) in aqueous solution. J Polym Res. doi: 10.1007/s10965-013-0299-x
17. Thurn-Albrecht T, DeRouchey J, Russell TP, Kolb R (2002) Pathways toward electric field induced alignment of block copolymers. Macromolecules 35:8106–8110
18. Elhadj S, Woody JW, Niu VS, Saraf RF (2003) Orientation of self-assembled block copolymer cylinders perpendicular to electric field in mesoscale film. Appl Phys Lett 82:871–873
19. Tsori Y, Andelman D (2002) Thin film diblock copolymers in electric field: transition from perpendicular to parallel lamellae. Macromolecules 35:5161–5170
20. Tao YF, Zohar H, Olsen BD, Segalman RA (2007) Hierarchical nanostructure control in rod-coil block copolymers with magnetic fields. Nano Lett 7:2742–2746
21. Gopinadhan M, Majewski PW, Osuji CO (2010) Facile alignment of amorphous poly(ethylene oxide) microdomains in a liquid crystalline block copolymer using magnetic fields: toward ordered electrolyte membranes. Macromolecules 43:3286–3293
22. Grigorova T, Pispas S, Hadjichristidis N, Thurn-Albrecht T (2005) Magnetic field induced orientation in diblock copolymers with one crystallizable block. Macromolecules 38:7430–7433
23. Tomikawa N, Lu ZB, Itoh T, Imrie CT, Adachi M, Tokita M, Watanabe J (2005) Orientation of microphase-segregated cylinders in liquid crystalline diblock copolymer by magnetic field. Jpn J Appl Phys 2(44):L711–L714
24. Tran H, Gopinadhan M, Majewski PW, Shade R, Steffes V, Osuji C, Campos LM (2013) Monoliths of semiconducting block copolymers by magnetic alignment. ACS Nano 7:5514–5521
25. Gopinadhan M, Majewski PW, Beach ES, Osuji CO (2012) Magnetic field alignment of a diblock copolymer using a supramolecular route. ACS Macro Lett 1:184–189
26. Wakayama H, Yonekura H, Kawai Y (2013) Three-dimensional periodically ordered nanohetero metallic materials from self-assembled block copolymer composites. ACS Macro Lett 2:284–287
27. Sakurai S (2008) Progress in control of microdomain orientation in block copolymers–efficiencies of various external fields. Polymer 49: 2781–2796
28. Sakurai S, Momii T, Taie K, Shibayama M, Nomura S, Hashimoto T (1993) Morphology transition from cylindrical to lamellar microdoains of block copolymers. Macromolecules 23:485–491

Materials Science Forum Vol. 777 (2014) pp 142-147
Online available since 2014/Feb/06 at www.scientific.net

doi:10.4028/www.scientific.net/MSF.777.142

豊田ビームライン研究発表会プロシーディングス 5, (2014)

Crystal Plasticity finite element analysis based on crystal orientation mapping with three-dimensional x-ray diffraction microscopy

Daigo Setoyama[a *], Yujiro Hayashi[b] and Noritoshi Iwata[c]

Toyota Central R&D Labs., Inc., Nagakte, Aichi 480-1192, Japan

[a]daigo@mosk.tytlabs.co.jp, [b]y-hayashi@mosk.tytlabs.co.jp, [c]noriiwata@mosk.tytlabs.co.jp

Keywords: crystal plasticity, finite element analysis, polycrystalline iron, three-dimensional x-ray diffraction, crystallographic orientation mapping

Abstract. In other study we examined the plastic behavior for polycrystalline iron by three-dimensional x-ray diffraction (3DXRD) experiment. In this study we analyze the behavior by crystal plasticity finite element (CPFE) analysis, to confirm the validity of application to the deformation analysis of engineering steels of a couple of constitutive models. In the CPFE analysis, the observed microstructure and its crystal orientation are modeled with finite elements to take the inter-granular and intra-granular interactions into consideration. The plastic deformation state of the finite element model was computed by means of CPFE analysis based on the {110}<111> slip system in body centered cubic (BCC) crystal. The experiment showed that the most of the grains rotated toward the preferred orientation <110> along the tensile axis and that intra-granular orientation spread and multi-directionally rotated as the tensile strain increased. These results are reproduced by the CPFE analysis, in which the influence of interaction between neighboring grains is taken into consideration.

1. Introduction

The understanding of non-linear and complicated mechanical behavior of polycrystalline metals is one of the important issues to predict plastic behavior of the materials. Mathur, et al. [1] predicted the evolution of the crystallographic texture for roll forming of FCC metals using Taylor homogenization method [2]. Iwakuma, et al. [3] characterized the kinematic hardening caused by the interaction between grains using Hill's self-consistent method [4]. Watanabe, et al. [5] computed the development of the macroscopic anisotropy caused by the cross-hardening behavior of a single crystal with two-scale finite element analysis based on the mathematical homogenization method [6]. Consequently, various homogenization approaches have been proposed and developed in this field. The experimental confirmation for these methods is however necessary to confirm the validity of above–mentioned constitutive models.

Recent synchrotron-based high energy x-ray diffraction technique has opened new ways for experimental evaluations for these models sophisticated over the past several decades. Three-dimensional x-ray diffraction (3DXRD) microscopy [7] has enabled non-destructive three-dimensional characterization of polycrystalline metals and alloys. Poulsen, et al. [8] and Winther, et al. [9] observed the lattice rotations of polycrystalline aluminum by 3DXRD and then compared with some classic homogenization models. Oddershede, et al. [10] observed the lattice rotations for a tensile deformed IF steel and also discussed from a view point of crystal plasticity. To the authors' knowledge, however, only Taylor model [11], Sachs model [12] and self-consistent model [13] has been compared with the 3DXRD observation, and no reports considering the influence of neighboring grains has found. Finite element method is possible to be directly taken the inter-granular relationship into consideration.

In the present study the plastic behavior of polycrystalline iron observed by a modified 3DXRD method [14] with the tensile test is analyzed by crystal plasticity finite element (CPFE) medhod as well as an analysis with Taylor type boundary condition. The measured microstructure by the 3DXRD method in the authors' other work [14] are used for the analyses. The elastic and plastic

anisotropy of body centered cubic (BCC) crystal is considered in the analyses. The lattice rotations in single grains by the tensile deformation obtained from the experiment and the analyses are compared.

2. Crystal plasticity finite element analysis

Constitutive equations for crystal plasticity In this study, the fully implicit stress-update algorithm for the proposed constitutive model is applied, which has been formulated by Huang [15]. A yield function for the α-th slip system is given as:

$$\varphi^{(\alpha)} := |\tau^{(\alpha)}| - q^{(\alpha)} \leq 0 \tag{1}$$

where $\tau^{(\alpha)}$ is the resolved shear stress and $q^{(\alpha)}$ is the critical resolved shear stress (CRSS) including the plastic hardening. In a single crystal plasticity, the resolved shear stress is defined as below in the current configuration with the slip system vectors ($\mathbf{s}^{(\alpha)}$, $\mathbf{m}^{(\alpha)}$):

$$\tau^{(\alpha)} := \mathbf{s}^{(\alpha)} \cdot (\boldsymbol{\tau}\mathbf{m}^{(\alpha)}) \qquad \forall \alpha \in \{1, \cdots, n_{slip}\} \tag{2}$$

where $\boldsymbol{\tau}$ is the Kirchhoff stress tensor defined in the current configuration, and $\mathbf{s}^{(\alpha)}$ and $\mathbf{m}^{(\alpha)}$ are the slip direction vector and the normal vector of the slip surface of α-th slip system, respectively. n_{slip} is the number of slip system. In this study, {011}<111> slip system for bcc is considered, the n_{slip} being 12, accordingly. The CRSS is described as follows:

$$q^{(\alpha)} := \tau_0 + \sum_{\alpha=1}^{n_{slip}} h_{\alpha\beta}\xi^{(\alpha)} \qquad \forall \alpha \in \{1, \cdots, n_{slip}\} \tag{3}$$

where τ_0 is the reference yield stress of α-th slip system, and $h_{\alpha\alpha}$ and $h_{\alpha\beta}$ ($\alpha \neq \beta$) are respectively the self and latent hardening moduli, $\xi^{(\alpha)}$ is the internal variable of plastic history of the α-th yield criterion, which denotes the accumulated slip of the α-th slip system in a single crystal plasticity. Pierce, et. al [16] and Asaro [17,18] defined the simple form for the self-hardening modulus as follows:

$$h_{\alpha\alpha} := h_0 \cosh^{-2}\left|\frac{h_0}{\tau_s - \tau_0}\sum_{\lambda=1}^{n_{slip}} \xi^{(\lambda)}\right| \qquad \forall \alpha \in \{1, \cdots, n_{slip}\} \tag{4}$$

where h_0 and τ_s are the initial hardening modulus and the break-through stress where large plastic flow initiates, respectively. The latent hardening modulus is described as follows:

$$h_{\alpha\beta} := a h_{\alpha\alpha} \qquad \forall \alpha \in \{1, \cdots, n_{slip}\} \tag{5}$$

where a is also the constants. The other details about the constitutive equations are described elsewhere [15].

Determination of material constants Here we obtain the material constants to reproduce macroscopic stress-strain relationship for the experimental tests, by means of a polycrystalline metal modeled within the homogenization method based on finite element analysis [6]. At the micro-scale, the finite element model of Fig. 1 is used as a representative volume element (RVE) of polycrystalline aggregate. The RVE comprises 54 crystal grains and is assumed to satisfy the geometrical periodicity condition. The crystal grain has an idealized geometry of the truncated octahedron and is discretized by 80 standard isoparametric hexahedron finite elements. The crystallographic orientations of each grain are provided in a random fashion. The macroscopic uniaxial tensile deformation is imposed to the macroscopic single element in the corresponding Y_1 direction illustrated in Fig. 1. Elastic stiffness is quoted from the literature [19]. Consequently, the macroscopic stress–strain curve is calculated in Fig. 2 by adopting the material constants presented in Table 1, which gives good accordance with the experimental response. Other ten sets of random

Table 1. Material constants

Elastic stiffness [19]	C_{11}	[GPa]	228.09
	C_{12}	[GPa]	133.48
	C_{44}	[GPa]	110.86
Initial hardening modulus	h_0	[GPa]	0.200
Breakthrough stress	τ_s	[GPa]	0.090
Reference yield stress	τ_0	[GPa]	0.041
coefficient between self and latent hardening moduli	a	[-]	1.000

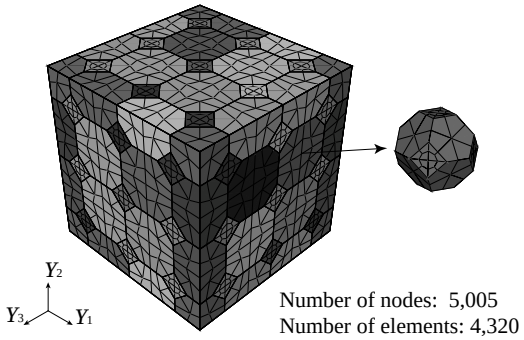

Fig. 1. Finite element model of polycrystalline aggregate for determining the material constants for the polycrystalline iron. The polycrystalline aggregate comprises 54 grains with the idealized geometry of the truncated octahedron. The gray values represent the difference of the crystallographic orientations given in a random fashion.

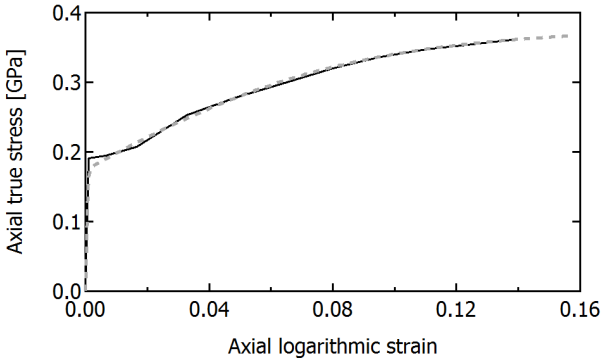

Fig. 2. Macroscopic stress-strain curves of polycrystalline iron. The solid and the dashed lines indicate experimental and numerical results, respectively.

Crystal plasticity analysis corresponding to three-dimensional x-ray diffraction observation

Here we assess the texture change of a polycrystalline iron tensile test by performing the crystal plasticity analysis with finite element model corresponding to the experimentally obtained orientation map, as seen in Fig. 3 [9], in which there are large 7 grains. Fig. 4 shows the model composed with 3423 voxels and each voxel is discretized by 3 standard isoparametric hexahedron finite elements, which is created from the shape of Fig. 3(a). The crystallographic orientations of each element are provided from the orientation map before tensile deformation. The macroscopic uniaxial tensile deformation is imposed toward the z direction illustrated in Fig. 4. In this case, elastic and plastic anisotropy and inter-granular interaction are considered.

The other crystal plasticity analysis with Taylor type boundary condition is also performed, in which homogeneous strain distribution is applied on the whole FE model, and then the stress-strain interaction between neighboring grains are not considered. The material constants are also adopted from Table 1.

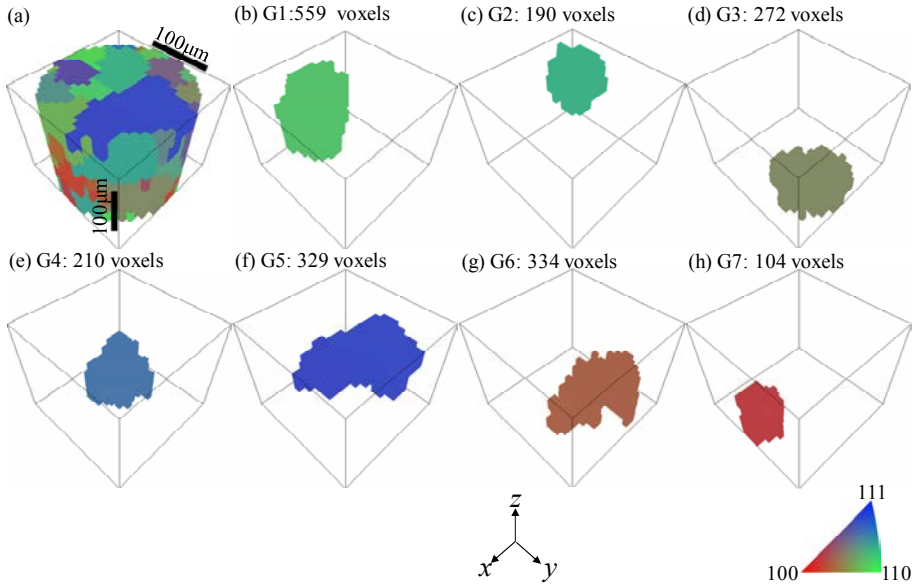

Fig. 3. Three-dimensional orientation map before tensile test. (b) – (h) show major seven large grains (G1–G7) extracted from (a). The mapped volume and the voxel size are φ 200 μm × z 175 μm and x 6.7 μm × y 6.7 μm × z 25 μm, respectively. The mapped volume has 3423 voxels. The colors show the inverse pole figure of the tensile axis in the stereographic triangle.

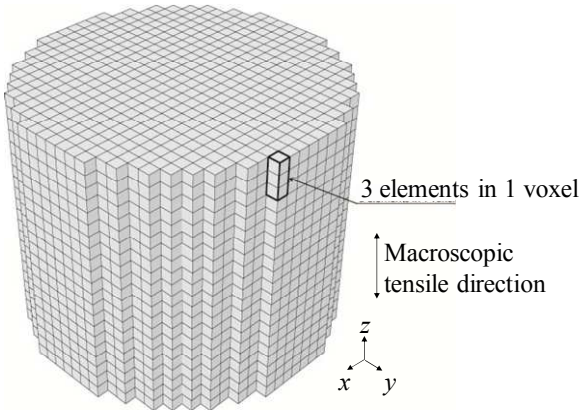

Fig. 4. Finite element model of the polycrystalline iron corresponding to the three-dimensional orientation map as seen in Fig. 3(a). The model also consists of 3423 voxels and each voxel comprises 3 elements (therefore the model has 10269 elements).

3. Results and discussion

Fig. 5 shows the inverse pole figures of the tensile axis in the stereographic triangle for the large grains G1–G7 (a) from the 3DXRD observation, (b) from the analysis with Taylor type boundary condition, and (c) from CPFE analysis. In the observation, all of the grains mainly rotate toward <110> along the tensile axis, which is attributed to the slip system of BCC. Also in the both analyses, most of the grains rotate toward <110> direction, which is in accordance with the observation. The grain G4 however does not rotate toward <110> in the analyses, the reason of which is unclear at present.

The observed orientation spreads are not found in the analysis with Taylor-type boundary condition, since the interaction between neighboring grains, which gives rise to the intra-granular inhomogeneous deformation, is not considered. On the other hand the spreads are found in the CPFE analysis. For example the grain G6 rotates and spreads toward <110>–<111> side as well as <110> corner in the analysis, which is in good accordance with the observation. The reasons of the remaining difference are thought to be due to spacial resolution by the 3DXRD measurement and not to considering {112}<111> and {123}<111> slip systems [20], which are considered in authors' future work. Fig. 6 depicts the population of the rotation angles from the initial orientation in the grain G6. It is found from the figure that the mean rotation angles and the dispersion increase as the tensile strain increases.

These results show that the consideration of inter-granular relationship plays a role to spread intra-granular orientations. It is also found that the CPFE analysis qualitatively reproduces the orientation changes observed by the 3DXRD method.

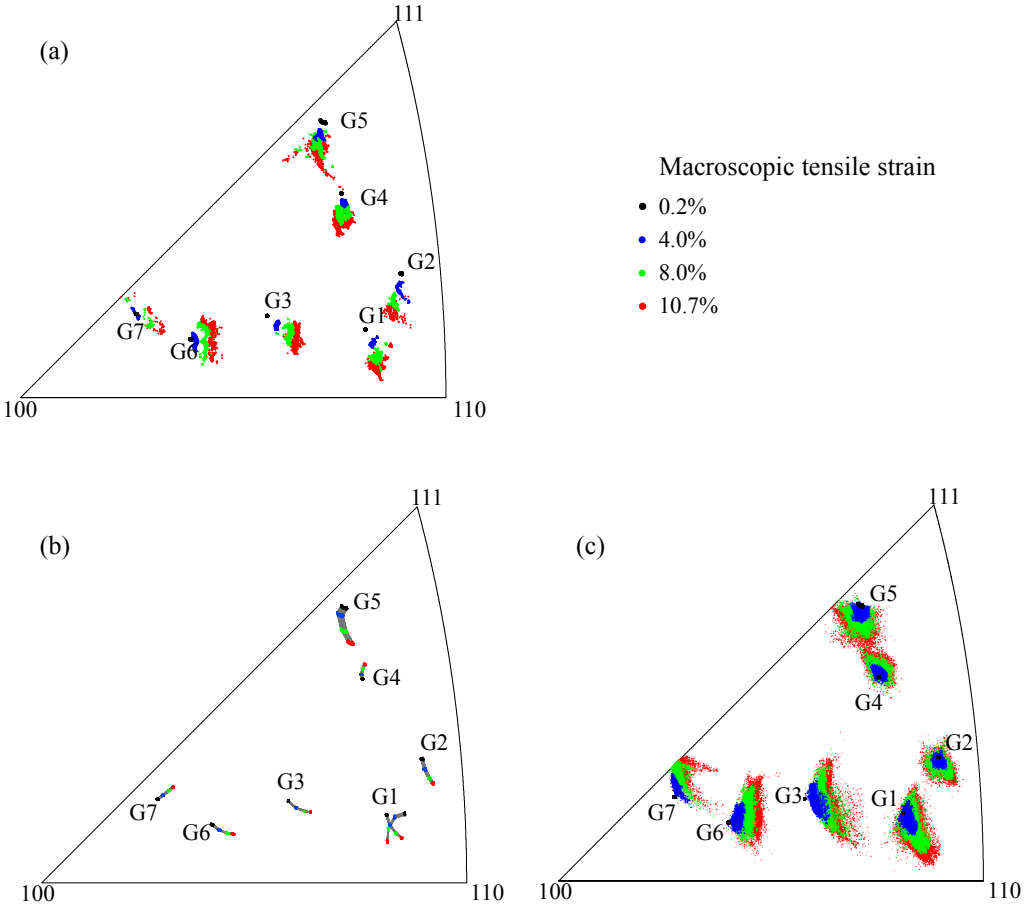

Fig. 5. Inverse pole figures of the tensile axis in the stereographic triangle for the grains G1–G7, (a) from the experimental tensile test coupled with the 3DXRD observation, (b) from the crystal plasticity analysis with Taylor type boundary condition, and (c) from CPFE analysis taking the interaction with neighboring grains into consideration. The all voxels in the observation or all integration points in the finite element analysis assigned to the grains are plotted for the all tensile strains.

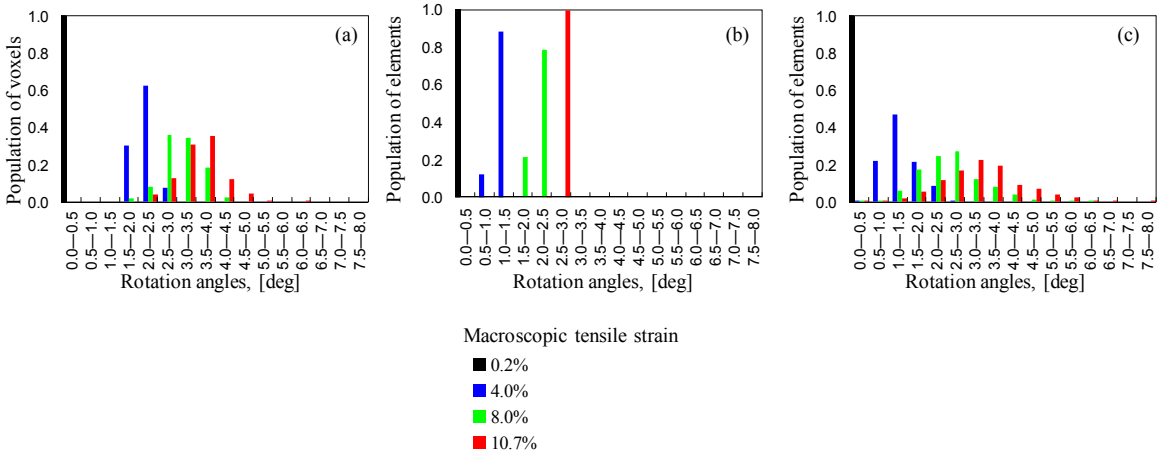

Fig. 6. Populations of rotation angles from the initial orientation in the grain G6. (a) experimental tensile test coupled with the 3DXRD observation, (b) crystal plasticity analysis with Taylor type boundary condition, and (c) CPFE analysis.

4. Summary

Plastic behavior for polycrystalline iron examined by a modified 3DXRD method was analyzed by CPFE analysis. A crystal plasticity analysis with Taylor-type boundary condition was also performed. In the crystal plasticity analyses, the constitutive equation formulated by Huang [13] and the {110}<111> slip system of BCC were adopted. The FE model for the microstructure of the tensile test specimen was directly modeled from the measurements by the 3DXRD method. The observed orientation change by tensile deformation toward the preferred orientation <110> along the tensile axis was reproduced by the both analyses. The orientation spread and multidirectional rotations in grains were meanwhile reproduced only by the CPFE analysis, in which the influence of interaction between neighboring grains was taken into consideration.

References

[1] K. K. Mathur and P. R. Dawson, Int. J. Plast. 5(1989) 67–94.

[2] G. I. Taylor, J. Inst. Met. 62(1938), 307–324.

[3] T. Iwakuma and S. Nemat-Nasser, Proc. R. Soc. Lond. A 394(1983), 87–119.

[4] R. Hill, J. Mech. Phys. Solids 13(1965), 89–101.

[5] I. Watanabe, K. Terada and M. Akiyama, Comput. Mater. Sci. 32(2005), 240–250.

[6] K. Terada, I. Saiki, K. Matsui and Y. Yamakawa, Comput. Meth. Appl. Mech. Eng. 192(2003), 3531–3563.

[7] H. F. Poulsen, J. Appl. Cryst. 45 (2012) 1084–1097.

[8] H. F. Poulsen, L. Margulies, S. Schmidt and G. Winther, Acta Mater., 51(2003) 3821–3830.

[9] G. Winther, L. Margulies, S. Schmidt and H. F. Poulsen, Acta Mater., 52(2004) 2863–2872.

[10] J. Oddershede, J. P. Wright, L. Margulies, X. Huang, H. F. Poulsen, S. Schmidt, G. Winther, Proceedings of the 31st Risø International Symposium on Material Science (2010) 369–374.

[11] G. I. Taylor, J. Inst. Metals, 62 (1938) 307–324.

[12] G. Z. Sachs, Verein. Deut. Mag., 72 (1928) 734–736.

[13] H. W. Hutchinson, Proc. R. Soc. London A, 319 (1970) 247–272.

[14] Y. Hayashi, Y. Hirose and D. Setoyama: submitted to Mater. Sci. Forum (2013).

[15] Y. Huang, Mech Report, Vol.178, Division of Engineering and Applied Sciences, Harvard University, Cambridge, Massachusetts (1991).

[16] D. Peirce, R. J. Asaro and A. Needleman, Acta Metall., 30(1982) 1087–1119.

[17] R. J. Asaro, J. Appl. Mech, 50(1983) 921–934.

[18] R. J. Asaro, Advances in Appl. Mech., 23(1983) 1–115.

[19] G. Simmons, H. Wang, MIT Press, Cambridge, Massachusetts, and London, England, (1971).

[20] C. J. Hamelin, B. J. Diak and A. K. Pilkey, Int. J. Plast. 27(2011) 1185–1202.

Mechanical Stress Evaluation by Neutrons and Synchrotron Radiation VII
10.4028/www.scientific.net/MSF.777

Crystal Plasticity Finite Element Analysis Based on Crystal Orientation Mapping with Three-Dimensional X-Ray Diffraction Microscopy
10.4028/www.scientific.net/MSF.777.142

豊田ビームライン研究発表会プロシーディングス 5, (2014)
ECS Electrochemistry Letters, **3** (6) A66-A68 (2014)
2162-8726/2014/3(6)/A66/3/$31.00 © The Electrochemical Society

X-Ray Absorption and Diffraction Studies of $LiNiO_2$-Derivatives with or without Electrolyte at Elevated Temperature

Yoshinari Makimura,[*,z] Chikaaki Okuda, Takamasa Nonaka, Yusaku F. Nishimura, Tsuyoshi Sasaki,[*] and Yoji Takeuchi

Toyota Central Research and Development Laboratories, Incorporated, Nagakute, Aichi 480-1192, Japan

Simultaneous measurement of X-ray absorption and diffraction at elevated temperature was developed and carried out to examine thermal decomposition of $LiNi_{0.75}Co_{0.15}Al_{0.05}Mg_{0.05}O_2$ (NCA-Mg) electrode charged at 4.2 V vs. Li^+/Li with or without electrolyte. Our measurement clearly displays accelerated reduction of NCA-Mg by the electrolyte in terms of the change in crystal structure and the oxidation states of nickel and cobalt species. Reduction of nickel and cobalt species by XANES occurs at about 50°C lower temperature than the structural collapse detected by XRD, which will be a key to understand the mechanisms for onset temperature of the exothermic reactions.
 [DOI: 10.1149/2.014406eel]

Manuscript submitted February 10, 2014; revised manuscript received March 31, 2014. Published April 23, 2014.

Lithium-ion batteries have to be operated in the limited conditions in terms of temperature, voltage and current to achieve long cycling-life and to overcome safety-concerns. We reported that capacity fading and resistance increase of the lithium-ion battery of $LiNi_{0.8}Co_{0.15}Al_{0.05}O_2$ with graphite occurring upon cycling especially above 60°C are derived from the localized degradation of $LiNi_{0.8}Co_{0.15}Al_{0.05}O_2$,[1,2] and hence the cycling life can be improved by Mg-substitution, i.e., $LiNi_{0.75}Co_{0.15}Al_{0.05}Mg_{0.05}O_2$ (NCA-Mg).[3] Toward large-sized power supply for automotive and stationary applications, understanding and improving the safety of lithium-ion batteries are another significant challenge.[4,5] Although thermal-runaway mechanism of lithium-ion batteries is complicated, the exothermic reaction of positive electrode with electrolyte is a critical contribution to the battery-safety.[6–10] Exothermic reactions have been proposed to be associated with the solvent-combustion ascribed to structural collapse of electrode materials with respect to the heats generated at elevated temperatures,[6,7,10] while the mechanisms of onset temperature at which the exothermic reactions occur are still unclear.

Synchrotron technique gives us significant in-situ information on (electro-)chemical reactions in the batteries with respect to X-ray absorption fine structure (XAFS) and X-ray diffraction (XRD).[9,11–13] Independent in-situ or ex-situ techniques have been combined to detect the structural change of materials, while simultaneous in-situ XAFS and XRD measurement is necessary to follow precisely the exothermic reaction occurring at elevated temperature. In this paper, we propose our new technique to examine thermal decomposition of NCA-Mg in the absence or coexistence of electrolyte at elevated temperature. Our measurement shows the proper-order of reaction-steps at elevated temperature, and also describes a role of electrolyte on exothermic reaction.

Experimental

500 mAh-class cylindrical lithium-ion cells of NCA-Mg with graphite were fabricated, in which the positive electrode consisting of 85 wt% NCA-Mg, 10 wt% carbonblack, and 5 wt% polyvinylidene fluoride (PVdF) binder was coated about 20 μm thick on both sides of aluminum foil, and the negative electrode of 95 wt% graphite and 5 wt% PVdF binder was coated on both sides of copper foil. The cell body of wound sheets of positive and negative electrodes separated by polypropylene membrane was immersed in 1 M $LiPF_6$ ethylene carbonate (EC) / dimethyl carbonate (DMC) / ethyl methyl carbonate (EMC) (3 / 4 / 3, v/v) electrolyte. Then fabricated cells were charged to 4.1 V, namely 4.2 V vs. Li^+/Li for the positive electrode, and the electrode was taken out of the cells in an Ar-filled glove box, washed by DMC solution and dried under Ar atmosphere. Thus prepared NCA-Mg electrodes were used for the measurement.

Simultaneous XAFS and XRD measurements were performed at a beam line BL33XU in SPring-8,[14] and the beam energy of 8.0 keV was used for in-situ XRD. Beam size at the sample position was 0.5 × 1.2 mm. The intensities of the incident and transmitted X-rays were measured by ionization chambers at room temperature. Detailed procedures for the measurement are described in a separate paper,[15] and other conditions are given in the later section.

Results and Discussion

Figure 1 displays the newly developed technique to achieve simultaneous measurement of XAFS and XRD at elevated temperature as high as 450°C. The electrode sheet with or without electrolyte was sealed in Kapton sheet and was placed in the setup. Temperature for the setup was controlled and monitored by heat guns with thermometer, and XAFS and XRD were simultaneously collected from room temperature to 450°C for every 50°C. Kapton sheet was stable enough to protect the electrode sheet even at 450°C. Figure 2a displays XRD patterns for NCA-Mg electrode without electrolyte. At room temperature, the XRD pattern for the charged NCA-Mg is typical of α-$NaFeO_2$-type layered structure with R3(over-bar)m space group, and miller indexes in hexagonal setting are shown in this figure. Until 250°C, diffraction peaks slightly shift to lower angle because of thermal expansion, while the sample has layered structure. XRD pattern for the sample suddenly changes at 300°C, and then peak-broadening and the change in diffraction angle are more obvious above 300°C. During heating above 300°C, diffraction peaks of (102) and (104) in hexagonal setting increase whereas those of (003) and (101) decrease, suggesting structural change from layered to spinel-related structure owing to structural collapse at elevated temperature. Miller indexes based on a cubic lattice is also given in this figure. Similar trend was also reported by Bang et al. with respect to the temperature at which structural change occurs.[10]

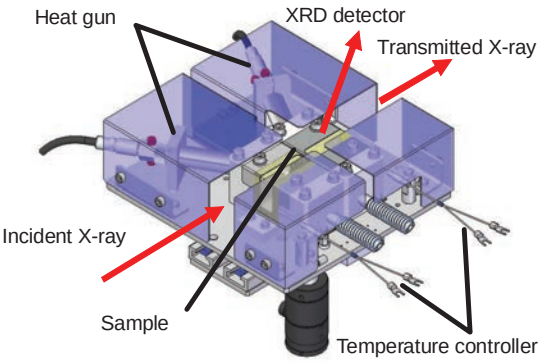

Figure 1. (Color online) Schematic illustration of the setup to control sample-temperature for X-ray absorption and diffraction measurements.

*Electrochemical Society Active Member.
zE-mail: ymakimura@mosk.tytlabs.co.jp

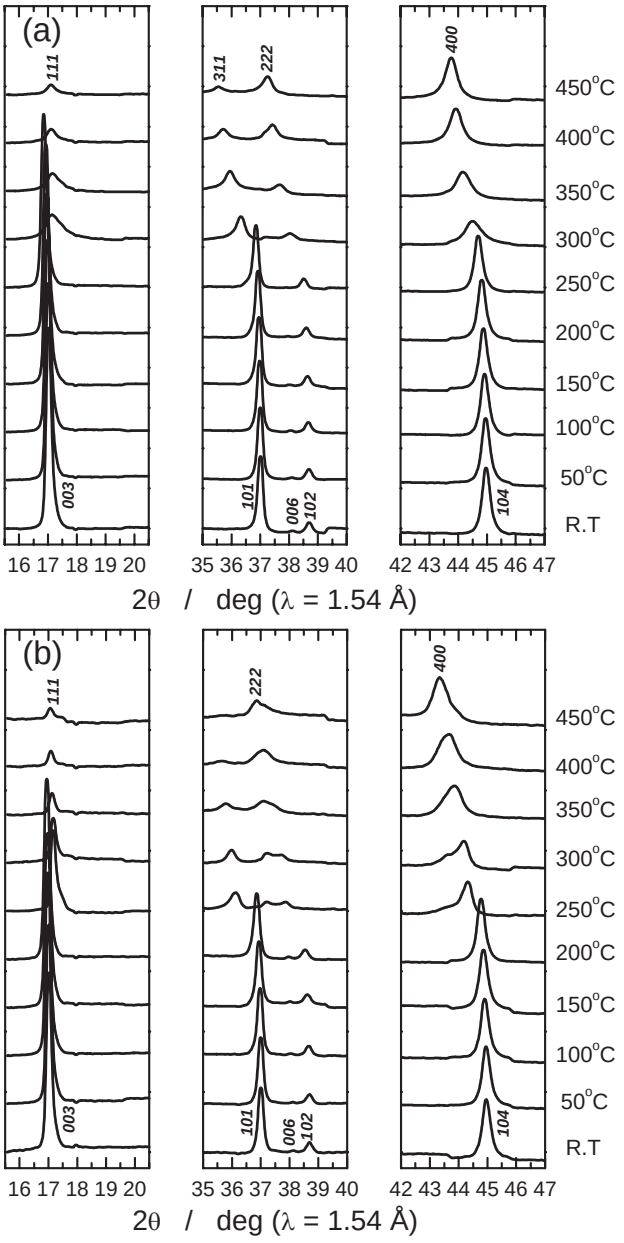

Figure 2. XRD patterns for $LiNi_{0.75}Co_{0.15}Al_{0.05}Mg_{0.05}O_2$ in a charged state at 4.2 V vs. Li^+/Li in the (a) absence or (b) coexistence of electrolyte during heating every 50°C from room temperature to 450°C, which were collected at an energy of 8.0 keV.

Figure 2b shows XRD patterns for NCA-Mg with electrolyte to clarify a role of electrolyte on the thermal decomposition. Small peaks appear at 250°C in the vicinity of diffraction peaks of (003) and (104) in hexagonal setting, while major peaks are associated with layered structure. Those new peaks increase during heating above 250°C, indicating two-phase coexistence of layered and spinel-related structures for the structural change with electrolyte, which is derived from accelerated reduction of NCA-Mg by the electrolyte.

Ni K-edge X-ray absorption near-edge structure (XANES) spectra for NCA-Mg electrode in the absence or coexistence of electrolyte are shown in Fig. 3a and 3b, and monotonous edge-shift is seen during heating. Edge energies at half-step height, i.e., normalized absorbance of 0.5, are displayed in Fig. 3c, which is often used to estimate the oxidation state of nickel species.[16] Edge energy of nickel metal is assumed to be 0 eV for comparison, and that of NiO is also shown as a reference. Oxidation states of nickel species at 450°C are almost

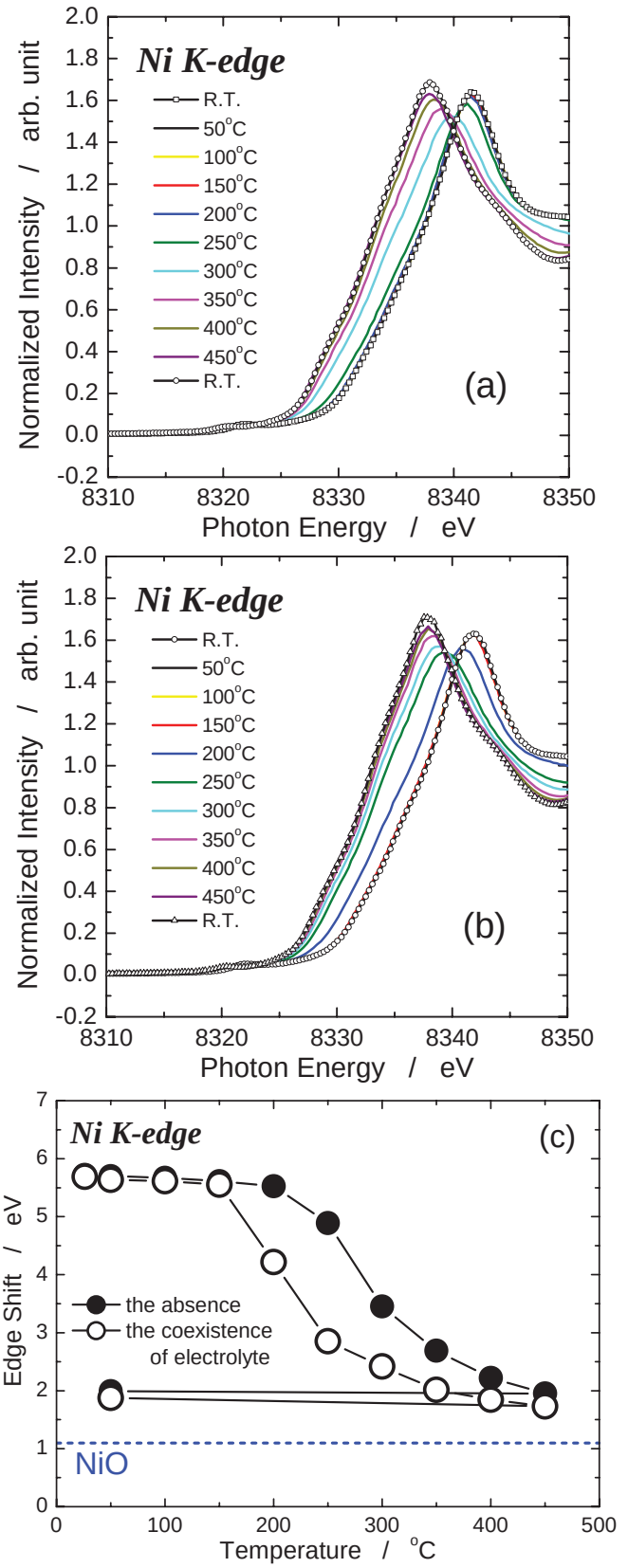

Figure 3. (Color online) Ni K-edge XANES spectra of $LiNi_{0.75}Co_{0.15}Al_{0.05}Mg_{0.05}O_2$ in a charged state at 4.2 V vs. Li^+/Li in the (a) absence or (b) coexistence of electrolyte during heating every 50°C from room temperature to 450°C, and (c) edge energies at half-step heights as a function of heating temperature. Edge energy of nickel metal is assumed to be 0 eV for comparison, and that of NiO is also shown as a reference.

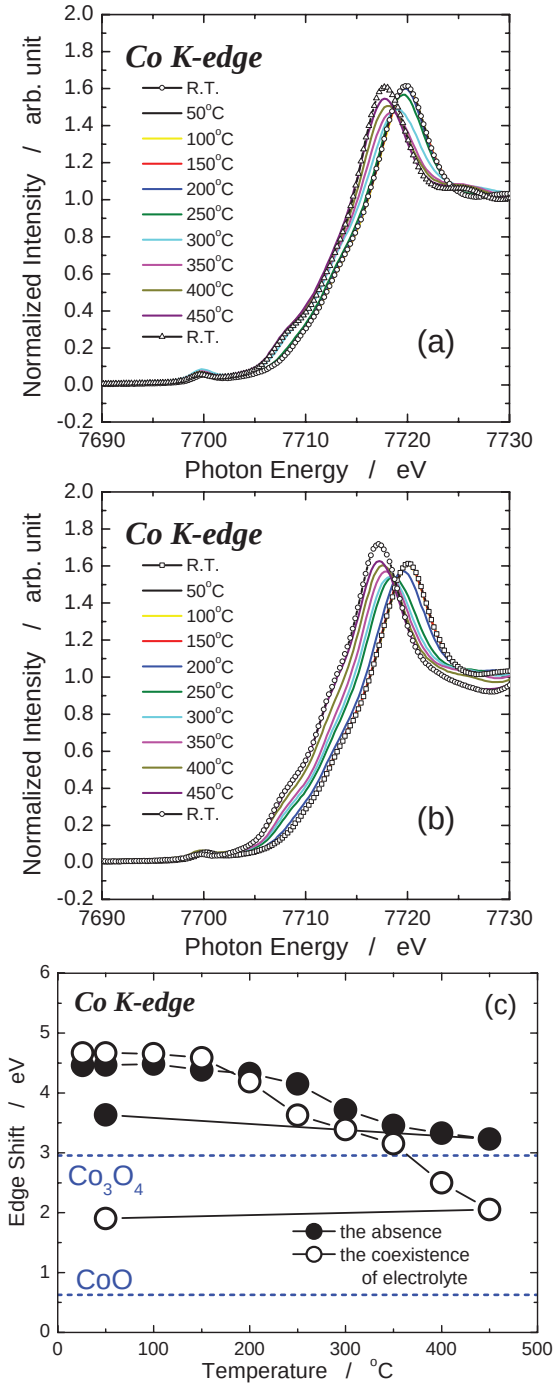

Figure 4. (Color online) Co K-edge XANES spectra of $LiNi_{0.75}Co_{0.15}Al_{0.05}Mg_{0.05}O_2$ in a charged state at 4.2 V vs. Li^+/Li in the (a) absence or (b) coexistence of electrolyte during heating every 50°C from room temperature to 450°C, and (c) edge energies at half-step heights as a function of heating temperature. Edge energy of cobalt metal is assumed to be 0 eV for comparison, and those of Co_3O_4 and CoO are also shown as references.

the same between two samples, which is close to NiO. About 50°C difference in the temperature at which the reduction of NCA-Mg starts between the electrolyte presence and absence, i.e., 200°C and 250°C, respectively, indicating reduction of NCA-Mg is accelerated by the electrolyte.

Co K-edge XANES spectra for NCA-Mg are shown in Fig. 4a and 4b. In the absence of electrolyte, edge shift to lower energy occurs in 250–300°C and then the change in spectral shape, characteristic of Co K-edge spectra,[17] is seen above 300°C, while coexistence of NCA-Mg with electrolyte gives monotonous edge-shift to lower energy in the entire temperature range. Edge energies of Co K-edge spectra at half-step height are displayed in Fig. 4c assuming that of cobalt metal as 0 eV for comparison. The edge-shift temperature is the same between Ni and Co K-edge spectra. Edge energies of Co_3O_4 and CoO are also shown as references. Edge energy for Co K-edge of NCA-Mg without electrolyte at 450°C is close to that of Co_3O_4, whereas reduction of cobalt species in the coexistence of electrolyte proceeds more deeply toward CoO above 350°C, which was also reported by MacNeil and Dahn with respect to thermal decomposition of $Li_{0.5}CoO_2$.[6]

Irrespective of electrolyte presence, reduction of nickel and cobalt species in NCA-Mg by XANES is found to occur at lower temperature of at least 50°C than the XRD structural-change, which will be a key to understand the exothermic mechanisms, especially onset temperature, occurring between electrode materials and nonaqueous electrolyte.

Conclusion

Simultaneous XAFS and XRD measurement at elevated temperature was newly developed to examine thermal decomposition of NCA-Mg with or without electrolyte. Reduction of NCA-Mg with electrolyte occurs at about 50°C lower temperature than that without electrolyte. Oxidation states of nickel species at 450°C are close to that of NiO irrespective of electrolyte presence, and that of cobalt species without electrolyte are associated with Co_3O_4. Reduction of cobalt species is promoted by the electrolyte more deeply toward CoO. Oxidation states of nickel and cobalt species detected by XANES start to decrease at about 50°C lower temperature than the structural change by XRD, and hence the onset temperature of the exothermic reaction examined by differential scanning calorimetry (DSC) can be compared with the simultaneous XAFS and XRD measurement to understand which reaction-step is a key for exothermic reactions of electrode materials with electrolyte. Such an approach is in progress in our group.

Acknowledgments

The synchrotron radiation experiments were performed at the BL33XU of SPring-8 with the approval of the Japan Synchrotron Radiation Research Institute (JASRI) (Proposal No. 2012A7008 and 2012B7008).

References

1. T. Sasaki, T. Nonaka, H. Oka, C. Okuda, Y. Itou, Y. Kondo, Y. Takeuchi, Y. Ukyo, K. Tatsumi, and S. Muto, *J. Electrochem. Soc.*, **156**, A289 (2009).
2. S. Muto, Y. Sasano, K. Tatsumi, T. Sasaki, K. Horibuchi, Y. Takeuchi, and Y. Ukyo, *J. Electrochem. Soc.*, **156**, A371 (2009).
3. H. Kondo, Y. Takeuchi, T. Sasaki, S. Kawauchi, Y. Itou, O. Hiruta, C. Okuda, M. Yonemura, T. Kamiyama, and Y. Ukyo, *J. Power Sources*, **174**, 1131 (2007).
4. H. Maleki, G. Deng, A. Anani, and J. Howard, *J. Electrochem. Soc.*, **146**, 3224 (1999).
5. D. D. MacNeil, L. Christensen, J. Landucci, J. M. Paulsen, and J. R. Dahn, *J. Electrochem. Soc.*, **147**, 970 (2000).
6. D. D. MacNeil and J. R. Dahn, *J. Electrochem. Soc.*, **148**, A1205 (2001).
7. D. D. MacNeil and J. R. Dahn, *J. Electrochem. Soc.*, **149**, A912 (2002).
8. M. Guilmard, L. Croguennec, and C. Delmas, *Chem. Mater.*, **15**, 4484 (2003).
9. W.-S. Yoon, M. Balasubramanian, X.-Q. Yang, J. McBreen, and J. Hanson, *Electrochem. Solid-State Lett.*, **8**, A83 (2005).
10. H.- J. Bang, H. Joachin, H. Yang, K. Amine, and J. Prakash, *J. Electrochem. Soc.*, **153**, A731 (2006).
11. A. N. Mansour, X.-Q. Yang, X. Sun, J. McBreen, L. Croguennec, and C. Delmas, *J. Electrochem. Soc.*, **147**, 2104 (2000).
12. T. Nonaka, C. Okuda, Y. Seno, H. Nakano, K. Koumoto, and Y. Ukyo, *J. Power Sources*, **162**, 1329 (2006).
13. K.-W. Nam, S.-M. Bak, E. Hu, X. Yu, Y. Zhou, X. Wang, L. Wu, Y. Zhu, K.-Y. Chung, and X.-Q. Yang, *Adv. Funct. Mater.*, **23**, 1047 (2013).
14. T. Nonaka, K. Dohmae, T. Araki, Y. Hayashi, Y. Hirose, T. Uruga, H. Yamazaki, T. Mochizuki, H. Tanida, and S. Goto, *Rev. Sci. Instrum.*, **83**, 083112 (2012).
15. T. Nonaka, C. Okuda, H. Oka, Y. F. Nishimura, Y. Makimura, Y. Kondo, K. Dohmae, and Y. Takeuchi, submitted to *J. Synchrotron Radiat.*
16. A. N. Mansour and C. A. Melendres, *J. Phys. Chem. A*, **102**, 65 (1998).
17. I. Nakai and T. Nakagome, *Electrochem. Solid-State Lett.*, **1**, 259 (1998).

ACS APPLIED MATERIALS & INTERFACES

Letter

www.acsami.org

Structural Improvement of $CaFe_2O_4$ by Metal Doping toward Enhanced Cathodic Photocurrent

Keita Sekizawa,[†,‡] Takamasa Nonaka,[†] Takeo Arai,[†,‡] and Takeshi Morikawa*[,†,‡]

[†]Toyota Central Research & Development Laboratories, Inc., 41-1, Yokomichi, Nagakute, Aichi 480-1192, Japan

[‡]Advanced Catalytic Transformation Program for Carbon Utilization (ACT-C), Japan Science and Technology Agency, 4-1-8 Honcho, Kawaguchi, Saitama 332-0012, Japan

Supporting Information

ABSTRACT: Various metal-doped *p*-type $CaFe_2O_4$ photocathodes were prepared in an attempt to improve the low quantum efficiency for photoreaction. CuO and Au doping enhanced the photocurrent by expansion of the absorption wavelength region and plasmon resonance, respectively. X-ray diffraction (XRD) and X-ray absorption fine structure (XAFS) analysis showed that doping with these metals further disturbed the originally distorted crystal structure of $CaFe_2O_4$. In contrast, doping with Ag relaxed the distorted crystal structure around the Fe center toward symmetry. Ag doping resulted in improvement of the carrier mobility together with a red-shift of photoabsorption with Ag-doped $CaFe_2O_4$ having a 23-fold higher photocurrent than undoped $CaFe_2O_4$.

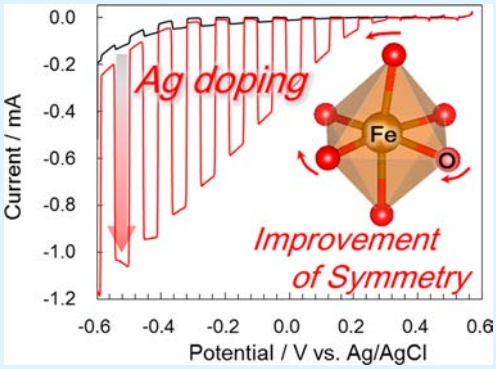

KEYWORDS: *earth-abundant materials, p-type semiconductor, X-ray absorption fine structure, ferrite compound, thin film*

Photocatalytic reactions are widely used for solar energy conversion[1] and environmental purification,[2] and they require semiconductors which show efficient photoresponses owing to their narrow bandgaps, high carrier densities, and mobility. To realize efficient photocatalytic systems, reports on combinations of *p*-type and *n*-type semiconductors for photoelectrochemical devices[3−6] and photocatalysts[7−9] have been increasing. Although there have been many reports on highly efficient *n*-type semiconductors, there have been comparatively few studies on *p*-type semiconductors, most of which consist of rare metals. Hence development of efficient *p*-type semiconductors is crucial. Calcium iron oxide ($CaFe_2O_4$) is an attractive *p*-type semiconductor which consists of only abundant elements. $CaFe_2O_4$ exhibits visible-light response (bandgap = 1.9 eV) and a suitable conduction band edge (−0.6 V vs RHE)[10] for application to water splitting,[11,12] photodecomposition of harmful organics,[13] and superhydrophilic reactions.[14] However, the quantum efficiency of the $CaFe_2O_4$ electrode is relatively low, which is mainly due to its poor mobility (ca. 10^{-1} V^{-1} s^{-1} cm^2).[15]

Metal doping into metal oxide has often been attempted to induce a red-shift of the bandgap transition[1] and generate acceptor levels in the bandgap due to enhanced *p*-type character.[16] Furthermore, if the atomic orbitals of the dopant are hybridized with the narrow d band in the conduction band (CB) or valence band (VB), bandgap modulation and an enhancement of carrier mobility are expected.

Here, to explore a suitable dopant, we have prepared various metal-doped $CaFe_2O_4$ (M-$CaFe_2O_4$; M = Ag, Au, CuO, Pd, and Ir) electrodes by radio frequency (RF) magnetron cosputtering followed by postannealing at a low temperature. It was confirmed that some metals enhance the photoelectrochemical properties of $CaFe_2O_4$. The enhancement effects of the cationic dopants were investigated in detail by structural analyses.

$CaFe_2O_4$ and a metal were codeposited by RF magnetron sputtering onto glass substrates coated with antimony-doped tin oxide (ATO), a transparent conductive oxide. The compositions of the films were adjusted by changing the input RF powers for the metal target in the range of 0−300 W, while that for $CaFe_2O_4$ was fixed at 500 W. The film thickness was adjusted to ca. 180 nm according to the sputtering time. The deposited electrodes were postannealed at an optimum temperature of 923 K in an O_2 gas flow for 2 h. The surface of the films was confirmed to be flat as shown by the scanning electron microscopy (SEM) image (Figure S1, Supporting Information). Representative scanning transmission electron microscopy (STEM) images (Figure S2e, Supporting Information) revealed that metals were aggregated in the films after annealing, while there were no aggregates before annealing (Figure S2d, Supporting Information). It indicates that an excess amount of metals for doping in lattices of $CaFe_2O_4$ aggregated during the annealing process.

Current−potential curves of the sputter-deposited films were measured in an electrochemical cell containing O_2-saturated 0.2

Received: April 24, 2014
Accepted: July 1, 2014
Published: July 1, 2014

M K_2SO_4 aqueous solution equipped with Pt wire and Ag/AgCl electrodes. In all of M-$CaFe_2O_4$'s, only Ag-$CaFe_2O_4$ showed dark current, which is a redox wave of Ag/Ag^+ by the elution of aggregated Ag. After oxidation by chronoamperometry at 0.6 V vs Ag/AgCl, the current disappeared, as shown in Figure S3 (Supporting Information). After this treatment, the color of the film changed from dark brown to yellow (Figure S3, Supporting Information), and voids due to the elution of Ag were evident by STEM analysis (Figure S2f, Supporting Information). Energy-dispersive X-ray (EDX) spectroscopy measurements indicated the residual amount of Ag was less than the detectable limit (<0.5 atom %). After repeated washing of the electrodes with distilled water, photocurrent−voltage curves were measured with fresh electrolyte.

Figure 1 shows current−potential curves for the Ag, CuO, Au, and undoped $CaFe_2O_4$ electrodes under chopped light

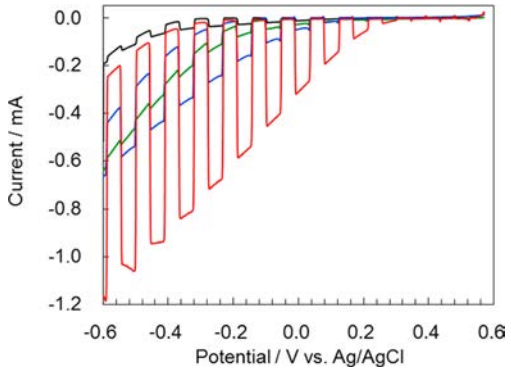

Figure 1. Current−potential curves measured in O_2-saturated 0.2 M K_2SO_4 solution under chopped light irradiation (300−800 nm) for Ag (35 W)-$CaFe_2O_4$ (red line), CuO (300 W)-$CaFe_2O_4$ (blue line), Au (50 W)-$CaFe_2O_4$ (green line), and $CaFe_2O_4$ (black line) electrodes. All electrodes were postannealed at 927 K, and the film thickness was fixed at ca.180 nm.

irradiation. These films exhibit typical cathodic photocurrents that correspond to O_2 reduction, which indicates that M-$CaFe_2O_4$'s are also *p*-type semiconductors. Ag (35 W)-$CaFe_2O_4$ (red line) showed the highest photoactivity. The photocurrent at 0.0 V vs Ag/AgCl was 23 times higher than that for $CaFe_2O_4$ (black line). Other Ag-$CaFe_2O_4$'s prepared by RF sputtering of a silver target in the range of 20−60 W also showed a higher photocurrent than $CaFe_2O_4$ (Figure S4a, Supporting Information). CuO-$CaFe_2O_4$ deposited by cosputtering with a RF power of 50−300 W for CuO also exhibited 1.3−2.9 times higher photocurrent than that of $CaFe_2O_4$ at 0 V (Figure S4b, Supporting Information). The photocurrent for Au (50 W)-$CaFe_2O_4$ was 1.7 times higher than that of $CaFe_2O_4$, although those for the Au electrodes sputtered at 15−37 W were lower (Figure S4c, Supporting Information). In contrast, doping with Pd and Ir did not enhance the photocurrent of $CaFe_2O_4$ (Figures S4d, e, Supporting Information). Time courses for the photocurrents with a bias of 0 V are shown in Figure S5 (Supporting Information). Although the photocurrents for CuO-$CaFe_2O_4$ and Au-$CaFe_2O_4$ decreased, that of Ag-$CaFe_2O_4$ was stable.

Figure 2 shows UV−vis absorption and incident photon to current efficiency (IPCE) spectra for $CaFe_2O_4$ doped with Ag, CuO, and Au and undoped $CaFe_2O_4$ films. The absorption edge of $CaFe_2O_4$ (ca. 650 nm, black line) was shifted to the longer-wavelength region by doping with Ag and CuO (red and

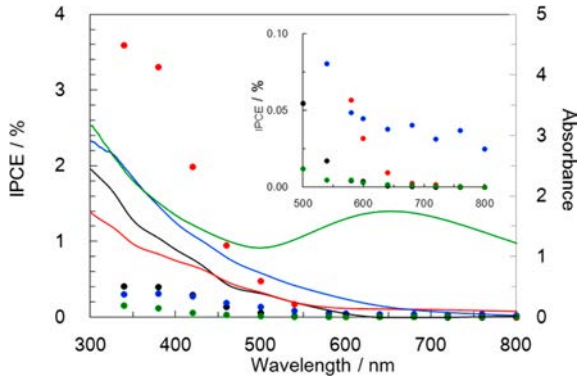

Figure 2. IPCE spectra (data points; left axis) and UV−vis absorption spectrum (lines; right axis) for Ag (35 W)-$CaFe_2O_4$ (red), CuO (300 W)-$CaFe_2O_4$ (blue), Au (50 W)-$CaFe_2O_4$ (green), and $CaFe_2O_4$ (black) electrodes. IPCEs were measured at 0.0 V vs Ag/AgCl with monochromatic light irradiation. The film thicknesses of all electrodes were fixed at ca.180 nm.

blue lines, respectively). The Au-$CaFe_2O_4$ film showed not only a red-shift but also an absorption peak around 500−800 nm (green line) which is attributed to the plasmonic absorption of Au nanoparticles.

The IPCE spectra also shifted toward the longer-wavelength region, which corresponds to the red-shift of the absorption edge with doping. The photocurrent of $CaFe_2O_4$ was obtained at less than 600 nm, while that of Ag-, Au-, and CuO-$CaFe_2O_4$ was observed at 720 nm (Figure S6, Supporting Information). Therefore, it is speculated that cationic Ag, Cu, and Au may be introduced into the $CaFe_2O_4$ lattice to create a new level between the VB and/or CB in the bandgap. In the case of CuO-$CaFe_2O_4$, enhanced photoresponse was observed at longer wavelengths of 460−800 nm. The improvement of photocurrent by full-arc irradiation in Figure 1 is considered to be due to the improved photoresponse between 460 and 800 nm. However, the IPCE below 420 nm is lower than that for $CaFe_2O_4$, which indicates that CuO doping has not only a positive effect by the bathochromic shift but also a negative effect in the generation of electron and hole trap sites.[1] In the case of Au-$CaFe_2O_4$, the IPCE was lower than that of $CaFe_2O_4$ below 600 nm. A decrease of photocurrent should also be caused by the generation of trap sites with Au doping. However, this is contradicted by the 70% increase in photoresponse with full-arc irradiation (Figure 1). This result indicates that the improved photocurrent for Au-$CaFe_2O_4$ requires multicolor irradiation, i.e., excitation to both bandgap and Au plasmons. It is a possibility that the improved photocurrent may be due to localized surface plasmon resonance (LSPR) by Au plasmons.[17] Photoexcitation of the LSPR peak is known to form a locally enhanced electric field in the proximity of metal nanoparticles, which can then enhance the photoexcitation of chromophores near the metal nanoparticles. In the case of Au-$CaFe_2O_4$, the electric field induced by photoexcitation of the LSPR peak for Au nanoparticles (λ > 500 nm) may enhance the photoexcitation of $CaFe_2O_4$ (λ < 600 nm). Despite that Au acts as a trap site, the photocurrent by full-arc irradiation may be increased. In contrast, the IPCE for Ag-$CaFe_2O_4$ was much higher than that for $CaFe_2O_4$ over the entire wavelength region. Therefore, doping with Ag is effective not only for the absorption red-shift but also for an improvement of the photoresponse in the range of 340−760 nm. As reasons for photocurrent enhancement, Ag doping may

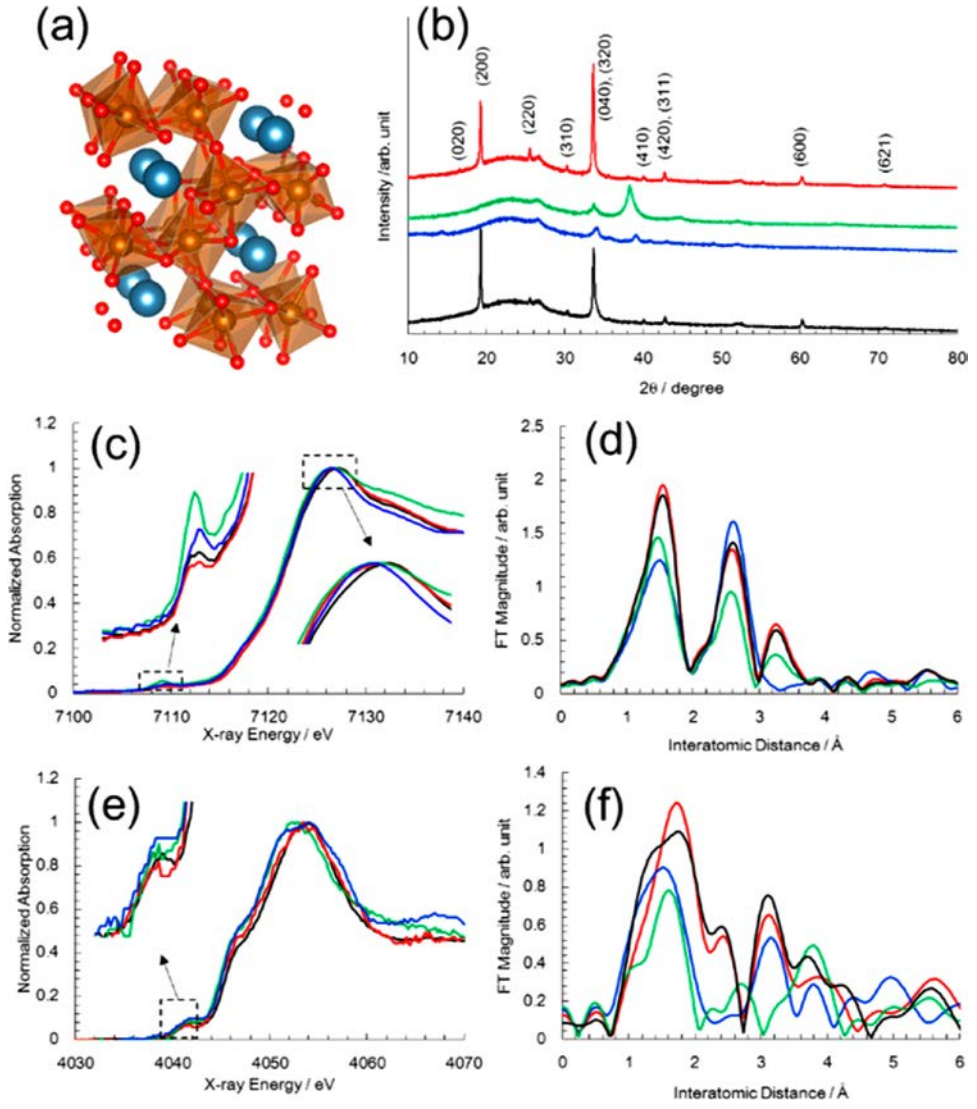

Figure 3. (a) Crystal structure of $CaFe_2O_4$ (Ca, blue; Fe, brown; O, red), (b) XRD patterns, and XANES and k^2-weighted FT-EXAFS spectra for Fe K-edge (c and d, respectively) and that for Ca K-edge (e and f, respectively) of Ag-$CaFe_2O_4$ (red), CuO-$CaFe_2O_4$ (blue), Au-$CaFe_2O_4$ (green), and $CaFe_2O_4$ (black) electrodes.

promote reaction with O_2 at the surface or improve bulk properties such as the carrier mobility.

To investigate the effect of Ag-doped sites and Ag particles for the reaction, a $CaFe_2O_4$ electrode loaded with Ag nanoparticles [Ag particle/$CaFe_2O_4$/ATO] and a Ag-doped $CaFe_2O_4$ electrode layer [Ag-$CaFe_2O_4$/$CaFe_2O_4$/ATO] were prepared. Photoinduced current−potential curves of these electrodes are shown in Figure S7 (Supporting Information), where the photocurrents of both electrodes were degraded. These results indicate that Ag-doped sites and Ag particles do not act as reduction sites to enhance the photocurrent in Ag-$CaFe_2O_4$.

To examine the bulk properties of Ag-$CaFe_2O_4$, the dependence of photocurrent on the film thickness was investigated. Photocurrent−voltage curves of 100−500 nm thick Ag-$CaFe_2O_4$ and $CaFe_2O_4$ films are shown in Figure S8 (Supporting Information). For $CaFe_2O_4$, the best photocurrent obtained at −0.25 V vs Ag/AgCl was for the 100 nm film and then decreased with increasing film thickness. The short carrier diffusion length in $CaFe_2O_4$ resulted in poor photoelectrochemical properties. This is disadvantageous for efficient light absorption because the majority of incident photons is transmitted through the thin film. In contrast, the optimum thickness of the Ag-$CaFe_2O_4$ film was 230 nm, and an efficient photocurrent was observed even at 500 nm. Therefore, more photons were absorbed in the thicker Ag-$CaFe_2O_4$ films, which can be explained by more photogenerated holes reaching the transparent electrode with improved carrier mobility. The enhancement of carrier mobility by Ag doping was estimated to be 4.6 times (Supporting Information). Consequently, the enhancement of the photoresponse with Ag doping is considered due to an improvement of the carrier mobility in the bulk. A detailed crystallographic analysis was then conducted to investigate the factors for improvement of the bulk properties with doping.

Figure 3b shows XRD patterns for Ag-, CuO-, and Au-doped $CaFe_2O_4$ and undoped $CaFe_2O_4$ electrodes. The undoped $CaFe_2O_4$ electrode has two intense peaks assignable to (200) and the overlap of (040) and (320), in addition to several weak peaks. Ag-$CaFe_2O_4$ also had intense peaks similar to that for $CaFe_2O_4$. The intensity of the (200) diffraction peak for Ag-$CaFe_2O_4$ was decreased slightly, while the other several peaks

were increased and shifted to lower angle by $\Delta 2\theta = 0.02-0.03°$ (Figure S10, Supporting Information). This indicates that doping with Ag induces a change of the crystal orientation in the film structure and the lattice spacing. In contrast, all of the peak intensities for the Au- and CuO-doped electrodes were decreased, and other peaks assignable to Au ($2\theta = 38.2°$) and CuO ($2\theta = 38.9°$) were observed. Films doped with Pd and Ir also showed a significant decrease in the $CaFe_2O_4$ peaks and the appearance of metallic phase dopant peaks.

XAFS spectra for the K-edge of Ca and Fe were measured to probe the short-range structure.[18] However, we could not obtain information on Ag because the dopant amounts were below the detection limit (less than 0.5 atom %). Figure 3c shows Fe K-edge X-ray absorption near edge structure (XANES) spectra for metal-doped $CaFe_2O_4$. Pre-edge peaks and absorption peaks were observed around 7109 and 7127 eV, respectively. The absorption maxima of Ag-$CaFe_2O_4$ were shifted to lower energy than that of $CaFe_2O_4$, which indicates that the electronic structure of Fe became reductive by Ag doping. The pre-edge peak of Ag-$CaFe_2O_4$ is lower than that of $CaFe_2O_4$ and is attributed to forbidden transitions such as 1s → 3d, which is allowed by degradation of the ligand-field symmetry around Fe due to p-character mixing with d orbitals. Therefore, the difference in the pre-edge peak indicates that Ag doping induces improvement of the symmetry around the Fe atom in $CaFe_2O_4$. In contrast, Au and CuO doping caused disturbance of the symmetry.

Figure 3d shows the Fourier transforms (FTs) of k^2-weighted extended X-ray absorption fine structure (EXAFS) spectra, which were collected for specific nearest-neighbor interatomic distances. The FT-EXAFS data showed three major peaks. $CaFe_2O_4$ has a distorted spinel structure (Figure 3a),[19] in which each Fe atom is surrounded by six O atoms in octahedral coordination. The first shell peak of the FT-EXAFS signal at ca. 1.6 Å is assigned to families of O atoms. The second shell peak at ca. 2.7 Å is assigned to single scattering by Fe−Ca and Fe−Fe atoms, while the third shell peak at ca. 3.2 Å represents contributions from both Ca, Fe, and O atoms. In the case of Ag-$CaFe_2O_4$, the FT magnitude of the first peak was higher than that of $CaFe_2O_4$, which also indicates improvement of the symmetry around Fe. The peak of the first shell was slightly shifted to longer interatomic distance with Ag doping. In contrast, the first shell shifted shorter, and the FT magnitude was lowered with Au and CuO doping.

The Ca K-edge XANES and FT-EXAFS spectra for metal-doped $CaFe_2O_4$ are shown in Figures 3e and 3f, respectively. These spectra contain much noise because the energy of the Ca K-edge is weak. The difference in the pre-edge and the absorption edge energy by doping could not be recognized. The FT-EXAFS data showed three major peaks. The first shell between 1.7 and 2.0 Å is attributed to single scattering by the surrounding eight O atoms. The other shells contain various scattering by Ca, Fe, and O atoms. The peak intensity of the first shell for Ag-$CaFe_2O_4$ is higher than that for $CaFe_2O_4$, which indicates the symmetry around Ca is also improved by Ag doping. In contrast, the first shell peak was more split and lowered by Au and CuO doping, which is considered to be because the symmetry of the Ca−O bond is lowered.

Decreasing symmetry is closely related to carrier mobility because mobility is highly dependent on the overlap of atomic orbitals. The CB minimum of $CaFe_2O_4$ consists of the Fe 3d, while the VB is mainly composed of Fe 3d and O 2p.[20,21] Therefore, the orbital overlap of the 3d orbitals of Fe with the 2p orbital of O^{2-} is important for the carrier mobility. The overlap must be significantly reduced by decreasing symmetry around Fe because of the narrow and anisotropic 3d orbital. Therefore, the low mobility is closely related to the distorted lattice structure. Doping with Ag induces an improvement in the symmetry around the central Fe atom. The structural improvement may also induce high mobility, which is considered to be the main reason for the significantly high photocurrent. These results introduce a new strategy for the formation of highly efficient semiconductor materials. This structural change by Ag doping may be applicable to other distorted oxide semiconductors.

In conclusion, various metal-doped $CaFe_2O_4$ semiconductors with *p*-type conductivity were produced by RF magnetron cosputtering. Doping of CuO, Au, and Ag resulted in an enhancement of the photocurrent. Although CuO and Au doping enhanced photocurrent by expansion of the absorption wavelength and plasmon resonance, respectively, the doping decreased the symmetry around the Fe center and the crystallinity of $CaFe_2O_4$. In contrast, Ag doping relaxed the distorted crystal structure of $CaFe_2O_4$ together with a red-shift in photoabsorption. As a result, Ag-doped $CaFe_2O_4$ exhibited 23 times higher photocurrent than undoped $CaFe_2O_4$. Ag-$CaFe_2O_4$ would be economically desirable as photocatalysts for environmental purification[13] and superhydrophilic reactions[14] and solar energy conversion[5,11,12] by conjugating *n*-type semiconductor since it is composed of naturally abundant elements.

■ ASSOCIATED CONTENT

Ⓢ Supporting Information

General procedures, photoelectrochemical property, and SEM and TEM images. This material is available free of charge via the Internet at http://pubs.acs.org.

■ AUTHOR INFORMATION

Corresponding Author

*E-mail: morikawa@mosk.tytlabs.co.jp.

Notes

The authors declare no competing financial interest.

■ ACKNOWLEDGMENTS

The authors thank Mai Asaoka, Kousuke Kitazumi, Naoko Takahashi, Toyokazu Nomoto, Masakazu Kanechika, and Keiichiro Oishi for assistances in the experiments. The Fe K-edge XAFS measurements were performed at the BL33XU of SPring-8 with the approval of the Japan Synchrotron Radiation Research Institute (JASRI) (Proposal No. 2013B7022).

■ REFERENCES

(1) Kudo, A.; Miseki, Y. Heterogeneous Photocatalyst Materials for Water Splitting. *Chem. Soc. Rev.* **2009**, *38* (1), 253−78.

(2) Hoffmann, M. R.; Martin, S. T.; Choi, W.; Bahnemann, D. W. Environmental Applications of Semiconductor Photocatalysis. *Chem. Rev.* **1995**, *95* (1), 69−96.

(3) Nozik, A. J. Photochemical Diodes. *Appl. Phys. Lett.* **1977**, *30* (11), 567−569.

(4) Khaselev, O.; Turner, J. A. A Monolithic Photovoltaic-photoelectrochemical Device for Hydrogen Production via Water Splitting. *Science* **1998**, *280* (5362), 425−427.

(5) Sato, S.; Arai, T.; Morikawa, T.; Uemura, K.; Suzuki, T. M.; Tanaka, H.; Kajino, T. Selective CO_2 Conversion to Formate

Conjugated with H_2O Oxidation Utilizing Semiconductor/Complex Hybrid Photocatalysts. *J. Am. Chem. Soc.* **2011**, *133* (39), 15240−3.
(6) Lin, Y.; Xu, Y.; Mayer, M. T.; Simpson, Z. I.; McMahon, G.; Zhou, S.; Wang, D. Growth of *p*-Type Hematite by Atomic Layer Deposition and Its Utilization for Improved Solar Water Splitting. *J. Am. Chem. Soc.* **2012**, *134* (12), 5508−5511.
(7) Chen, Y.; Crittenden, J. C.; Hackney, S.; Sutter, L.; Hand, D. W. Preparation of a Novel TiO_2-Based *p*−*n* Junction Nanotube Photocatalyst. *Environ. Sci. Technol.* **2005**, *39* (5), 1201−1208.
(8) Ida, S.; Takashiba, A.; Koga, S.; Hagiwara, H.; Ishihara, T. Potential Gradient and Photocatalytic Activity of an Ultrathin *p*-*n* Junction Surface Prepared with Two-Dimensional Semiconducting Nanocrystals. *J. Am. Chem. Soc.* **2014**, *136* (5), 1872−8.
(9) Meng, F.; Li, J.; Cushing, S. K.; Zhi, M.; Wu, N. Solar Hydrogen Generation by Nanoscale *p*−*n* Junction of *p*-type Molybdenum Disulfide/*n*-type Nitrogen-Doped Reduced Graphene Oxide. *J. Am. Chem. Soc.* **2013**, *135* (28), 10286−10289.
(10) Matsumoto, Y.; Obata, M.; Hombo, J. Photocatalytic Reduction of Carbon-dioxide on *p*-type $CaFe_2O_4$ Powder. *J. Phys. Chem.* **1994**, *98* (11), 2950−2951.
(11) Ida, S.; Yamada, K.; Matsunaga, T.; Hagiwara, H.; Matsumoto, Y.; Ishihara, T. Preparation of *p*-Type $CaFe_2O_4$ Photocathodes for Producing Hydrogen from Water. *J. Am. Chem. Soc.* **2010**, *132* (49), 17343−17345.
(12) Kim, E. S.; Nishimura, N.; Magesh, G.; Kim, J. Y.; Jang, J. W.; Jun, H.; Kubota, J.; Domen, K.; Lee, J. S. Fabrication of $CaFe_2O_4$/TaON Heterojunction Photoanode for Photoelectrochemical Water Oxidation. *J. Am. Chem. Soc.* **2013**, *135* (14), 5375−5383.
(13) Miyauchi, M.; Nukui, Y.; Atarashi, D.; Sakai, E. Selective Growth of *n*-Type Nanoparticles on *p*-Type Semiconductors for Z-Scheme Photocatalysis. *ACS Appl. Mater. Interfaces* **2013**, *5* (19), 9770−9776.
(14) Liu, Z.; Miyauchi, M. Visible-light Induced Superhydrophilicity on a WO_3/ITO/$CaFe_2O_4$ Heterojunction Thin Film. *Chem. Commun.* **2009**, *15*, 2002−2004.
(15) Matsumoto, Y.; Sugiyama, K.; Sato, E. I. Improvement of $CaFe_2O_4$ Photocathode by Doping with Na and Mg. *J. Solid State Chem.* **1988**, *74* (1), 117−125.
(16) Iwashina, K.; Kudo, A. Rh-Doped $SrTiO_3$ Photocatalyst Electrode Showing Cathodic Photocurrent for Water Splitting under Visible-Light Irradiation. *J. Am. Chem. Soc.* **2011**, *133* (34), 13272−13275.
(17) Torimoto, T.; Horibe, H.; Kameyama, T.; Okazaki, K.; Ikeda, S.; Matsumura, M.; Ishikawa, A.; Ishihara, H. Plasmon-Enhanced Photocatalytic Activity of Cadmium Sulfide Nanoparticle Immobilized on Silica-Coated Gold Particles. *J. Phys. Chem. Lett.* **2011**, *2* (16), 2057−2062.
(18) Nonaka, T.; Dohmae, K.; Araki, T.; Hayashi, Y.; Hirose, Y.; Uruga, T.; Yamazaki, H.; Mochizuki, T.; Tanida, H.; Goto, S. Quick-scanning X-ray Absorption Spectroscopy System with a Servo-motor-driven Channel-cut Monochromator with a Temporal Resolution of 10 ms. *Rev. Sci. Instrum.* **2012**, *83* (8), 5.
(19) Hill, P. M.; Peiser, H. S.; Rait, J. R. The Crystal Structure of Calcium Ferrite and β Calcium Chromite. *Acta Crystallogr.* **1956**, *9* (12), 981−986.
(20) Matsumoto, Y. Energy Positions of Oxide Semiconductors and Photocatalysis with Iron Complex Oxides. *J. Solid State Chem.* **1996**, *126* (2), 227−234.
(21) Obata, K.; Obukuro, Y.; Matsushima, S.; Nakamura, H.; Arai, M.; Kobayashi, K. Electronic Structure of $CaFe_2O_4$ with Antiferromagnetic Spin Ordering. *J. Ceram. Soc. Jpn.* **2013**, *121* (1417), 766−769.

Reprinted from ACS Applied Materials & Interfaces, Vol. 6, pp. 10969-10973 (http://dx.doi.org/10.1021/am502500y),

THE JOURNAL OF PHYSICAL CHEMISTRY B

Article

pubs.acs.org/JPCB

Dispersion of Rod-like Particles of Nafion in Salt-Free Water/1-Propanol and Water/Ethanol Solutions

Makoto Yamaguchi,*[,†] Takuro Matsunaga,[‡] Kazuki Amemiya,[¶] Akihiro Ohira,[†,§] Naoki Hasegawa,[‡] Kazuhiko Shinohara,[†,#] Masaki Ando,[¶] and Toshihiko Yoshida[¶]

[†]Fuel Cell Cutting-edge Research Center (FC-Cubic), Technology Research Association, AIST Tokyo Waterfront Main Building, 2-3-26 Aomi, Koto-ku, Tokyo 135-0064, Japan

[‡]Toyota Central R&D Laboratories, Inc., 41-1 Yokomichi, Nagakute, Aichi 480-1192, Japan

[¶]Higashifuji Technical Center, Toyota Motor Corporation, 1200 Mishuku, Susono, Shizuoka 410-1193, Japan

[§]Research Institute for Ubiquitous Energy Devices, National Institute of Advanced Industrial Science and Technology (AIST), 1-8-31 Midorigaoka, Ikeda, Osaka 563-8577, Japan

[#]Nissan Research Center, Nissan Motor Company, Limited, 1 Natsushima-cho, Yokosuka, Kanagawa 237-8523, Japan

Supporting Information

ABSTRACT: The dispersion of perfluorinated sulfonic acid ionomers in catalyst inks is an important factor controlling the performance of catalyst layers in membrane electrode assemblies of proton exchange membrane fuel cells (PEMFCs). The effect of water/alcohol composition on the dispersion of H-Nafion in water/1-propanol and water/ethanol solutions was studied by dynamic light scattering (DLS), small-angle X-ray scattering (SAXS), and ^{19}F nuclear magnetic resonance (^{19}F NMR) spectroscopy. Hydrodynamic radii calculated from DLS decay profiles and the radii and interparticle distance of rod-like particles derived from SAXS profiles showed almost the same dependence on alcohol concentration. 1-Propanol was more effective than ethanol to induce changes in the characteristic lengths of the rod-like particles. The motional narrowing in the ^{19}F NMR spectra by addition of 1-propanol indicates selective solvation of the rod-like particles. We suppose this might have decreased their radii and induced their elongation, which eventually led to extension of the ordered regions as observed in the hydrodynamic radii. Our study helps to clarify the dispersion of Nafion in aqueous alcohol solutions, which has implications for the performance of PEMFCs.

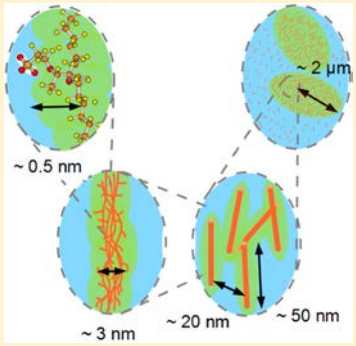

1. INTRODUCTION

Perfluorosulfonic acid (PFSA) ionomers such as Nafion have been widely used as proton-conducting materials in polymer electrolyte membrane fuel cells not only as the membrane-separating anode and cathode but also the ionomer in the catalyst layer.[1] The catalyst layer is prepared by drying a catalyst ink containing catalyst and ionomer particles, so it is important to understand their dispersion and interaction in the ink to improve the properties of the resulting catalyst layer.[2−5]

For ionomer dispersion, we can refer to previous studies on Nafion in polar solvents.[6−8] Aldebert et al.[9] claimed that rod-like particles of Nafion are homogeneously dispersed in polar solvents based on the concentration dependence of interference peaks in small-angle neutron scattering (SANS) and small-angle X-ray scattering (SAXS) profiles. The radii of the rod-like Nafion particles depended on interfacial energies rather than the dielectric constants of the solvents, because each particle was assumed to be an aggregate of several polymer chains forming a core with their hydrophobic perfluorinated backbones and sulfonates located on its surface.[10] Several analytical procedures of small-angle scattering profiles gave fairly consistent values of around 20−25 Å for the radii of Nafion particles dispersed in various polar solvents.[11] PFSA ionomers with short pendant chains also formed rod-like particles with slightly smaller radii of around 15−17 Å in polar solvents.[12] The degree of solvent penetration into the rod-like particles was probed by electron spin resonance measurements of spin-probe molecules, and a fringed rod model was proposed to explain the interaction of the rod-like particles at higher concentration.[13−16] Transmission electron microscopy (TEM) images of Nafion observed at low temperature show wormlike objects with a length of around 30 nm, which is in good agreement with that estimated from small-angle scattering measurements.[4,17]

However, recent studies on the PFSA ionomer dispersions show results which seem inconsistent with the traditional rod-like particle model. TEM images of Nafion solutions by freeze-dried specimen show larger aggregates of submicron scale.[8,18−20] Dynamic light scattering (DLS) measurements of Nafion solutions also give hydrodynamic radii ranging from 0.1 to 10 μm, so these larger values were attributed to secondary aggregation of the fringed rods in protic solvents.[21−24] In

Received: July 8, 2014
Revised: November 21, 2014
Published: November 24, 2014

contrast, Nafion in aprotic solvents forms smaller particles with diameters of <100 nm according to static light scattering (SLS) experiments,[18] suggesting Nafion aggregation is more sensitive to solvent properties than the shape and size of the rod-like particles. Recently, Welch et al.[25] claimed that the shape and size of primary particles of Nafion are more drastically affected by solvents than previously assumed. Their SANS profiles of Nafion in water/2-propanol showed significant swelling of the particles to >200 nm, while TEM images of the same system published by Ngo et al.[19] show aggregates of <100 nm.

It seems there is still no consistent understanding of the dispersion of PFSA ionomers in various polar solvents at different length scales from the shape and size of the primary particles to formation of their aggregates. Most previous papers have focused on either the primary particles or aggregates, and there are few studies discussing the relationship between these scales. Thus, here we used DLS, SAXS, and ^{19}F NMR spectroscopy to see how conformational changes in the primary particles of Nafion probed by NMR and SAXS affect its aggregation evaluated by DLS. Water/alcohol mixtures were used not only because they are the most fundamental systems to understand the effect of selective solvation on structural development but also because they are actually employed in catalyst ink solutions.

2. EXPERIMENTAL METHODS

Nafion PFSA polymer dispersion (D2020, DuPont Fuel Cells, Wilmington, DE; Nafion (EW 1100 g mol^{-1}) 21.9 wt %, water 32.6 wt %, 1-propanol 45 wt %, others 0.5 wt %) was diluted with purified water (Kishida Chemical, Osaka, Japan, deionized, SiO_2 <0.05 ppm) and either 1-propanol (Kishida Chemical, 99.5%) or ethanol (Kishida Chemical, 99.5%) to prepare Nafion solutions with different proportion of water and alcohol as summarized in Table 1. Reagents were used without further purification. Although solutions prepared by addition of ethanol to the original solution contain a small amount of 1-propanol, they are hereafter denoted as water/ethanol solutions for convenience except for cases where solvent composition is specified. The Nafion concentration in all solutions is 30 g dm^{-3} unless otherwise stated.

Table 1. Solvent Composition[a] Water/Alcohol Solutions of Nafion

water/1-propanol	water/ethanol/1-propanol
98/2	98/0/2
90/10	88/10/2
76/24	72/25/3
48/52	43/53/4
16/84	13/81/6

[a]Mole fraction, %.

DLS was performed with a DLS/SLS apparatus (ALV5000, ALV, Germany). Sample temperature was maintained at 25 ± 0.03 °C. The light source was a 22 mW He−Ne laser (λ = 632.8 nm). In the DLS measurements, intensity correlation functions were obtained for 60 s at 90°. The distribution functions of translational diffusion coefficients were obtained by the inverse Laplace transform of each correlation function, using the CONTIN algorithm.[26] The distribution function of hydrodynamic radii, R_h, was calculated with the Stokes−Einstein equation, using the viscosity and refractive index of the solvent.

SAXS profiles were measured at the BL33XU beamline of SPring-8, Hyogo, Japan. The X-ray beam was monochromatized to 0.827 Å with a two-crystal monochromator. Sample solutions in polyimide tubes (2 mm o.d.) were irradiated with an X-ray beam collimated to a height of 0.3 mm and width of 0.4 mm for 1 min per sample. Scattered photons were detected with a two-dimensional semiconductor detector (PILATUS-300 K, 487 × 619 pixels, pixel size 0.172 × 0.172 mm, Dectris, Switzerland) with sample-to-detector distances of 4.5 and 0.05 m. The measured data were plotted as relative scattering intensity profiles after corrections for dark current, background, transmittance, and solid angle.

NMR spectra of ^{19}F nuclei were measured with an NMR spectrometer (ECA-500, JEOL, Japan) with a superconducting magnet of 11.747 T, which corresponds to a resonance frequency of 470.62 MHz for ^{19}F. The sample was transferred to a glass tube (5 mm o.d.) and free induction decay signals after each $\pi/4$ pulse (3.7 μs) were collected at 20 °C at intervals of 5 s and then Fourier transformed to obtain NMR spectra. Baseline correction of the spectra was performed manually to facilitate comparison of peak intensities. The peak from the backbone CF_2 units was set to −123 ppm in all spectra.[27]

3. RESULTS

3.1. DLS. Figure 1 shows intensity−intensity time autocorrelation functions of water/1-propanol and water/

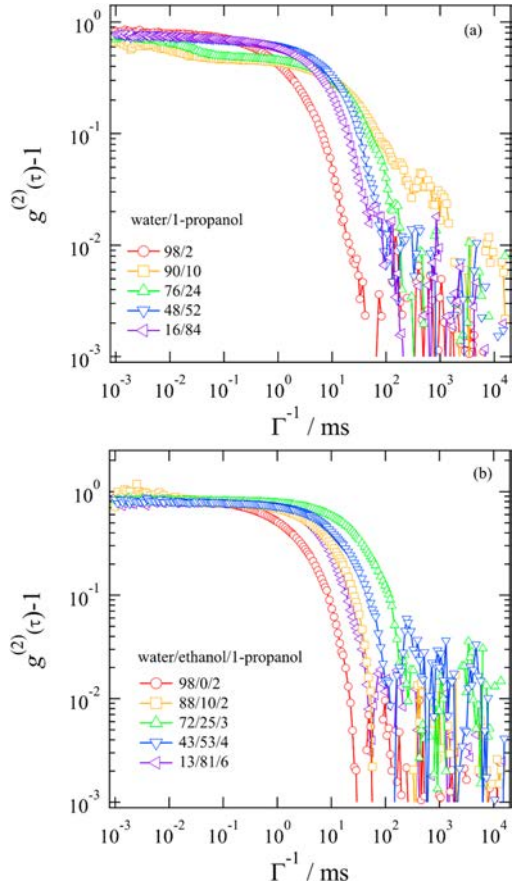

Figure 1. DLS autocorrelation function decay profiles of H-Nafion in water−alcohol solutions with different compositions: (a) water/1-propanol and (b) water/ethanol.

ethanol solutions of Nafion. In all the cases, the autocorrelation functions decay to 1% within 1 s. For the polyelectrolyte solutions, there are fast and slow decay components in the DLS decay curves. Although two such components are clearly identified for the water/1-propanol 90/10 and 76/24 solutions, the fast component is absent and only the slow relaxation component is observed in other cases. In previous literature, the presence of the fast relaxation mode in the decay of the autocorrelation functions of salt-free Nafion solutions depends on various factors such as solute concentration, solvent species, and composition.[7,24] Thus, we discuss only the changes in the decay constants of the slow relaxation mode that is observed in all the sample solutions.

The decay profiles of the autocorrelation functions of the sample solutions diluted with water alone, i.e., water/1-propanol 98/2 in Figure 1a and water/ethanol/1-propanol 98/0/2 in Figure 1b, show the fastest decay. Addition of either 1-propanol or ethanol causes the autocorrelation functions to decay more slowly, although the effects of 1-propanol and ethanol are slightly different. The decay is the slowest at the mole ratio of either 90/10 in water/1-propanol or 72/25/3 in water/ethanol/1-propanol, and the decay constants become shorter as the fraction of 1-propanol or ethanol increases. These changes in decay constants are shown in Figure 2 as

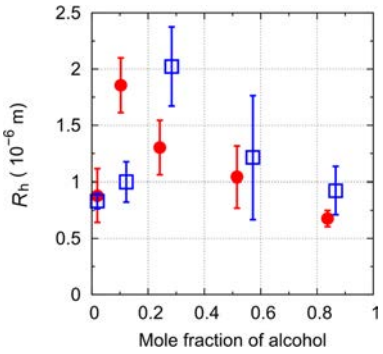

Figure 2. Hydrodynamic radius R_h calculated from self-diffusion coefficients of DLS decay profiles: (solid circles) water/1-propanol and (open squares) water/ethanol. Each sample was measured five times to calculate average and error.

hydrodynamic radii plotted against the total mole fraction of alcohols in the solvents. The mole fraction of alcohol that gives the largest hydrodynamic radius is higher for ethanol than 1-propanol. In other words, 1-propanol is more effective than ethanol to induce certain inhomogeneity in the Nafion solution, while the spatial extent of the inhomogeneity expressed as hydrodynamic radii is higher for ethanol than 1-propanol.

Changes in the decay of the autocorrelation functions caused by increasing mole ratio of alcohol to Nafion solution have already been observed in the case of water and 2-propanol solutions by Ngo et al.,[19] although Nafion concentration was far more dilute (0.6 g dm^{-3}) than in the present case (30 g dm^{-3}). Hydrodynamic radii were the largest for the solutions containing 45−55 wt % (20−27 mol %) 2-propanol, although their estimated values of 120−180 nm are about 10 times smaller than the present values. We suppose that the smaller hydrodynamic radii determined by Ngo and co-workers compared within this work are mainly caused by the much lower concentration of Nafion in their study. The concentration dependence of Nafion from 1 to 50 g dm^{-3} was briefly studied for water/1-propanol 98/2 and 16/84 solutions. Estimated hydrodynamic radii increased nearly 10 times with Nafion concentration in both solutions, and 16/84 solutions always showed larger R_h than 98/2 solutions.

3.2. SAXS. Figure 3 shows SAXS profiles of Nafion in water/alcohol solutions with different compositions. The SAXS

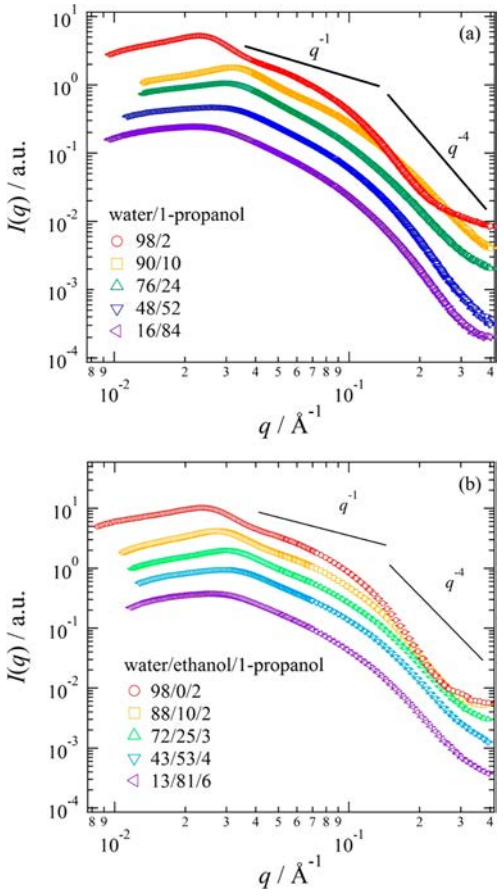

Figure 3. SAXS profiles of Nafion in water−alcohol solutions: (a) water/1-propanol and (b) water/ethanol. Profiles are vertically shifted to avoid overlap.

profiles of the aqueous solutions (water/1-propanol 98/2 and water/ethanol/1-propanol 98/0/2) show distinct maxima at $q_{max} \approx 0.023$ Å^{-1}, where $q \equiv (4\pi/\lambda) \sin\theta$ is the magnitude of the scattering vector. On the higher q side of this maximum, the profile shows approximately q^{-1} dependence up to $q \approx 0.1$, which then changes to approximately q^{-4} dependence. Upon increasing the mole fraction of 1-propanol to 10% (water/1-propanol 90/10), the SAXS profile at $q < 0.1$ Å^{-1} shifts to higher q and lower $I(q)$ values with $q_{max} = 0.032$ Å^{-1}, as shown in Figure 3a. However, when the fraction of 1-propanol is increased further, the maximum shifts toward smaller q with considerable broadening. SAXS profiles of water/ethanol solutions are very similar to those of the water/1-propanol solutions, as shown in Figure 3b, except that the scattering maxima shift to larger q value until the mole fraction of ethanol reaches 25%.

The SAXS profiles ($q = 0.04$−0.2 Å^{-1}) of Nafion in water/1-propanol were fitted by scattering curves of cylindrical objects, as shown in Figure 4a. Their radii were adjusted to reproduce changes in q dependence at 0.1−0.2 Å^{-1} from q^{-1} to q^{-4}. The length of the cylindrical object may also be deduced in principle from the onset of changes in q dependence of $I(q)$ from q^0 to

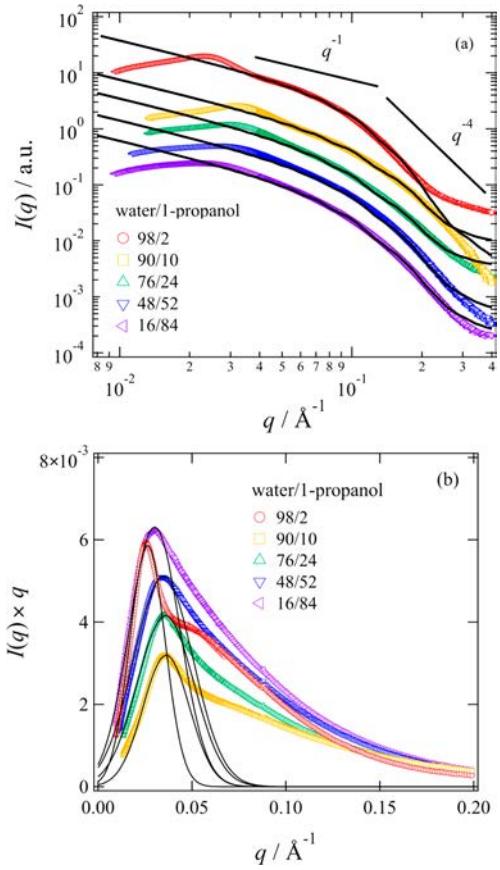

Figure 4. Curve fittings of SAXS profiles of Nafion in water/1-propanol solutions. (a) $I(q)$ profiles and simulated curves assuming cylindrical objects. Profiles were vertically shifted to avoid overlap. (b) $I(q) \times q$ profiles fitted with Gaussian functions to locate q_{max}.

q^{-1} at the smaller q. Unfortunately this region was obscured by scattering maxima because of high solute concentration, so the cylindrical objects were assumed to be infinitely long in the fitted curves in Figure 4a.

We next identified the location of the scattering maxima in the $I(q)$ profiles. The peaks were fairly broad, so it was difficult to obtain reliable values directly from the $I(q)$ profiles. Because scattering maxima arise from structure factors $S(q)$, their approximate profiles were obtained by assuming that the form factor $P(q)$ was proportional to q^{-1} as described above and thus $S(q) \approx I(q)/P(q) \approx I(q) \times q$. The simulated $S(q)$ of Nafion in water/1-propanol are shown in Figure 4b, with maxima fitted with Gaussian functions. It should be noted that a secondary maximum appears at ~0.06 Å^{-1} only for the 98/2 water/1-propanol mixture. The measured and simulated SAXS profiles of Nafion in water/ethanol mixtures are shown in the Supporting Information.

The radii of the cylindrical objects derived from the fitted curves in Figure 4a for Nafion in water/1-propanol are plotted against alcohol fraction in Figure 5a. The radius decreases from 1.4 to 0.9 nm as the mole fraction of 1-propanol increases from 2% to 10% or 24%. In contrast, the minimum value was obtained for the alcohol (ethanol + 1-propanol) mole fraction of 57%. In the case of water/ethanol solutions, the radius decreases as the mole fraction of ethanol in the solvent increases.

Figure 5b shows interparticle distances of the rod-like particles estimated from the maxima of the structure factors

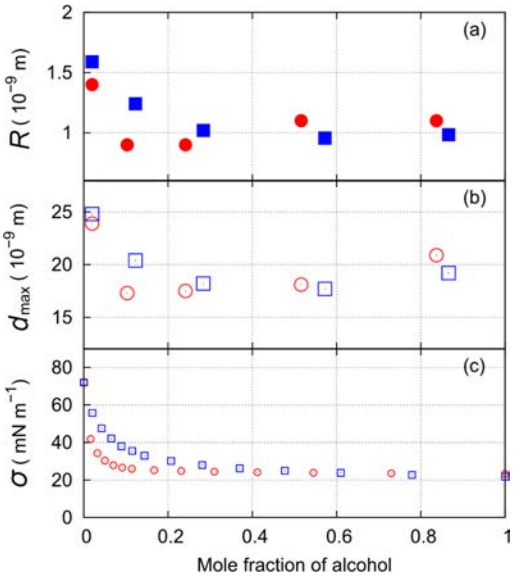

Figure 5. Dependence of characteristic lengths of Nafion in water–alcohol mixtures on alcohol fraction: (circles) water/1-propanol; (squares) water/ethanol. (a) Radii of rod-like objects from fitting $I(q)$ profiles; (b) interparticle distance of rod-like objects $d_{max} = 2\pi/q_{max}$; and (c) surface tension of water–alcohol mixtures (ref 28).

q_{max} depicted in Figure 4b as $d_{max} = 2\pi/q_{max}$. The changes of q_{max} with alcohol fraction are almost parallel to those of the radii of the cylindrical objects presented in Figure 5a. For water/1-propanol solutions, the mole fraction giving the smallest R and d_{max} values is ~0.1, while it is ~0.5 for water/ethanol solutions.

In previous studies, the radii of the rod-like particles of Nafion in different solvents have been explained by the interfacial energy between the solvent and air or polytetrafluoroethylene polymer.[10] Figure 5c shows the surface tension of water/1-propanol and water/ethanol mixtures at 25 °C, which decreases rapidly as alcohol fraction increases.[28] 1-Propanol reduces the surface tension more than ethanol, which is consistent with the changes in estimated radii shown in Figure 5a. Pure 1-propanol and ethanol show almost identical surface tensions, which can explain the smallest radii of the rod-like particles in the water/1-propanol and water/ethanol solutions at high alcohol fraction.

The scattering maxima in the SAXS profiles of the samples with high water fraction are caused by interference between the rod-like particles with a certain ordered structure in solution, such as a two-dimensional hexagonal array.[9−12] For a model of infinitely long cylinders, the radius can be estimated from d_{max} and the volume fraction ϕ of the ionomer is

$$R = \left(\frac{2}{\pi\sqrt{3}}\right)^{1/2} \phi^{1/2} d_{max} \quad (1)$$

By assuming the density of the ionomer is 2.1 g cm^{-3}, corresponding to ϕ = 1.4% for the 30 g dm^{-3} solutions, the calculated radii of the rod-like particles are 1.3−1.8 nm, which are slightly larger than the values shown in Figure 5a. While Loppinet et al.[11] obtained slightly larger radii for Li-Nafion particles in water (2.4 nm) and ethanol (2.0 nm) with this procedure, the values recently reported by Xu et al.[4] are slightly smaller (1.5 nm) and closer to our results. In any case, although the absolute values of the radii of the rod-like particles are

dx.doi.org/10.1021/jp506814m | J. Phys. Chem. B 2014, 118, 14922−14928

different, the present study confirms the reported observation that their radii are larger in aqueous solution than in alcohol ones.

3.3. NMR. Figure 6 illustrates ^{19}F NMR spectra of Nafion in water/1-propanol. The measured spectra are very similar to

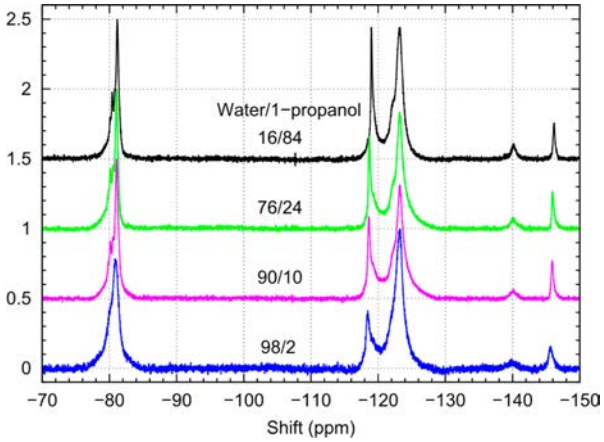

Figure 6. ^{19}F NMR spectra of Nafion in water/1-propanol solutions of different composition. Each spectrum is normalized against the strongest peak. Spectra are plotted with shifted baselines to avoid overlap.

those in previous studies of Nafion in 1-propanol[27] or ethanol,[29,30] and show peaks at around −81 (CF_3, OCF_2), −118 (SCF_2), −123 (backbone CF_2), −140 (backbone CF), and −146 ppm (side chain CF). Each spectrum in this figure is normalized to its strongest peak at either −123 or −81 ppm. In the spectrum of the water/1-propanol 98/2 mixture, the peak of the backbone CF_2 at −123 ppm is the strongest and the strongest side chain peak at −81 ppm does not show resolved structure but only a shoulder at −80 ppm. At higher 1-propanol fraction, this peak at ca. −81 ppm splits into several sharp peaks; the strongest singlet at −81 ppm is assigned to CF_3 and the multiplet at ca. −80 ppm is assigned to OCF_2 in the side chain. The peak at −146 ppm from the side chain CF to which CF_3 is attached changes in parallel with the CF_3 peak; the peak becomes narrower and its relative intensity is almost constant throughout as the mole fraction of 1-propanol changes above 0.1. These changes imply motional narrowing of the side chain caused by solvation of the hydrophobic perfluorinated polymers by the alkyl group of 1-propanol. In contrast, changes in the peaks from the OCF_2 and SCF_2 units at −80 and −118 ppm, respectively, are more gradual and are strongest in the solution with the highest 1-propanol fraction. Because these units are closer to the negatively charged sulfonate located at the end of the side chain, water molecules around them are more gradually replaced by 1-propanol compared with the case for the CF and CF_3 groups closer to the backbone. As for the backbone peaks, the CF peak at −140 ppm becomes narrower as the mole fraction of 1-propanol increases. Changes in the strongest backbone CF_2 peak at −123 ppm are less obvious, although the line width becomes slightly narrower at higher 1-propanol fraction.

4. DISCUSSION

We used two scattering methods to probe structural information about scattering objects at different length scales of Nafion dispersed in water/1-propanol and water/ethanol mixtures by changing the mole ratio of water and alcohol. It is noteworthy that the characteristic lengths obtained by the two methods, i.e., radii and mutual separation of the rod-like particles from the SAXS profiles and the hydrodynamic radii from the DLS decay curves, approach the largest or smallest values, respectively, at the same mole fraction of ∼0.1 for 1-propanol and >0.3 for ethanol. Thus, it is anticipated that certain physical principles might be relevant for both of these parallel changes in characteristic lengths.

As noted above, changes in the radii of the rod-like particles are explained by the interfacial energies of the water−alcohol mixtures. Because the particle volume is considered to be unaffected by the solvent composition at ambient temperature and pressure, the rod-like particles become longer as their radii decrease.[10] If one assumes that highly dispersed Nafion has $M_w \approx 2.5 \times 10^5$ g mol^{-1} [31,32] and a density of 2 g cm^{-3}, calculated rod lengths are 30 and 66 nm for radii of 1.5 and 1.0 nm, respectively. Thus, the smaller interparticle distance at higher alcohol fraction is associated with thinner, elongated rod-like particles. It should be noted that at a concentration of 30 g dm^{-3}, the interparticle distance in a homogeneous distribution of particles is estimated to be 24 nm. This value is smaller than the estimated lengths of the rod-like particles in water−alcohol mixtures with alcohol fraction >0.1 and consequently they are expected to exhibit orientational order to some extent, as already assumed in our use of the hexagonal array model. In addition, recent theoretical studies point out the possibility of the electrostatic interaction between charged rod-like particles to become attractive in salt-free solutions.[33,34] These effects explain the observed decrease in interparticle distance as the alcohol fraction in the solvent mixtures increases.

Interparticle distances smaller than the average value of the homogeneous distribution mean there is inhomogeneous spatial distribution of the rod-like particles. Loppinet et al.[11] analyzed their results with a homogeneous distribution of the particles with a limited extent of local order and rejected the two-state structure model. The two-state model assumes ordered and disordered regions are present,[35] and it seems plausible to explain the larger structures observed by SANS and DLS. However, it is still unclear how the size of the clusters in the ordered regions is governed in the two-state structure model. For sodium polystyrenesulfonate (NaPSS) in water, SANS profiles at very small angle gave estimated radii of the ordered domains of 40−100 nm.[36] Hydrodynamic radii estimated from slow diffusion coefficients measured by DLS were 100−400 nm, which were larger but of the same order as those determined by SANS analyses.[37,38] In the present case, the rod-like shape of the particles might have introduced orientational order and stronger attractive interaction, which would eventually have resulted in more extended clusters in the ordered regions than in the case of NaPSS in water. Introduction of alcohol causes the rod-like particles to elongate because of selective solvation by alcohol. As a result, the attractive electrostatic interaction between particles is enhanced and consequently the average interparticle distance is decreased. It is also expected that the area of the ordered region is enlarged when the attractive interaction is stronger, as observed in the estimated hydrodynamic radii in Figure 2. However, the shape of the rod-like particles gradually becomes obscured by solvent penetration as alcohol fraction increases further, as proposed in the fringed rod model.[13−16] These changes might have weakened the attractive interaction and consequently the ordered region becomes smaller.

At the polymer concentration range used in this study, the estimated interparticle distances indicate that the rod-like particles do not form dense aggregates in the ordered regions. Such aggregates observed in the TEM images of the Nafion solutions are probably formed during preparation of freeze-dried samples. However, the TEM images seem to reflect changes in the shape of the rod-like particles in the ordered regions with solvent composition. For example, in a reported series of TEM images of Nafion in water/isopropanol mixture solvents, spherical primary particles change to rod-like and their aggregates become larger as isopropanol fraction increases.[19] The aggregates become smaller as both the number and size of the primary particles decrease as the isopropanol fraction increases further. These changes in the size and shape of the primary particles with solvent composition are the same in the present case.

However, SANS profiles suggested the presence of highly swollen clusters (>200 nm) in water/2-propanol solution,[25] which does not seem compatible with the TEM images. This SANS analysis was based on a model proposed by Hammouda et al.[39] that includes a term describing local polymer−solvent interaction to reproduce scattering maxima, which appeared at around q = 0.035 Å^{-1} and disappeared at higher alcohol fraction. Their SANS profile of an aqueous solution showed steeper decrease at q > 0.1 Å^{-1} than the profiles of the water/2-propanol solutions. These characteristics were also observed in the SAXS profiles of Nafion in water/alcohol mixtures shown in Figure 3. We suppose that the SANS profiles of Nafion in water/2-propanol can be analyzed by assuming rod-like scattering objects, and their sizes and interparticle distances would be very similar to those found in the present case.

5. CONCLUSIONS

Dispersion of H-Nafion in water/1-propanol and water/ethanol solutions was studied by DLS, SAXS, and ^{19}F NMR spectroscopy. The hydrodynamic radii of the ordered regions determined by DLS and the radii and interparticle distances of the rod-like particles evaluated by SAXS showed almost parallel changes with water/alcohol composition. Selective solvation of the particles by alcohol was revealed by motional narrowing of the peaks in the ^{19}F NMR spectra, and this was assumed to have induced elongation of the rod-like particles and consequently the development of ordered regions. Further studies are planned to clarify the presence of ordered regions and estimate their size by small-angle scattering at q < 0.01 Å^{-1} as well as direct observation by nanoparticle tracking analysis and fast atomic force microscopy.

■ ASSOCIATED CONTENT

Ⓢ Supporting Information

Curve fittings of SAXS profiles of Nafion in water/ethanol solutions. This material is available free of charge via the Internet at http://pubs.acs.org.

■ AUTHOR INFORMATION

Corresponding Author

* Phone: 81-3-3599-2364. Fax: 81-3-3529-2303. E-mail: m-yamaguchi@fc-cubic.or.jp.

Notes

The authors declare no competing financial interest.

■ ACKNOWLEDGMENTS

Part of this work was financially supported by the Ministry of Economy, Trade and Industry (METI) and the New Energy and Industrial Technology Development Organization (NEDO), Japan. The synchrotron radiation experiments were performed at BL33XU of SPring-8 with the approval of the Japan Synchrotron Radiation Research Institute (JASRI) (Proposal No. 2013A7003). The authors thank Prof. Mitsuhiro Shibayama of the University of Tokyo for DLS measurements and Yuichi Inoue, Kuon Miyazaki, and Naoki Sakamoto of Asahi Kasei Corporation for discussion about the properties of ionomer solutions.

■ REFERENCES

(1) Holdcroft, S. Fuel Cell Catalyst Layers: A Polymer Science Perspective. *Chem. Mater.* **2014**, *26*, 381−393.

(2) Ma, S.; Chen, Q.; Jøgensen, F. H.; Stein, P. C.; Skou, E. M. ^{19}F NMR Studies of Nafion Ionomer Adsorption on PEMFC Catalysts and Supporting Carbons. *Solid State Ionics* **2007**, *178*, 1568−1575.

(3) Mizukawa, H.; Kawaguchi, M. Effects of Perfluorosulfonic Acid Adsorption on the Stability of Carbon Black Suspensions. *Langmuir* **2009**, *25*, 11984−11987.

(4) Xu, F.; Zhang, H. Y.; Ilavsky, J.; Stanciu, L.; Ho, D.; Justice, M. J.; Petrache, H. I.; Xie, J. Investigation of a Catalyst Ink Dispersion Using Both Ultra-Small-Angle X-ray Scattering and Cryogenic TEM. *Langmuir* **2010**, *26*, 19199−19208.

(5) Shibayama, M.; Matsunaga, T.; Kusano, T.; Amemiya, K.; Kobayashi, N.; Yoshida, T. SANS Studies on Catalyst Ink of Fuel Cell. *J. Appl. Polym. Sci.* **2014**, *131*, DOI: 10.1002/app.39842.

(6) Moore, R. B., III; Martin, C. R. Chemical and Morphological Properties of Solution-Cast Perfluorosulfonate Ionomers. *Macromolecules* **1998**, *21*, 1334−1339.

(7) Lin, H.-L.; Yu, T. L.; Huang, C.-H.; Lin, T.-L. Morphology Study of Nafion Membranes Prepared by Solutions Casting. *J. Polym. Sci., Part B: Polym. Phys.* **2005**, *43*, 3044−3057.

(8) Ma, C.-H.; Yu, T. L.; Lin, H.-L.; Huang, Y.-T.; Chen, Y.-L.; Jeng, U.-S.; Lai, Y.-H.; Sun, Y.-S. Morphology and Properties of Nafion Membranes Prepared by Solution Casting. *Polymer* **2009**, *50*, 1764−1777.

(9) Aldebert, P.; Dreyfus, B.; Pineri, M. Small-Angle Neutron Scattering of Perfluorosulfonated Ionomers in Solution. *Macromolecules* **1986**, *19*, 2651−2653.

(10) Aldebert, P.; Dreyfus, B.; Gebel, G.; Nakamura, N.; Pineri, M.; Volino, F. Rodlike Micellar Structures in Perfluorinated Ionomer Solutions. *J. Phys. (Paris)* **1988**, *49*, 2101−2109.

(11) Loppinet, B.; Gebel, G.; Williams, C. E. Small-Angle Scattering Study of Perfluorosulfonated Ionomer Solutions. *J. Phys. Chem. B* **1997**, *101*, 1884−1892.

(12) Loppinet, B.; Gebel, G. Rodlike Colloidal Structure of Short Pendant Chain Perfluorinated Ionomer Solutions. *Langmuir* **1998**, *14*, 1977−1983.

(13) Szajdziniska-Pietek, E.; Schlick, S.; Plonka, A. Self-Assembling of Perfluorinated Polymeric Surfactants in Water. Electron Spin Resonance Spectra of Nitroxide Spin Probes in Nafion Solutions and Swollen Membranes. *Langmuir* **1994**, *10*, 1101−1109.

(14) Szajdziniska-Pietek, E.; Schlick, S.; Plonka, A. Self-Assembling of Perfluorinated Polymeric Surfactants in Nonaqueous Solvents. Electron Spin Resonance Spectra of Nitroxide Spin Probes in Nafion Solutions and Swollen Membranes. *Langmuir* **1994**, *10*, 2188−2196.

(15) Szajdziniska-Pietek, E.; Pilar, J.; Schlick, S. Structure and Dynamics of Perfluorinated Ionomers in Aqueous Solutions and Swollen Membranes Based on Simulations of ESR Spectra from Spin Probes. *J. Phys. Chem.* **1995**, *99*, 313−319.

(16) Li, H.; Schlick, S. Effect of Solvents on Phase Separation in Perfluorinated Ionomers, from Electron Spin Resonance of VO^{2+} in Swollen Membranes and Solutions. *Polymer* **1995**, *36*, 1141−1146.

(17) Rubatat, L.; Gebel, G.; Diat, O. Fibrillar Structure of Nafion: Matching Fourier and Real Space Studies of Corresponding Films and Solutions. *Macromolecules* **2004**, *37*, 7772−7783.
(18) Liu, W.-H.; Yu, T.-Y.; Yu, T. L.; Lin, H.-L. Static Light Scattering and Transmission Microscopy of Dilute Nafion Solutions. *e-Polym.* **2007**, *7*, 1264−1271.
(19) Ngo, T. T.; Yu, T. L.; Lin, H.-L. Influence of the Composition of Isopropyl Alcohol/Water Mixture Solvents in Catalyst Ink Solutions on Proton Exchange Membrane Fuel Cell Performance. *J. Power Sources* **2013**, *225*, 293−303.
(20) Ngo, T. T.; Yu, T. L.; Lin, H.-L. Nafion-based Membrane Electrode Assemblies Prepared from Catalyst Inks Containing Alcohol/Water Solvent Mixtures. *J. Power Sources* **2013**, *238*, 1−10.
(21) Cirkel, P. A.; Okada, T.; Kinugasa, S. Equilibrium Aggregation in Perfluorinated Ionomer Solutions. *Macromolecules* **1999**, *32*, 531−533.
(22) Cirkel, P. A.; Okada, T. A Comparison of Mechanical and Electrical Percolation during the Gelling of Nafion Solutions. *Macromolecules* **2000**, *33*, 4921−4925.
(23) Jiang, S.; Xia, K.-Q.; Xu, G. Effect of Additives on Self-Assembling Behavior of Nafion in Aqueous Media. *Macromolecules* **2001**, *34*, 7783−7788.
(24) Lee, S.-J.; Yu, T. L.; Lin, H.-L.; Liu, W.-H.; Lai, C.-L. Solution Properties of Nafion in Methanol/Water Mixture Solvent. *Polymer* **2004**, *45*, 2853−2862.
(25) Welch, C.; Labouriau, A.; Hjelm, R.; Orler, B.; Johnston, C.; Kim, Y. S. Nafion in Dilute Solvent Systems: Dispersion or Solution? *ACS Macro Lett.* **2012**, *1*, 1403−1407.
(26) Provencher, S. W. A Constrained Regularization Method for Inverting Data Represented by Linear Algebraic or Integral Equations. *Comput. Phys. Commun.* **1982**, *27*, 213−227.
(27) Takasaki, M.; Kimura, K.; Kawaguchi, K.; Abe, A.; Katagiri, G. Structural Analysis of a Perfluorosulfonate Ionomer in Solution by ^{19}F and ^{13}C NMR. *Macromolecules* **2005**, *38*, 6031−6037.
(28) Vázquez, G.; Alvarez, E.; Navaza, J. M. Surface Tension of Alcohol + Water from 20 to 50 °C. *J. Chem. Eng. Data* **1995**, *40*, 611−614.
(29) Schlick, S.; Gebel, G.; Pineri, M.; Volino, F. ^{19}F NMR Spectroscopy of Acid Nafion Membranes and Solutions. *Macromolecules* **1991**, *24*, 3517−3521.
(30) Avalos, J.; Gebel, G.; Pineri, M.; Volino, F.; Schlick, S. Comparative Study of Perfluorinated Ionomers with Short and Long Pendant Chains by ^{19}F NMR. *Polym. Prepr. (Am. Chem. Soc., Div. Polym. Chem.)* **1993**, *34*, 448−449.
(31) Lousenberg, R. D. Molar Mass Distributions and Viscosity Behavior of Perfluorinated Sulfonic Acid Polyelectrolyte Aqueous Dispersions. *J. Polym. Sci., Part B: Polym. Phys.* **2005**, *43*, 421−428.
(32) Mourey, T. H.; Slater, L. A.; Galipo, R. C.; Koestner, R. J. Size-exclusion Chromatography of Perfluorosulfonated Ionomers. *J. Chromatogr. A* **2011**, *1218*, 5801−5809.
(33) Potemkin, I. I.; Khokhlov, A. R. Nematic Ordering in Dilute Solutions of Rodlike Polyelectrolytes. *J. Chem. Phys.* **2004**, *120*, 10848−10851.
(34) Yang, D.; Venev, S. V.; Palyulin, V. V.; Potemkin, I. I. Nematic Ordering of Rigid Rod Polyelectrolytes Induced by Electrostatic Interactions: Effect of Discrete Charge Distribution along the Chain. *J. Chem. Phys.* **2011**, *134*, 074901 (16 pages).
(35) Ise, N.; Okubo, T. "Ordered" Distribution of Electrically Charged Solutes in Dilute Solutions. *Acc. Chem. Res.* **1980**, *13*, 303−309.
(36) Matsuoka, H.; Schwahn, D.; Ise, N. Determination of Cluster Size in Polyelectrolyte Solutions by Small-Angle Neutron Scattering. In *Macro-ion Characterization*; Schmitz, K., Ed.; American Chemical Society: Washington, DC,1993; ACS Symposium Series *548*, Chapter 27.
(37) Sedlák, M. Extraordinary Behavior of Salt-Free Solutions of Strongly Charged Polyelectrolytes. In *Macro-ion Characterization*; Schmitz, K., Ed.; American Chemical Society: Washington, DC, 1993, ACS Symposium Series *548*, Chapter 26.
(38) Matsuoka, H.; Ogura, Y.; Yamaoka, H. Effect of Counterion Species on the Dynamics of Polystyrenesulfonate Aqueous Solution as Studied by Dynamic Light Scattering. *J. Chem. Phys.* **1998**, *109*, 6125−6132.
(39) Hammouda, B.; Horkay, F.; Becker, M. L. Clustering and Solvation in Poly(acrylic acid) Polyelectrolyte Solution. *Macromolecules* **2005**, *38*, 2019−2021.

Reprinted from the Journal of Physical Chemistry B, Vol. 118, pp. 14922-14928 (http://dx.doi.org/10.1021/jp506814m),

2014 年豊田ビームライン研究発表一覧

原著論文

[1] Hiroshi Oji, Yi-Tao Cui, Tomoyuki Koganezawa, Noritake Isomura, Kazuhiko Dohmae, and Jin-Young Son, "A HAXPES Measurement System up to 15 keV Developed at BL46XU of SPring-8", Journal of Physics: Conference Series, **502**, (2014) 012006.

[2] Yujiro Hayashi, Yoshiharu Hirose, and Daigo Setoyama, "*In Situ* Three-dimensional Orientation Mapping in Plastically-deformed Polycrystalline Iron by Three-dimensional X-ray Diffraction", Materials Science Forum, **777**, (2014) 118-123.

[3] Wakayama Hiroaki, Hirotaka Yonekura, and Masashi Harada, "Effects of Metal Loading and Magnetic Field Strength on Alignment of Noncrystalline Block Copolymers Doped with Metal Complexes", Journal of Polymer Research, **21**, (2014) 488.

[4] Daigo Setoyama, Yujiro Hayashi, and Noritoshi Iwata, "Crystal Plasticity Finite Element Analysis Based on Crystal Orientation Mapping with Three-Dimensional X-ray Diffraction Microscopy", Materials Science Forum, **777**, (2014) 142-147.

[5] Yoshinari Makimura, Chikaaki Okuda, and Takamasa Nonaka, "X-Ray Absorption and Diffraction Studies of LiNiO2-Derivatives with or without Electrolyte at Elevated Temperature", ECS Electrochemistry Letters, **3**, (2014) A66-A68.

[6] Keita Sekizawa, Takamasa Nonaka, Takao Arai, and Takeshi Morikawa, "Structural Improvement of CaFe2O4 by Metal Doping toward Enhanced Cathodic Photocurrent", ACS Applied Materials & Interfaces, **6**, (2014) 10969-10973.

[7] Makoto Yamaguchi, Takuro Matsunaga, Kazuki Amemiya, Akihiro Ohira, Naoki Hasegawa, Kazuhiko Shinohara, Masaki Ando, and Toshihiko Yoshida, “Dispersion of Rod-like Particles of Nafion in Salt-Free Water/1-Propanol and Water/Ethanol Solutions”, Journal of Physical Chemistry B, **118**, (2014) 14922-14928.

査読無しプロシーディングス、公開技術報告書、総説、口頭／ポスター発表等

[1] 小屋町潤、八木和行、梶田晴司、泉貴士、遠山護、斉藤浩二、杉村丈一、 "In-situ XRD Analysis of Frictional Area during Scuffing of Steel by Synchrotron 1 -Phase Transformation at Onset of Plastic Flow-", トライボロジー会議 2014 春東京　予稿集, , (2014)

[2] 梶田晴司、泉貴士、八木 和行、小屋町潤、遠山護、斉藤 浩二、杉村 丈一、"In-situ XRD Analysis of Frictional Area during Scuffing of Steel by Synchrotron 2 -Temperature Analysis of Frictional Area Phase Transformation-", トライボロジー会議 2014 春東京　予稿集, , (2014)

[3] 小屋町潤、八木和行、梶田晴司、泉貴士、三田修三、斉藤浩二、杉村丈一、"In-situ XRD Analysis of Frictional Area during Scutting of Steel by Synchrotron 3 -Surface Analysis after Scuffing-"、トライボロジー会議 2014 秋盛岡　予稿集, , (2014).

[4] 八木 和行、梶田晴司、泉貴士、遠山 護、小屋町潤、斉藤 浩二、杉村 丈一、 "In-situ Analysis

of Phase Transformation during Scuffing by Synchrotron XRD", 第 62 回 レオロジー討論会 予稿集, , (2014).

[5] 木村英彦、瀬戸山大吾、山口聡、広瀬美治、奥田勝治、梅村祐二、福田邦雄、"Development of Slit System for Area Detector and Synchrotron Diffraction Measurement"、日本材料学会 第 48 回 X 線材料強度に関するシンポジウム講演論文集 (Proceedings of the 48th Symposium on X-ray Studies on Mechanical Behavior of Materials), (2014) 3-6.

[6] 鈴木賢一郎、長井康貴、"Mesoporous Ferrihydrite by a Solution-Phase Cooperative Assembly Process for Air Purification"、セラミックス (Ceramics Japan), 49, (2014) 473-477.

[7] 林雄二郎、広瀬美治、瀬戸山大吾、"Development of Three-dimensional X-ray Diffraction Microscopy at the Toyota Beamline"、豊田ビームライン研究発表会プロシーディング, 4, (2014) 3-7.

[8] 松永拓郎、原田雅史、山口聡、青木良文、福森健三, "Relationship between Physical Properties and Hierarchical Structure for Semi-crystalline Polymers"、豊田ビームライン研究発表会プロシーディング, 4, (2014) 8-11.

[9] 畑中達也、廣嶋一崇、野中敬正、西村友作、堂前和彦、"High-accuracy XAFS Measurements of Transient Behavior in Fuel Cell Electrocatalys"、豊田ビームライン研究発表会プロシーディング, 4, (2014) 12-15.

[10] 青木良文、光岡拓哉、堂前和彦、福森健三、”Study on Thermal-Aging of EPDM Rubber by Time Resolved XAFS”、 豊田ビームライン研究発表会プロシーディング, 4, (2014) 16-19.

[11] 光岡拓哉、野中敬正、鈴木教友、大坪功、斎藤史朗、”Time Resolved XAFS Study of Metal Adsorption Mechanism of Iron Reduced by Bacteria”、 豊田ビームライン研究発表会プロシーディング, 4, (2014) 20-22.

[12] 磯村典武、野中敬正、堂前和彦、雀芸涛、陰地宏、孫珍永、”Study of a Depth Profiling Method by HAXPES with Energies up to 15 keV”、 豊田ビームライン研究発表会プロシーディング, 4, (2014) 23-27.

[13] 大田慎吾、野中敬正、"Distribution Analysis of Electrochemical Reaction in Cathode Layer for All-Solid-State Lithium Ion Battery"、豊田ビームライン研究発表会プロシーディング, 4, (2014) 28-32.

[14] 林雄二郎、広瀬美治、妹尾与志木、”Intragranular Orientation Observation by Scanning Three-Dimensional X-ray Diffraction Microscopy”、日本金属学会 春期大会 [2014.03.21-03.23] Tokyo, Japan.

[15] 林雄二郎、” 走査型 3DXRD 顕微鏡法による多結晶すべり変形の観察”、第9回 SPring-8 金属材料評価研究会 [2014.02.14] Tokyo, Japan.

[16] 林雄二郎、” 走査型 3DXRD 顕微鏡法の開発”、日本学術振興会 加工プロセスによる材料新機能発現 第 176 委員会 第 25 回研究会 [2014.01.30] Tokyo, Japan

[17] 林雄二郎、” 走査型 3DXRD 顕微鏡法による実用金属材料の観察”、日本放射光学会年会・放射光科学合同シンポジウム [2014.01.11-01.13] Hiroshima, Japan.

[18] 松永拓郎、片桐 好秀、森下卓也、原田雅史、福森健三, "Observation on Injection Molding Process of Polymers", 第 11 回 SPring-8 産業利用報告会 第 5 回 豊田ビームライン研究発表会

[2014.09.05]

[19] 松永拓郎、片桐 好秀、森下卓也、原田雅史、福森健三、"In-Situ Observation on Injection Molding Process by Small-angle X-ray Scattering", 日本分析化学会 高分子分析研究懇談会 第19回 高分子分析討論会 [2014.10.16-10.17] Nagoya, Japan.

[20] 松永拓郎、片桐 好秀、森下卓也、原田雅史、福森健三、"Observation system of X-ray Scattering from Molds for Injection Molding Process", 高分子学会 年次大会 [2014.05.28-05.30] Nagoya, Japan.

[21] 松永拓郎、片桐 好秀、森下卓也、原田雅史、福森健三、"In-Situ Observation on Crystallization Process of Poly (phenylene sulfide) during Injection Molding"、高分子討論会 [2014.09.24-09.26] Nagasaki, Japan.

[22] Hiroaki Wakayama, "Periodically Ordered Nanohetero Inorganic Structures of Nanoparticles, Nanorods and Layers in a Matrix from Self-Assembled Block Copolymers", 2014 MRS Spring Meeting & Exhibit [2014.04.21-04.25] San Francisco, USA.

[23] Hiroaki Wakayama, "Periodic Order of Metal-containing Block Copolymer Induced under Magnetic Field", 高分子討論会 [2014.09.24-09.26] Nagasaki, Japan.

[24] 泉貴士、梶田晴司、遠山護、八木 和行、小屋町潤、杉村丈一、斉藤浩二、"摩擦面その場X線回折による鋼材の焼付き現象解析", 第11回 SPring-8 産業利用報告会 [2014.09.04] Himeji, Japan

[25] Kazuyuki Yagi, Takashi Izumi, Jun Koyamachi, Mamoru Tohyama, Koji Saito, Joichi Sugimura, "In-situ Observation of Synchrotron X-ray Diffraction and Temperature During Scuffing of Steel", Tribology Frontiers Conference [2014.10.26-10.28] Chicago, USA

[26] 野中敬正、太田慎吾、駒形将吾、西村友作、酒井真利、"酸化物全固体電池の深さ分解 XAFS 解析"、日本放射光学会年会・放射光科学合同シンポジウム [2014.01.11-01.13] Hiroshima, Japan.

[27] 野中敬正、"自動車関連材料の in-situ XAFS 解析"、PF 研究会 次世代放射光光源で期待されるXAFS を活用したサイエンス [2014.07.11-07.12] Tsukuba, Japan

[28] 野中敬正、佐々木厳、奥田匠昭、西村友作、川浦宏之、牧村嘉也、"Li イオン電池過充電挙動の in situ XAFS・XRD 解析"、第11回 SPring-8 産業利用報告会 [2014.09.04-09.05] Himeji, Japan.

[29] 岡秀亮、牧村嘉也、西村友作、野中敬正、奥田匠昭、近藤 広規、佐々木厳、"Operando Measurements of Positive and Negative Electrodes Using Synchrotron X-ray"、第55回 電池討論会 [2014.11.19-11.21] Kyoto, Japan.

[30] 野中敬正、関澤佳太、森川健志、"可視光応答P型半導体材料のXAFS解析"、第11回 SPring-8 産業利用報告会 [2014.09.04-09.05] Himeji, Japan.

[31] Tsuyoshi Sasaki, Chikaaki Okuda, Takamasa Nonaka, Yusaku Nishimura, Yoshinari Makimura, Yasuhito Kondo, "Exploring Overcharge Behavior of Li-ion Batteries by Synchrotron X-ray Diffraction and Absorption Fine Structure", 226th Meeting of the Electrochemical Society, [2014.10.05-10.09] Cancun, Mexico.

[32] 奥田匠昭、牧村嘉也、野中敬正、西村友作、佐々木厳、近藤康仁、竹内要二、"Li 二次電池用層状 Ni 系正極の昇温過程における XAFS 解析-電解液の影響-"、電気化学会 第81回大会 [2014.03.29-03.31] Suita, Japan.

[33] 佐々木厳、奥田匠昭、野中敬正、西村友作、牧村嘉也、近藤康仁、小林哲郎、竹内要二、"放射光 XAFS-XRD 同時測定による Li 二次電池の過充電挙動解析"、電気化学会 第 81 回大会 [2014.03.29-03.31] Osaka, Japan.

[34] 関澤佳太、野中敬正、荒井健男、森川健志、"金属添加による CaFe2O4 光電極の高効率化"、日本化学会 春季年会 [2014.03.27-03.30] Nagoya, Japan.

[35] 向山真登、古田典利、山重寿夫、野中敬正、"In situ X 線イメージング法によるリチウムイオン電池の断面方向電解液濃度分布解析"、第 55 回 電池討論会 [2014.11.19-11.21] Kyoto, Japan.

[36] Hisao Yamashige, Noritoshi Furuta, Masato Mukouyama, Keiji Kawamura, Hisayoshi Ota, Takamasa Nonaka, Hiroyuki Kawaura, "In-situ X-ray Imaging Study on the Cross-sectional Distribution of Li-ion Concentration", 226th Meeting of The Electrochemical Society [2014.10.05-10.09] Cancun, Mexico.

[37] 長井康貴、平林武史、堂前和彦、田辺稔貴、高木信行、"放射光解析技術の自動車三元触媒開発への応用”、触媒討論会 [2014.09.25-09.27] Higashi-hiroshima, Japan

[38] 酒井真利、長井康貴、高橋直樹、"Cu/CeO2 触媒による NO 還元反応—Cu/CeO2 界面構造とその反応特性—"、触媒討論会 [2014.09.25-09.27] Higashi-hiroshima, Japan.

[39] 瀬戸山大吾、林雄二郎、広瀬美治、"Scanning 3DXRD observation and crystal plasticity finite element analysis of deformation behavior in polycrystalline iron "、日本機械学会 M&M2014 材料力学カンファレンス [2014.07.18-21] Fukushima, Japan.